UC Berkeley
UC Berkeley Electronic Theses and Dissertations

Title
Modeling and Analysis of Elements in Structural Mechanics

Permalink
https://escholarship.org/uc/item/70m2w7z8

Author
Drazin, Paul Luke

Publication Date
2017

Peer reviewed|Thesis/dissertation

Modeling and Analysis of Elements in Structural Mechanics

by

Paul Luke Drazin

A dissertation submitted in partial satisfaction of the

requirements for the degree of

Doctor of Philosophy

in

Engineering - Mechanical Engineering

in the

Graduate Division

of the

University of California, Berkeley

Committee in charge:

Professor Sanjay Govindjee, Co-chair
Professor Oliver O'Reilly, Co-chair
Professor Panayiotis Papadopoulos
Professor Khalid Mosalam

Spring 2017

Modeling and Analysis of Elements in Structural Mechanics

Abstract

Modeling and Analysis of Elements in Structural Mechanics

by

Paul Luke Drazin

Doctor of Philosophy in Engineering - Mechanical Engineering

University of California, Berkeley

Professor Sanjay Govindjee, Co-chair

Professor Oliver O'Reilly, Co-chair

The focus of this work is to advance the theoretical and modeling techniques for the fields of hybrid simulation and multi-slider friction pendulum systems (MSFPs). Hybrid Simulation is a simulation technique involving the integration of a physical system and a computational system with the use of actuators and sensors. This method has a strong foundation in the experimental mechanics community where it has been used for many years. The hybrid simulation experiments are performed with the assumption of an accurate result as long as the main causes of error are reduced. However, the theoretical background on hybrid testing needs to be developed in order validate these findings using this technique. To achieve this objective, a model for hybrid simulation is developed and applied to three test cases: an Euler-Bernoulli beam, a nonlinear damped, driven pendulum, and a boom crane structure. Due to the complex dynamics that these three test cases exhibit, L^2 norms, Lyapunov exponents, and Lyapunov dimensions, as well as correlation exponents were utilized to analyze the error in hybrid simulation tests. From these three test cases it was found that hybrid simulations are highly dependent on the natural frequencies of the dynamical system as well as how and where the hybrid split is located. Thus, proper care must be taken when conducting a hybrid experiment in order to guarantee reliable results.

Multi-stage friction pendulum systems (MSFPs), such as the triple friction pendulum (TFP), are currently being developed as seismic isolators. However, all current analytical models are inadequate in modeling many facets of these devices. Either the model can only handle uni-directional ground motions while incorporating the kinetics of the TFP system, or the model ignores the kinetics and can handle bi-directional motion. And in all cases, the model is linearized to simplify the equations. The second part of this dissertation presents an all-in-one model that incorporates the full nonlinear kinetics of the TFP system, while allowing for bi-directional ground motion. In this way, the model presented here is the most complete single model currently available. It was found that the non-linear model can more accurately predict the experimental results for large displacements due to the nonlinear kinematics used to describe the system. The model is also able to successfully predict the experimental results for bi-directional ground motions.

1

Contents

List of Figures

List of Tables

Acknowledgments

First and foremost, I would like to thank my advisor Professor Sanjay Govindjee for all of the help, advice, insight, and support that he has given me during my time as Ph.D. student these last 5 years. I would not have been able to complete all of the research in this dissertation without him. I have truly enjoyed the many interactions with him over the years; from stressful meetings trying to figure out research problems, being a GSI and reader for countless classes, helping grade finals, and running into him at the gym. I am truly thankful for the opportunity to work with him, and all of the knowledge and experience that I have gained from being his student.

I would like to thank my co-advisor Professor Oliver O'Reilly, who, I can honestly say, is the main reason that I decided to study the dynamics at UC Berkeley. I still remember taking my first class with him as an undergraduate, and his dedication and enthusiasm for dynamics made me realize that is what I wanted to study. I am thankful for the opportunity that he gave me when he accepted me to the Ph.D. program in Mechanical Engineering.

I would also like to thank Professor Khalid Mosalam for the help when I was first starting out as a graduate student and as a coauthor on my first published paper [20].

And many thanks to Professor Panos Papadopoulos for agreeing to be on my dissertation committee and for the valuable feedback he gave on this dissertation.

I am grateful to Professors Fai Ma, James Casey, David Steigmann, and John Strain for all being members of my qualifying exam committee.

I also want to thank my many colleagues and friends including Christopher Daily-Diamond, Evan Hemingway, Giorgio De Vera, Ahmed Bakhaty, Miklos Zoller, Xuance Zhou, Alyssa Novelia, Sunny Mistry, Gerd Brandstetter, Giuseppe Montella, and Kristin de Payrebrune for all of the support, discussions, and amazing memories we had over the last 5 years. I also want to thank the countless other friends and classmates that I made at UC Berkeley who made my life interesting and made my many years at UC Berkeley some of the best years of my life.

And a special thanks to Marc Zajac, Robert Tang-Kong, Gio Gajudo, Erik Bertelli, and Allison Vuong for taking the time to help edit this dissertation.

I would like to recognize and thank Dr. Daniel Kawano for his work on the latex style files used to create this dissertation.

Finally, I want to thank my Mom, Dad, and Brother for all of the encouragement they gave me throughout, without which I would not have reached this point in my life.

Chapter 1

Introduction

The field of structural mechanics is very broad, with focuses on experimentation as well as theoretical and numerical modeling. Theoretical and numerical modeling allow for cheaper and quicker predictions than an experiment, and in some cases an experiment may be impractical due to size and cost constraints. However, theoretical and numerical models need to be validated against experimental tests to guarantee the utility and accuracy of the model. For these reasons, it is important that experimentation and modeling progress and work together. However, there are some instances where the theoretical and numerical modeling for a specific topic is lagging behind the experimental efforts. One such area is that of hybrid simulation. Another such topic is that of multi-slider friction pendulum (MSFP) systems. Thus, the aim of this dissertation is to expand on the theoretical and numerical modeling and analysis of those two areas of structural mechanics, and when possible, these theoretical and numerical models are compared against experimental results.

1.1   Background on Hybrid Simulation

Hybrid simulation (or hybrid-testing) is a popular experimental method that is primarily used in Civil Engineering laboratories [39, 44, 57, 60]. It originated roughly 30 years ago [59] and has been used continuously and extensively as a methodology to experimentally assess structural systems under earthquake loadings. Occasionally the methodology has also been used in other disciplines to assess dynamic phenomena; see e.g. [8, 65, 70]. The central problem that hybrid simulation addresses is that it is very difficult and expensive to test full-size civil structures for their structural capacities under seismic loads. The largest testing facility in world is the E-Defense facility [21] which can test structures with a 20 m × 15 m plan and 12 MN weight. While this represents a large capacity, it precludes the testing of many types of structures, is very expensive due to the need to build full-size prototypes, has limited throughput, and does not easily allow for design exploration.

At its heart, one can think of experimental testing of this variety as the use of an analog computer (algorithm) to simulate the behavior of a structure. Hybrid testing and its many

1

variants (see e.g. [40, 55]) tries to leverage this viewpoint in the following manner: (1) The determination of the dynamic response of a structural system is thought of as the integration of the equations of motion for the structure; (2) The integration of the system of equations is done by a hybrid mix of numerical and analog computing. In practice, this means that part of the structural system is physically present in the laboratory and the remainder is represented by a computer model. Both parts of the structure are subjected to dynamic excitation and they interact via a system of sensors and actuators in real- and/or pseudo-time [69]. Figure 1.1 provides a schematic of the setup. Its advantage comes about when one can place the bulk of the structure in the computer due to a confidence in its model; the physical part typically represents a subset of the structure for which one does not have a good model; see e.g. [43].
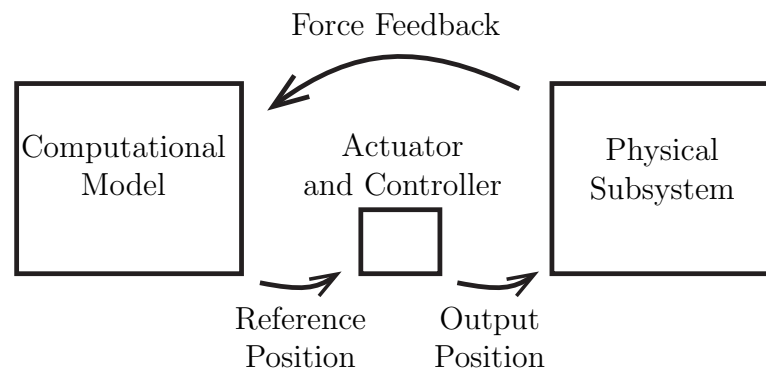
Fig. 1.1   A simple diagram of a hybrid system setup.

Most of the work on hybrid simulation has been devoted to the actual execution of experiments; as this is a large task in and of itself, little theoretical work has been performed to verify the results that these experiments produce. The main errors associated with hybrid simulation include time integration errors, control errors, interface splitting errors, and random signal errors, which can further be classified as either systematic or random errors [56, 66]. The bulk of the literature on hybrid-testing has focused on improving the accuracy and speed of the numerical computation and the fidelity of the control system [9, 12, 67] – all with the implicit assumption that improvements in these aspects will render a result that is more faithful to an untested physical reality. There has also been attempts to see how the location of the hybrid interface can affect the overall dynamics of the hybrid system [19, 61]. However, there has been a lack of studies on the errors directly associated with the mismatch inherently created at the hybrid interface by the use of sensors and actuators.

Recently, efforts have been put forth to try and understand the theoretical limitations of hybrid testing [4, 18, 19, 20] independent of the systematic and random errors that arise from numerical issues and sensor errors. These works utilized a reference structural system that was fully theoretical, split the system into fictitious physical and computational parts, and then explored the fidelity of the hybrid equations with respect to the reference

equations. In this way, the true dynamical response of the reference system was known *a priori* in analytic form and could be compared to the hybrid-system response which was also known in analytic form. The overall methodology thus illuminated directly the central feature of all hybrid simulation methodologies – viz., the presence of a split system that is patched together with an imperfect interface.

1.2 Background on Multi-Slider Friction Pendulums

Multi-stage friction pendulum systems (MSFPs) are currently being designed and developed as seismic isolation devices for a wide range of structural and non-structural systems [41, 68, 72]. One of the earliest forms of the MSFP was the single friction pendulum, developed as early as 1987 [71]. This original design has been expanded to double and triple friction pendulums to increase the utility of the device as a seismic isolator [23, 26]. These seismic isolators consist of steel bearings with spherical concave surfaces that slide along one another. An example of the triple friction pendulum (TFP) can be seen in Fig. 1.2. As the bearings slide along one another, they are able to provide restoring forces related to the relative displacement between bearings, which creates a variable stiffness associated with the overall motion of the friction pendulum [23]. Also, the friction between sliding bearings gives the friction pendulums a hysteretic behavior [26].

| (a) | (b) |
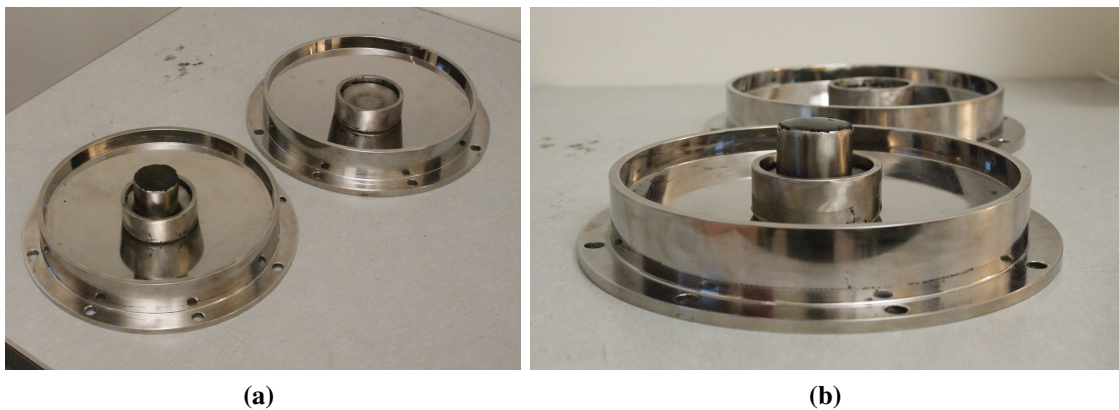
Fig. 1.2   (a) An overview image of an example of a Triple Friction Pendulum (TFP). (b) A close up front view of a TFP.

Multiple areas of the world, including California and Japan, are at a constant risk of a major earthquake, and the proper usage of seismic isolators, such as MSFPs, can drastically reduce the damage sustained to buildings, bridges, etc. due to a major earthquake [11, 42]. For this reason, well-functioning models of MSFPs are necessary to make sure that structures are properly isolated in the event of an earthquake. As the usage of MSFPs became more common, there were extensive experimental tests on MSFPs to help characterize their motion due to different types of excitation [25, 45]. However, experimental tests can be expensive and time consuming, thus numerical models were developed to help

with the simulation of these MSFPs [5, 6, 24, 63]. While current models have come a long way, no current model for MSFPs utilizes a rigorous setup for the kinematics of the internal sliders; they start directly with scalar equations. Another drawback of current models, is that no one model incorporates the full kinetics of the MSFPs with bi-directional motion; there is either full kinetics for planar motion or bi-directional motion with only kinematics and no kinetics.

1.3   Organization of this Dissertation

Chapters 2-4 focus on the development of theoretical models for hybrid simulation with analyses of those models. Chapter 2 focuses solely on the beam, for both the elastic and viscoelastic systems. Chapter 2 also includes the derivation of the equations of motion for the reference and hybrid systems. Chapter 3 follows the same pattern as Chapter 2, but for a nonlinear damped and driven pendulum. Chapter 4 applies the theoretical model for hybrid simulation to that of a crane structure. Chapter 5 then develops a model for multi-slider friction pendulums (MSFP) and uses that model on the specific case of the triple friction pendulum (TFP) and compares it to previous models and experimental data. Finally, Chapter 6 provides a comprehensive summary of the results from the previous chapters, along with comments on possible of future work.

Chapter 2

Hybrid Simulation Theory Applied to Continuous Beams

2.1 Introduction

The first aspect of this dissertation focuses solely on the *theoretical* performance of real-time hybrid simulation as an experimental method, ignoring all of the numerical and random errors, as this leads to a best case scenario for a hybrid experiment. This approach eliminates the errors associated with time integration methods and signal noise and focuses only on the errors that are generated by systematic interface mismatch errors – an element that is always present in hybrid simulations. In this way one is able to focus in on the essential error associated with a system possessing a split interface and to understand the inherent error associated with imperfect interface splitting without the added clutter associated with time stepping error etc. The net result then provides a true estimate of the best possible error targets for a hybrid system.

To make the analysis concrete, this dissertation focuses on a harmonically driven beam. This system has been chosen for its relative simplicity and the ability to analyze the solution in an analytical form. Both the elastic as well as the viscoelastic cases will be examined. Further, this work always considers the case of distributed mass which occurs in the real physical objects. By studying the problem from a strictly theoretical viewpoint, one can fully control the situation and precisely define what one means by *truth*. This allows one to precisely identify a lower bound below which one can not improve a hybrid simulation via, say, improvements in time integration methods or improvements in the control scheme. While the setup is rather simple, the results are felt to have general applicability. In what follows, the general theoretical setting of hybrid simulation is first described; then the elastic beam is considered within this setting, followed by the viscoelastic beam. This is followed by a study of the behavior of hybrid simulation for these two systems and finally a set of concluding observations and comments are presented.

2.2 General Theory of Hybrid Simulation

In this section a general framework for hybrid simulation is developed.

The Reference System

First, the reference system needs to be setup to which the hybrid system will be compared. Let the open set $\mathcal{D}$ be the domain of mechanical, as shown in Fig. 2.1a.

(a)	**(b)**
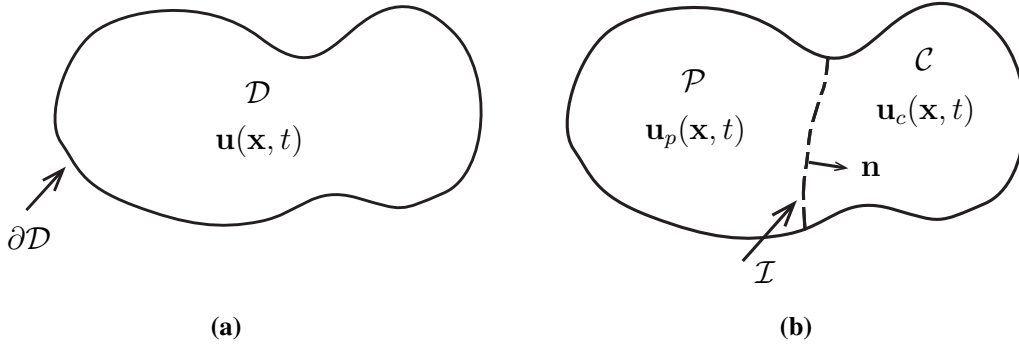
Fig. 2.1 (a) A general system with domain $\mathcal{D}$ and state vector $\mathbf{u}(\mathbf{x},t)$. (b) A general system with imposed separation into two substructures for comparison to the hybrid system.

The mechanical response of the system is characterized by a state vector,

$$\mathbf{u}(\mathbf{x},t) \text{ for } \mathbf{x} \in \mathcal{D}, \tag{2.1}$$

where t represents time. In order to compare the reference system response to the hybrid system response, imagine that the reference system is split into two substructures by an open set $\mathcal{I}$, with normal $\mathbf{n}$, which acts an interface between two substructures. Note, the interface $\mathcal{I}$ must be chosen such that for all $\mathbf{x} \in \mathcal{D}$, either $\mathbf{x} \in \mathcal{C}$ or $\mathbf{x} \in \mathcal{P}$ must hold, but not both. The two substructures are defined by the open sets $\mathcal{P}$ and $\mathcal{C}$, with the following definitions:

$$\mathcal{P} = \{\mathbf{x} \in \mathcal{D} \mid \mathbf{x} \cdot \mathbf{n} < 0\}, \tag{2.2}$$

$$\mathcal{C} = \{\mathbf{x} \in \mathcal{D} \mid \mathbf{x} \cdot \mathbf{n} > 0\}. \tag{2.3}$$

The "physical" substructure ($\mathcal{P}$-side) and the "computational" substructure ($\mathcal{C}$-side) are shown in Fig. 2.1b. The state vector can now be separated into two parts:

$$\mathbf{u}(\mathbf{x},t) = \begin{cases} \mathbf{u}_p(\mathbf{x},t) & \text{if } \mathbf{x} \in \mathcal{P} \\ \mathbf{u}_c(\mathbf{x},t) & \text{if } \mathbf{x} \in \mathcal{C}. \end{cases} \tag{2.4}$$

This defines the true response for a given mechanical system. The precise expression for $\mathbf{u}(\mathbf{x},t)$ is found by determining the function that satisfies the governing equations of motion on $\mathcal{D}$ and the imposed boundary conditions on $\partial\mathcal{D}$.

The Hybrid System

The response of the hybrid system should be defined in a similar fashion to make the comparison between the two systems straightforward. Using the same boundary defined in Fig. 2.1b, the hybrid system is separated into two substructures, as seen in Fig. 2.2. In order to differentiate the reference system from the hybrid system a superposed hat (ˆ) is used to indicate a quantity in the hybrid system. The mechanical response of the hybrid system is represented by the following state vector:

$$\hat{\mathbf{u}}(\mathbf{x},t) = \begin{cases} \hat{\mathbf{u}}_p(\mathbf{x},t) & \text{if } \mathbf{x} \in \mathcal{P} \\ \hat{\mathbf{u}}_c(\mathbf{x},t) & \text{if } \mathbf{x} \in \mathcal{C}. \end{cases} \tag{2.5}$$

In a hybrid system $\hat{\mathbf{u}}_p$ and $\hat{\mathbf{u}}_c$ are determined from the "solution" of the governing equations of motion for $\mathcal{P}$ and $\mathcal{C}$ subjected to the boundary conditions on $\partial\mathcal{P}$ and $\partial\mathcal{C}$. The boundary conditions on $\partial\mathcal{D} \cap \partial\mathcal{P}$ and $\partial\mathcal{D} \cap \partial\mathcal{C}$ naturally match those of the reference system. However, in the hybrid system one must additionally deal with boundary conditions on the two interface sides of $\mathcal{I}_p$ and $\mathcal{I}_c$, where $\mathcal{I}_p = \mathcal{I} \cap \partial\mathcal{P}$ and $\mathcal{I}_c = \mathcal{I} \cap \partial\mathcal{C}$. The boundary conditions on $\mathcal{I}_p$ and $\mathcal{I}_c$ are provided by the sensor and actuator system.
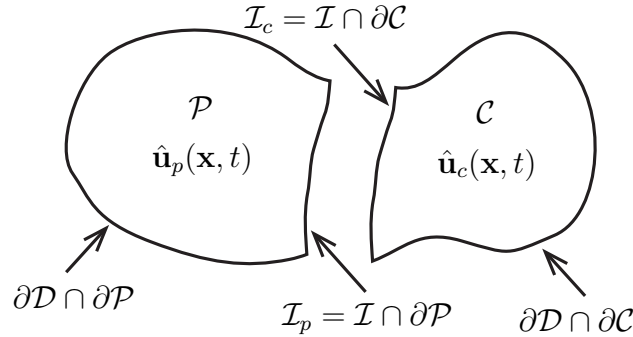
Fig. 2.2 The hybrid system separated into the physical, $\mathcal{P}$, and computational, $\mathcal{C}$, substructures.

The hybrid split leads to more unknowns than equations. To resolve this issue, a model of the actuator and sensor system is needed. A relatively general form for such a model can be expressed as [18]:

$$\underline{D}_c[\hat{\mathbf{u}}_c]\Big|_{\mathcal{I}_c} = \underline{D}_p[\hat{\mathbf{u}}_p]\Big|_{\mathcal{I}_p}, \tag{2.6}$$

where $\underline{D}_c[\bullet]$ and $\underline{D}_p[\bullet]$ are operators that generate the necessary equations at the interface from the state vectors $\hat{\mathbf{u}}_\bullet$. The specific form of $\underline{D}_c[\bullet]$ and $\underline{D}_p[\bullet]$ will be defined later in this dissertation. This model allows one to study the effects of systematic hybrid system splitting errors, specifically boundary mismatch errors. Such errors directly correlate to errors seen in experimental hybrid systems [1, 56].

In an actual hybrid simulation, one only has the physical part $\mathcal{P}$, the sensor and actuator system, and the computational model for part $\mathcal{C}$. This makes it challenging to know if

the determined response $\hat{\mathbf{u}}$ is correct to a sufficient degree. To circumvent this issue an analytical model for part $\mathcal{P}$ and part $\mathcal{C}$ will be used, and similarly for the sensor and actuator system. This will allow one to faithfully compute the error in the response quantity $\hat{\mathbf{u}}$ of the hybrid system by comparing it to the response quantity $\mathbf{u}$ of the reference system. The error investigated is then strictly the error in the hybrid system associated with the splitting interface.

Note, the previous definitions start from a reference system, and then develop a hybrid system framework. One can easily start from a hybrid system and develop the corresponding reference system. For example, let $\mathcal{C}$ and $\mathcal{P}$ be open sets that define the two substructures of a hybrid system. Then, the interface is defined as $\mathcal{I} = \partial\mathcal{C} \cup \partial\mathcal{P}$. From there, a domain is defined as $\tilde{\mathcal{D}} = \mathcal{C} \cup \mathcal{I} \cup \mathcal{P}$. Finally, the open set which defines the domain of the reference system is defined as $\mathcal{D} = \tilde{\mathcal{D}} \setminus (\mathcal{I} \cap \partial\tilde{\mathcal{D}})$.

L^2 Space and Hybrid Simulation Error

With the above notation in hand, consider now how one can understand hybrid simulation from a *geometric* point of view. First note that the space of L^2 functions over $\mathcal{B}$ is defined as [36]:

$$L^2(\mathcal{B}) = \{\mathbf{v} : \mathbf{v} \text{ is defined on } \mathcal{B} \text{ and } \int_{\mathcal{B}} \mathbf{v}^2 d\mathbf{x} < \infty\}, \tag{2.7}$$

where $\mathcal{B}$ is a bounded domain in $\mathbb{R}^3$. Using this definition one has

$$\mathbf{u} \in L^2(\mathcal{D}). \tag{2.8}$$

The restriction of $\mathbf{u}$ onto $\mathcal{C}$ is denoted as

$$\mathbf{u}_c \in L^2(\mathcal{C}), \tag{2.9}$$

and similarly for the restriction of $\mathbf{u}$ onto $\mathcal{P}$:

$$\mathbf{u}_p \in L^2(\mathcal{P}). \tag{2.10}$$

The same applies for the $\hat{\bullet}$ quantities. One notes that

$$L^2(\mathcal{D}) = L^2(\mathcal{C}) \times L^2(\mathcal{P}). \tag{2.11}$$

In $L^2(\mathcal{C})$, the displacements $\mathbf{u}_c$ and $\hat{\mathbf{u}}_c$ trace out trajectories with time. These two trajectories differ from each other since they are for two different systems. The same is true for the trajectories of $\mathbf{u}_p$ and $\hat{\mathbf{u}}_p$ in $L^2(\mathcal{P})$. By considering the trajectories in $L^2(\mathcal{C})$ and $L^2(\mathcal{P})$ as components of order pairs in $L^2(\mathcal{D})$ at each moment in time, one can combine trajectories from $L^2(\mathcal{C})$ and $L^2(\mathcal{P})$ into trajectories in $L^2(\mathcal{D})$, one for the reference system and one for hybrid system. A simple illustration of this situation is shown in Fig. 2.3. The difference between the two trajectories in $L^2(\mathcal{D})$ gives one the basis for an error analysis. Given a true
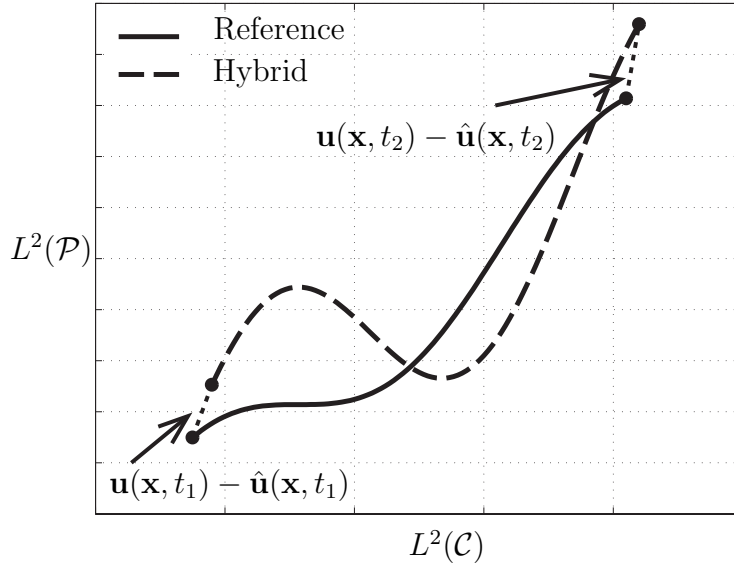
Fig. 2.3   A schematic illustration of a possible $L^2(\mathcal{D})$ space with trajectories for the reference and hybrid systems from time $t = t_1$ to $t = t_2$ showing the difference between the two trajectories.

solution $\mathbf{u}$ and a hybrid solution $\hat{\mathbf{u}}$, one can measure error using a space-time L^2-norm in the form of Eq. (2.12) [36]:

$$||e|| = \left(\int_0^T \int_{\mathcal{D}} \left| \mathbf{u}(\mathbf{x},t) - \hat{\mathbf{u}}(\mathbf{x},t) \right|^2 d\mathbf{x} dt \right)^{1/2}, \tag{2.12}$$

where T is the period of the harmonic excitation on the system and $\mathcal{D}$ is the complete domain of the system. This allows for a measurement of the absolute error between the reference system and the hybrid system over the domain of the mechanical system and over the period of the harmonic excitation.

2.3   Application to the Elastic Beam

The earlier set-up is now applied to a continuous beam, where one has access to exact analytical solutions for an intact reference system and for a hybrid (decomposed) system defined over $\mathcal{P}$ and $\mathcal{C}$.

Reference System

The reference system is an elastic, homogeneous beam pinned on both ends with a harmonic moment applied to one end. A diagram of the mechanical system is shown in Fig. 2.4.

9
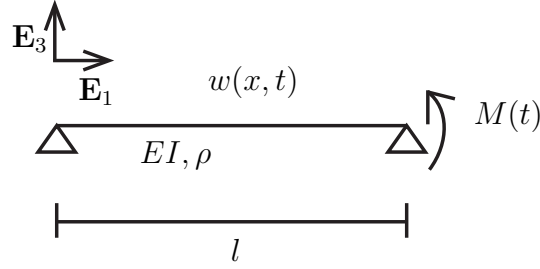
Fig. 2.4   The system of an elastic pinned-pinned beam with a terminally applied moment, $M(t)$.

In this case the displacement can be decomposed as shown in Eq. (2.13):

$$\mathbf{w} = w(x,t)\mathbf{E}_3, \tag{2.13}$$

where $\mathbf{E}_3$ represents the unit vector in the 3-direction as indicated in Fig. 2.4. In what follows, the vector form is ignored, and only $w(x,t)$ is considered. The partial differential equation that governs the motion of the mechanical system is given by the dynamic form of the classical Bernoulli-Euler equation:

$$\rho\ddot{w} = -EIw_{,xxxx}, \tag{2.14}$$

where ρ is the linear mass density, E is the elastic modulus, I is the second moment of area of the beam, and comma notation indicates differentiation. The terminally applied moment, M, is assumed to be harmonic:

$$M(t) = \bar{M}\exp(i\omega t), \tag{2.15}$$

where $\bar{M}$ is the magnitude of the applied moment and ω is the frequency of the applied moment. The well-known solution to this system is given by

$$w(x,t) = \left(\frac{-\bar{M}\sin(\beta x)}{2EI\beta^2\sin(\beta l)} + \frac{\bar{M}\sinh(\beta x)}{2EI\beta^2\sinh(\beta l)} \right)\exp(i\omega t), \tag{2.16}$$

where l is the beam span and the parameter β is determined from

$$\beta^4 = \frac{\rho}{EI}\omega^2. \tag{2.17}$$

Hybrid System

The pinned-pinned beam is now represented by a hybrid system using a specific separation. The hybrid system is shown in Fig. 2.5, where the $\mathcal{P}$-side is the left side, without the applied moment, and the $\mathcal{C}$-side is the right side, with the applied moment.
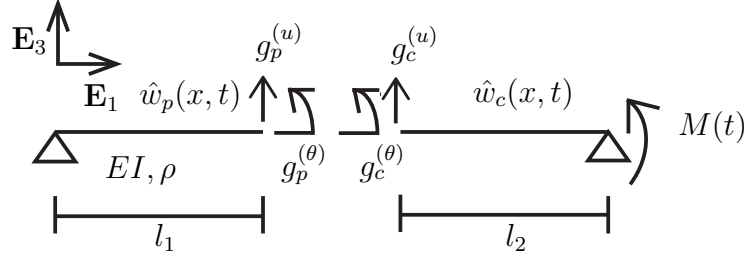
Fig. 2.5 The hybrid system of an elastic pinned-pinned beam with a terminally applied moment, $M(t)$, and boundary functions $g_p^{(u)}(t)$, $g_c^{(u)}(t)$, $g_p^{(\theta)}(t)$, and $g_c^{(\theta)}(t)$, $l_1 + l_2 = l$.

The separation of the hybrid system occurs at $x = l_1$, thus, in this system, the displacement is given by

$$\hat{w}(x,t) = \begin{cases} \hat{w}_p(x,t) & \text{if } 0 \le x < l_1 \\ \hat{w}_c(x,t) & \text{if } l_1 < x \le l. \end{cases} \tag{2.18}$$

Separation of variables is applied to the system, giving $\hat{w}_p(x,t) = \hat{X}_p(x)\hat{T}_p(t)$ and $\hat{w}_c(x,t) = \hat{X}_c(x)\hat{T}_c(t)$, where both must independently satisfy Eq. (2.14). This leads to the following equations:

$$\hat{X}_p(x) = \hat{b}_1 \cos(\hat{\beta}_p x) + \hat{b}_2 \sin(\hat{\beta}_p x) + \hat{b}_3 \cosh(\hat{\beta}_p x) + \hat{b}_4 \sinh(\hat{\beta}_p x), \tag{2.19a}$$

$$\hat{X}_c(x) = \hat{b}_5 \cos(\hat{\beta}_c x) + \hat{b}_6 \sin(\hat{\beta}_c x) + \hat{b}_7 \cosh(\hat{\beta}_c x) + \hat{b}_8 \sinh(\hat{\beta}_c x), \tag{2.19b}$$

$$\hat{T}_p(t) = \hat{T}_c(t) = \exp(i\omega t), \tag{2.19c}$$

where $\hat{b}_1 - \hat{b}_8$ are constants. Since $\hat{w}_p$ and $\hat{w}_c$ must both independently satisfy Eq. (2.14), the following relation also holds:

$$\hat{\beta}_p^4 = \hat{\beta}_c^4 = \frac{\rho}{EI}\omega^2. \tag{2.20}$$

Using Eq. (2.20) in conjunction with Eq. (2.17), it is noted that $\beta = \hat{\beta}_p = \hat{\beta}_c$. In order to determine $\hat{b}_1 - \hat{b}_4$, one needs four boundary conditions on $\mathcal{P}$. As is typical, one can take two from the left-side and two from the right-side of the domain of $\mathcal{P}$. The functions $g_p^{(\bullet)}$ will denote the boundary functions on $\mathcal{I}_p$, which in the present case is simply the point $x = l_1$. The same applies for $\hat{b}_5 - \hat{b}_8$ on $\mathcal{C}$ where the boundary functions on $\mathcal{I}_c$ will be denoted by $g_c^{(\bullet)}$. As an example, Fig. 2.5 shows boundary functions $g_p^{(u)}$ and $g_c^{(u)}$ for transverse displacements and $g_p^{(\theta)}$ and $g_c^{(\theta)}$ for rotations. Thus, the boundary conditions at

$x = l_1$ become

$$\hat{w}_p(l_1,t) = g_p^{(u)}(t) = \bar{g}_p^{(u)} \exp(i\omega t), \tag{2.21a}$$

$$\hat{w}_c(l_1,t) = g_c^{(u)}(t) = \bar{g}_c^{(u)} \exp(i\omega t), \tag{2.21b}$$

$$\hat{w}_{p,x}(l_1,t) = g_p^{(\theta)}(t) = \bar{g}_p^{(\theta)} \exp(i\omega t), \tag{2.21c}$$

$$\hat{w}_{c,x}(l_1,t) = g_c^{(\theta)}(t) = \bar{g}_c^{(\theta)} \exp(i\omega t). \tag{2.21d}$$

Note that $\bar{g}_p^{(\bullet)}$ and $\bar{g}_c^{(\bullet)}$ are so far unspecified. Intuitively they are related to each other but a discussion of this inter-relation is deferred to the discussion of a model for the interface errors.

Solving for $\hat{b}_1 - \hat{b}_8$, while employing the requisite boundary conditions at $x = 0$, $x = l$, $\mathcal{I}_p$, and $\mathcal{I}_c$, gives

$$\hat{w}_p(x,t) = \frac{\bar{g}_p^{(u)} D_2(\beta l_1, \beta x) - \frac{\bar{g}_p^{(\theta)}}{\beta} D_3(\beta l_1, \beta x)}{D_2(\beta l_1, \beta l_1)} \exp(i\omega t), \tag{2.22}$$

$$\hat{w}_c(x,t) = \left(\frac{\bar{M}}{2EI\beta^2} \left(A_1(\beta l_2)B_1\left(\beta(x-l_1)\right) - B_1(\beta l_2)A_1\left(\beta(x-l_1)\right) \right) \right.$$
$$\left. - \bar{g}_c^{(u)} D_2(\beta l_2, \beta(x-l)) + \frac{\bar{g}_c^{(\theta)}}{\beta} D_3(\beta(x-l), \beta l_2) \right) \frac{\exp(i\omega t)}{D_2(\beta l_2, \beta l_2)}, \tag{2.23}$$

where

$$A_1(x) = \sin(x) - \sinh(x), \tag{2.24a}$$

$$B_1(x) = \cosh(x) - \cos(x), \tag{2.24b}$$

$$D_2(x,y) = \cosh(x)\sin(y) - \cos(x)\sinh(y), \tag{2.24c}$$

$$D_3(x,y) = \sinh(x)\sin(y) - \sin(x)\sinh(y). \tag{2.24d}$$

Non-Dimensionalization and Determination of $\bar{g}_p^{(\bullet)}$ and $\bar{g}_c^{(\bullet)}$

To further the analysis, one needs to determine the so far unspecified boundary functions. In this regard, it is advantageous to non-dimensionalize the equations as well as to express the reference solution in the same format as the hybrid solution. For the latter point, an examination of Eqs. (2.16) and (2.24) shows that one can write the reference solution as

$$w(x,t) = \frac{\bar{M}D_3(\beta x, \beta l)}{2EI\beta^2 P_1(\beta l)} \exp(i\omega t), \tag{2.25}$$

where

$$P_1(x) = \sin(x)\sinh(x). \tag{2.26}$$

In order to non-dimensionalize Eqs. (2.22), (2.23), and (2.25), one can introduce the following non-dimensional quantities:

$$\eta = \frac{w}{l}, \quad \hat{\eta}_p = \frac{\hat{w}_p}{l}, \quad \hat{\eta}_c = \frac{\hat{w}_c}{l}, \quad y = \frac{x}{l}, \tag{2.27a}$$

$$\mu = \frac{\bar{M}l}{EI}, \tag{2.27b}$$

$$\omega_1 = \sqrt{\frac{EI}{\rho}}\frac{\pi^2}{l^2}, \quad \Omega = \frac{\omega}{\omega_1}, \quad \tau = \omega_1 t, \tag{2.27c}$$

$$\kappa = \beta l = \pi\sqrt{\Omega}, \tag{2.27d}$$

$$G_p^{(u)} = \frac{\bar{g}_p^{(u)}}{l}, \quad G_c^{(u)} = \frac{\bar{g}_c^{(u)}}{l}, \quad G_p^{(\theta)} = \bar{g}_p^{(\theta)}, \quad G_c^{(\theta)} = \bar{g}_c^{(\theta)}, \tag{2.27e}$$

$$L_1 = \frac{l_1}{l}, \quad L_2 = 1 - L_1, \tag{2.27f}$$

where ω_1 is the lowest resonant frequency of the pinned-pinned beam [62]. Thus Eqs. (2.22), (2.23), and (2.25) become

$$\eta(y,\tau) = \frac{\mu D_3(\kappa y, \kappa)}{2\kappa^2 P_1(\kappa)}\exp(i\Omega\tau), \tag{2.28}$$

$$\hat{\eta}_p(y,\tau) = \frac{G_p^{(u)}D_2(\kappa L_1, \kappa y) - \frac{G_p^{(\theta)}}{\kappa}D_3(\kappa L_1, \kappa y)}{D_2(\kappa L_1, \kappa L_1)}\exp(i\Omega\tau), \tag{2.29}$$

$$\hat{\eta}_c(y,\tau) = \left(\frac{\mu}{2\kappa^2}\Big(A_1(\kappa L_2)B_1(\kappa(y-L_1)) - B_1(\kappa L_2)A_1(\kappa(y-L_1))\Big)\right.$$
$$\left. - G_c^{(u)}D_2(\kappa L_2, \kappa(y-1)) + \frac{G_c^{(\theta)}}{\kappa}D_3(\kappa(y-1), \kappa L_2)\right)\frac{\exp(i\Omega\tau)}{D_2(\kappa L_2, \kappa L_2)}. \tag{2.30}$$

For the rest of this chapter, unless stated otherwise, all new variables or quantities are assumed to be dimensionless.

To complete the system of equations, $G_p^{(\bullet)}$ and $G_c^{(\bullet)}$ need to be determined. The conditions to determine $G_p^{(\bullet)}$ and $G_c^{(\bullet)}$ come from the characteristics of the sensor and actuator

control system. As a simple model, one can assume that the hybrid system produces a magnitude and phase error in the corresponding displacements, rotations, bending moments, and shear forces across the interface of the hybrid system. Using the notation introduced in Eq. (2.6), $\underline{D}_c[\bullet]$ is defined as

$$\underline{D}_c[\bullet] = \underline{D}[\bullet] = \begin{bmatrix} \bullet \\ \frac{\partial \bullet}{\partial y} \\ \frac{\partial^2 \bullet}{\partial y^2} \\ \frac{\partial^3 \bullet}{\partial y^3} \end{bmatrix}, \tag{2.31}$$

and $\underline{D}_p[\bullet]$ is defined as

$$\underline{D}_p[\bullet] = \underline{E}\,\underline{D}[\bullet], \tag{2.32}$$

with the same definition for $\underline{D}[\bullet]$ and $\underline{E}$ is expressed as

$$\underline{E} = \begin{bmatrix} (1+\varepsilon_u)\exp(i\Omega d_u) & 0 & 0 & 0 \\ 0 & (1+\varepsilon_\theta)\exp(i\Omega d_\theta) & 0 & 0 \\ 0 & 0 & (1+\varepsilon_M)\exp(i\Omega d_M) & 0 \\ 0 & 0 & 0 & (1+\varepsilon_V)\exp(i\Omega d_V) \end{bmatrix}. \tag{2.33}$$

Here $\varepsilon_{(\bullet)}$ are the magnitude of the tracking errors for the displacement, rotation, bending moment, and shear force at the interface and $d_{(\bullet)}$ are the tracking error time delays of the displacement, rotation, bending moment, and shear force. $\varepsilon_{(\bullet)}$ and $d_{(\bullet)}$ model the interface error in the hybrid system at $\mathcal{I}$. Using this model gives

$$\hat{\eta}_c(L_1,\tau) = \hat{\eta}_p(L_1,\tau)(1+\varepsilon_u)\exp(i\Omega d_u), \tag{2.34a}$$

$$\hat{\eta}_{c,y}(L_1,\tau) = \hat{\eta}_{p,y}(L_1,\tau)(1+\varepsilon_\theta)\exp(i\Omega d_\theta), \tag{2.34b}$$

$$\hat{\eta}_{c,yy}(L_1,\tau) = \hat{\eta}_{p,yy}(L_1,\tau)(1+\varepsilon_M)\exp(i\Omega d_M), \tag{2.34c}$$

$$\hat{\eta}_{c,yyy}(L_1,\tau) = \hat{\eta}_{p,yyy}(L_1,\tau)(1+\varepsilon_V)\exp(i\Omega d_V). \tag{2.34d}$$

The purpose of Eq. (2.34) is to relate $\hat{\eta}_c$ and $\hat{\eta}_p$ by their ratios, defined as $(1+\varepsilon_u)\exp(i\Omega d_u)$, similarly for their spatial derivatives. In this way, one can say that error is transferred from the physical side to the computational side if $(1+\varepsilon_{(\bullet)}) > 1$ and vice versa if $(1+\varepsilon_{(\bullet)}) < 1$. The same can be said of $d_{(\bullet)}$, depending on the sign of $d_{(\bullet)}$. Equations (2.34) together with Eqs. (2.29) and (2.30) can be used to analytically solve for $G_p^{(\bullet)}$ and $G_c^{(\bullet)}$ and thus complete the solution [17]. Note that this error model can be made more sophisticated but suffices to understand a number of features of hybrid systems.

2.4 Application to the Viscoelastic Beam

The same pinned-pinned beam model used previously is adopted for the viscoelastic case. For this purpose it is useful to introduce the complex elastic modulus:

$$E^* = E' + iE'', \tag{2.35}$$

where E' is the storage modulus, E'' is the loss modulus, and $i = \sqrt{-1}$ is the imaginary unit [27]. To be concrete, the standard 3-parameter Maxwell model for a linear viscoelastic solid will be employed (the so-called standard linear solid) [64]. In this case,

$$E' = E_\infty + \frac{\omega^2 t_r^2}{1 + \omega^2 t_r^2}(E_0 - E_\infty), \tag{2.36a}$$

$$E'' = \frac{\omega t_r}{1 + \omega^2 t_r^2}(E_0 - E_\infty), \tag{2.36b}$$

where E_0 is the instantaneous modulus and E_∞ is the equilibrium modulus. The relaxation time, t_r, is given by

$$t_r = \frac{1}{\bar{\omega}\zeta}. \tag{2.37}$$

The parameter ζ is the non-dimensional damping frequency, which determines the location of the damping peak in the frequency domain. Since E^* is complex, it can be expressed in polar form by

$$E^* = |E^*|\exp(i\delta), \tag{2.38a}$$

$$|E^*| = \sqrt{E'^2 + E''^2}, \tag{2.38b}$$

$$\delta = \tan^{-1}\left(\frac{E''}{E'}\right). \tag{2.38c}$$

Using this form of the complex elastic modulus, Eq. (2.17) becomes

$$\rho\omega^2 = |E^*|I\exp(i\delta)\beta^4. \tag{2.39}$$

Since ω, $|E^*|$, I, and ρ are real values, β must be complex. Solving for β results in

$$\beta = \sqrt[4]{\frac{\rho}{|E^*|I}}\sqrt{\omega}\exp\left(\frac{-i\delta}{4}\right). \tag{2.40}$$

The solution for the reference system now reads

$$w(x,t) = \left(\frac{-\bar{M}\exp(-i\delta)\sin(\beta x)}{2|E^*|I\beta^2\sin(\beta l)} + \frac{\bar{M}\exp(-i\delta)\sinh(\beta x)}{2|E^*|I\beta^2\sinh(\beta l)} \right)\exp(i\omega t). \tag{2.41}$$

The non-dimensionalization of Eq. (2.41) and the application of the functions defined by Eqs. (2.24) and (2.26) lead to the same relation given by Eq. (2.28), where all values have the same definitions as before except

$$\kappa = \beta l = \pi\sqrt{\Omega}\exp\left(\frac{-i\delta}{4}\right), \tag{2.42a}$$

and

$$\mu = \frac{\bar{M}l\exp(-i\delta)}{|E^*|I}. \tag{2.42b}$$

Likewise, Eqs. (2.29) and (2.30) hold for the viscoelastic pinned-pinned hybrid beam case, using the new definitions of κ and μ.

2.5 Analysis of the Hybrid Systems

Having analytic expressions for the response of the reference systems and the hybrid systems, it is possible to examine the intrinsic errors associated with hybrid simulation using the interface model. Error in hybrid simulation for a given loading and a given set of $\varepsilon_{(\bullet)}$ and $d_{(\bullet)}$ will be defined using the non-dimensionalized response functions as

$$e(y,\tau) = \eta(y,\tau) - \hat{\eta}(y,\tau). \tag{2.43}$$

For analysis purposes it is useful to examine the L^2-norm of this quantity which is defined by

$$||e_p||^2 = \int\limits_0^T \int\limits_0^{L_1} \left(\text{Re}\big(\eta(y,\tau) - \hat{\eta}_p(y,\tau)\big) \right)^2 dy d\tau, \tag{2.44a}$$

$$||e_c||^2 = \int\limits_0^T \int\limits_{L_1}^1 \left(\text{Re}\big(\eta(y,\tau) - \hat{\eta}_c(y,\tau)\big) \right)^2 dy d\tau, \tag{2.44b}$$

$$||e|| = \sqrt{||e_p||^2 + ||e_c||^2}, \tag{2.44c}$$

where T is the non-dimensional period of the applied bending moment, meaning that it changes with Ω and $\text{Re}(\bullet)$ is the real part of $(\bullet)$. The functions $\eta(y,\tau)$, $\hat{\eta}_p(y,\tau)$, and $\hat{\eta}_c(y,\tau)$ are from Eqs. (2.28), (2.29), and (2.30), respectively. Due to the complexity of developing an analytic form for these norms, the integrals appearing in the norm expression are numerically evaluated with a high order adaptive quadrature rule to at least an absolute error of 10^{-10} and at least a relative error of 10^{-6}. See Appendix A for a table of all material constants and dimensions used for all of the following tests.

Analysis of the Elastic Beam
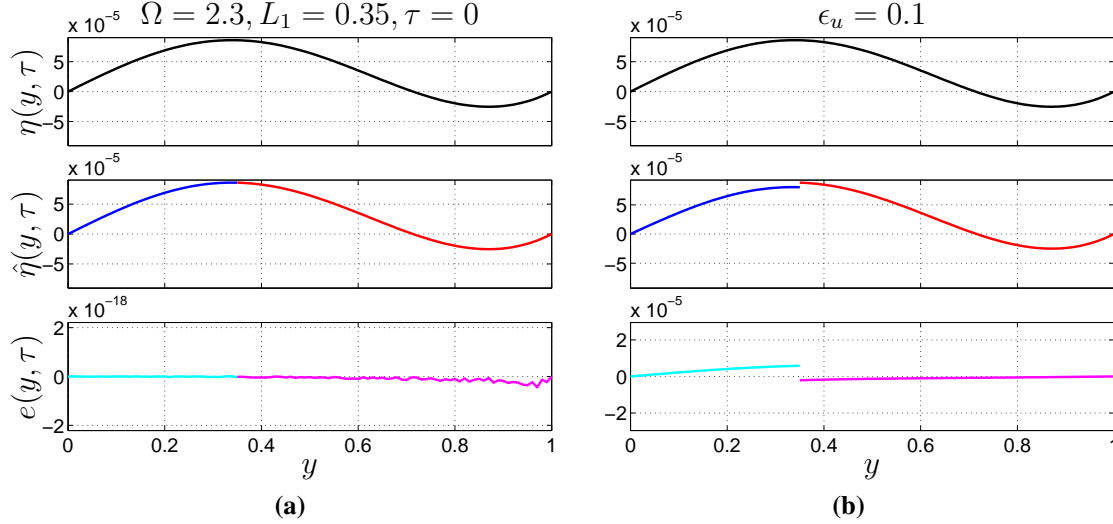
Fig. 2.6 (a) Comparison of the reference elastic pinned-pinned beam to the hybrid elastic pinned-pinned beam with zero interface errors. (b) Comparison of the reference elastic pinned-pinned beam to the hybrid elastic pinned-pinned beam when $\varepsilon_u = 0.1$. Note, $\mu = 3.75 \times 10^{-3}$.

First, Eqs. (2.29) and (2.30) are compared with Eq. (2.28) to verify that the equations do in fact describe the correct system. Note that if all $\varepsilon_{(\bullet)} = 0$ and $d_{(\bullet)} = 0$, then the hybrid system should reduce to the reference system. Figure 2.6(a) shows $\eta(y, 0)$ and $\hat{\eta}(y, 0)$ for one set of parameters and the difference $e(y, 0)$. Note that $e(y, 0)$ is zero to machine precision and thus, to the accuracy to which one can evaluate the expressions, they are identical. For all of the following figures, all error parameters are assumed to be 0 unless noted otherwise in the figure. To show the effects of a displacement error, a 10% error is introduced into the displacement by setting $\varepsilon_u = 0.1$. This value of ε_u was chosen since it represents a relatively large error, and it is useful to see how this large error influences the system error. Later in the analysis, the effect of varying ε_u will be examined. Fig. 2.6(b) shows a discontinuity between the two sides of the interface in the hybrid system and that a noticeable amount of error has been introduced into the entire domain of the hybrid system due to the 10% displacement error at the interface; the large difference in scale of the vertical axes of the error plots in Figs. 2.6(a) and 2.6(b) should be noted.

Effect of Varying Frequency

For specific choices of the parameters $\varepsilon_{(\bullet)}$, $d_{(\bullet)}$, and L_1, Ω is initially swept from 10^{-2} to 10^2 to give a comprehensive look at the effect of the excitation frequency on the hybrid system. Note, that all $\varepsilon_{(\bullet)}$ have similar effects on the error, and thus only ε_u is discussed, with any differences explicitly stated for the other $\varepsilon_{(\bullet)}$. The same holds for $d_{(\bullet)}$. In Fig. 2.7(a),

17

Fig. 2.7 Error Norms: (a) A frequency sweep of the elastic pinned-pinned beam with $\varepsilon_u = 0.1$ on a log-log plot. (b) A zoomed-in plot showing the parasitic spike just to the left of $\Omega = 1$.

Fig. 2.8 Normalized Error Norms: (a) A frequency sweep of the elastic pinned-pinned beam with $\varepsilon_u = 0.1$ on a log-log plot. (b) A zoomed-in plot showing the parasitic spike just to the left of $\Omega = 1$.

which has $\varepsilon_u = 0.1$, the error grows extremely large near the resonant frequencies of the system, i.e. $\Omega = 1, 4, 9, ...$, which is to be expected as the displacement becomes unbounded at these frequencies. Since almost all types of excitation contain a broad spectrum of frequencies, this leads one to conclude that in order for the hybrid system to give usable results all frequencies in the excitation must be less than the first resonant frequency, or $\Omega = 1$. Be-
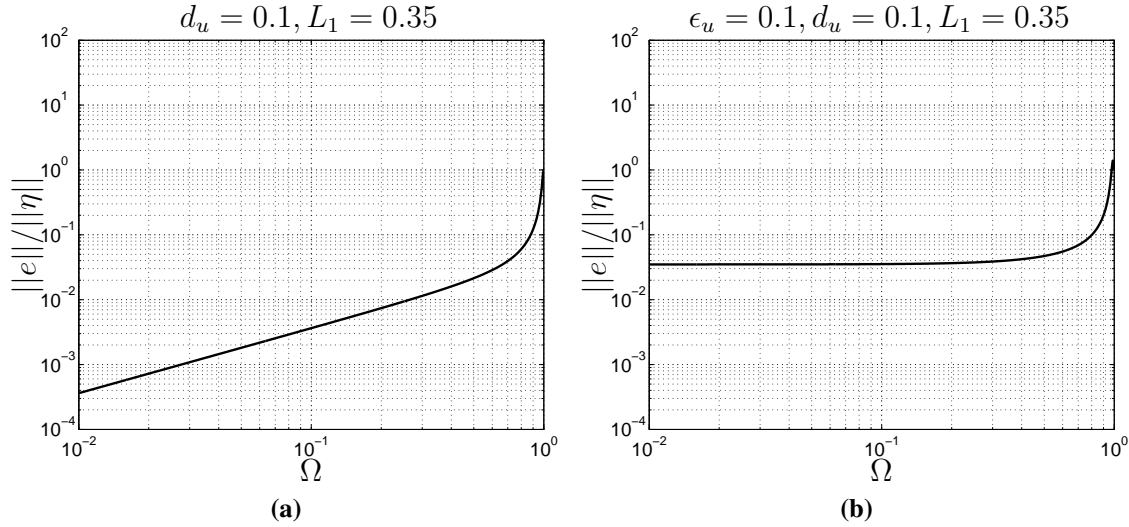
Fig. 2.9 (a) A frequency sweep of the elastic pinned-pinned beam with $d_u = 0.1$ on a log-log plot. (b) A frequency sweep of the elastic pinned-pinned beam with $\varepsilon_u = 0.1$ and $d_u = 0.1$ on a log-log plot.

cause of this, the following analysis will focus on excitation frequencies that are below the first resonant frequency ($\Omega < 1$). Note, this is due to the fact that the system being used for this section has zero damping. In real situations there will be some form of damping that will reduce the effects of the resonant frequencies. An important feature of the hybrid system response is the appearance of parasitic resonant spikes not associated with the actual resonant frequencies of the reference system. Figure 2.7(b) shows one such spike just to the left of $\Omega = 1$. These parasitic spikes are more noticeable for different values of the system parameters. The parasitic spikes oscillate around the resonant frequencies as L_1 changes from zero to one. The amplitude of these oscillations, in the frequency domain, are directly related to the values of $\varepsilon_{(\bullet)}$. It is also helpful to plot the error norm normalized by $\|\eta\|$ to give a sense of the relative magnitude of the error. For the same parameters as considered in Fig. 2.7, this is shown in Fig. 2.8. Comparing Figs. 2.7(a) and 2.8(a), one notes that the drop off in error with increasing frequency disappears. This is due to the fact that $\|\eta\|$ is inversely proportional to $\sqrt{\Omega}$. While the error spikes seem similar in the two cases, an examination of the zoomed-in normalized error in Fig. 2.8(b), cf. Fig. 2.7(b), shows that the hybrid system somewhat tracks the reference system at $\Omega = 1$ but that it clearly possesses a true parasitic resonance just below $\Omega = 1$.

Considering now the effect of time delay errors, Fig. 2.9(a) shows the case of $d_u = 0.1$; the normalized error is now seen to grow for increasing frequencies below $\Omega = 1$. This is in contrast to what is seen in Fig. 2.8(a), where the normalized error held constant with increasing frequency until it approached the first resonant frequency. Further, with the presence of multiple error sources, the behavior is modestly additive. Consider for example non-zero ε_u and d_u as shown in Fig. 2.9(b). In this instance the normalized error, prior to

$\Omega = 1$, behaves exactly as Fig. 2.8(a). This indicates that with multiple non-zero error parameters, the error in the hybrid system will be controlled by the largest individual error for equivalent values of the error parameters.

Effect of Varying ε_u: Magnitude of Tracking Error

The effect of varying ε_u is studied to determine its direct effect on the hybrid system error. As an example, in Fig. 2.10(a), the effect of varying ε_u at $\Omega = 0.8$ is shown. The domain of ε_u extends from -0.5 to 0.5, since it is highly unlikely that an experimental setup will have tracking errors outside of this domain. It can be seen that as ε_u increases in magnitude, the rate of normalized error change decreases. Thus, the only areas of large change in the error come from locations near $\varepsilon_u = 0$. This indicates that there is noticeable error in the hybrid system, even for small ε_u, and trying to reduce the value of ε_u does not have a large effect on the system error, unless ε_u can be brought quite close to zero. Note that varying ε_θ, ε_M, and ε_V produces similar results to those in Fig. 2.10(a).

Fig. 2.10 (a) The effect of varying ε_u for the elastic beam with no other imposed error on a linear-log plot. (b) The effect of varying d_u for the elastic beam with no other imposed error on a linear-log plot.

Effect of Varying d_u: Phase of Tracking Error

The effect of varying d_u is analyzed to determine its direct effect on the error in the hybrid system. Since the effects of d_u are periodic, d_u only goes from 0 to $2\pi/\Omega$. For Ω, a value of 0.8 is chosen for illustrative purposes. As shown in Fig. 2.10(b), the normalized error grows from zero, peaks when d_u is half of the period, and then falls when d_u is equal to a period. Note that varying d_θ, d_M, and d_V produces similar results as in Fig. 2.10(b).

Analysis of the Viscoelastic Beam

As viscoelasticity introduces damping it provides a somewhat more realistic model system. As an initial check of the basic relations, Eqs. (2.29) and (2.30) with $\varepsilon_{(\bullet)} = d_{(\bullet)} = 0$ are compared with the equation for the solution to the reference viscoelastic beam, Eq. (2.28). This comparison is shown in Fig. 2.11. For succinctness, only the real part of the solution is shown.
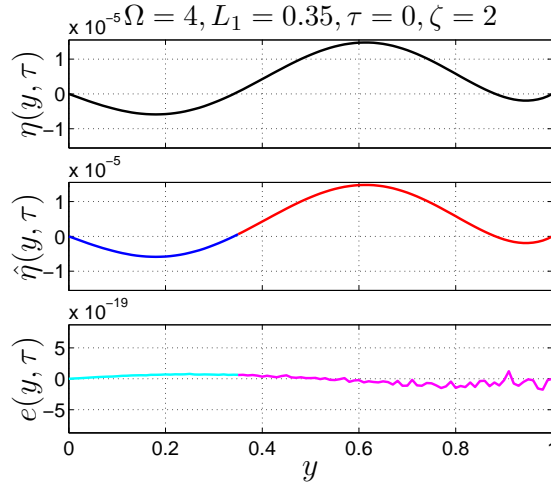
Fig. 2.11   Comparison of the reference viscoelastic pinned-pinned beam to the hybrid viscoelastic pinned-pinned beam with no imposed error.

As it can be seen, only round-off error is present between the hybrid and reference systems. It should be noted that the applied frequency chosen was $\Omega = 4$, which is a resonant frequency of the elastic system, meaning that the displacement is unbounded in the equivalent elastic case. However, in Fig. 2.11, the displacement is bounded due to viscoelastic damping. Note that $\zeta = 2$ implies that the damping peak is located at a frequency of 2. If ζ was chosen to be farther from the applied frequency, the effects of the damping would be significantly less.

Effect of Varying Frequency

As with the elastic beam, a sweep of the frequency is performed from $\Omega = 10^{-2}$ to $\Omega = 10^2$ for various values of ζ. It is noted that the effects of all magnitude errors $\varepsilon_{(\bullet)}$ are nearly identical and thus only ε_u is considered. This is the same for all time delay errors $d_{(\bullet)}$. Consider first the effect of a magnitude error ε_u as shown in Fig. 2.12(a). One notes that, depending on the value of ζ, the error is bounded to differing degrees at all of the resonant of the elastic case. In what follows, focus will be paid to frequencies less than 10 ($\Omega < 10$). Similar to the elastic beam case, there are parasitic resonant spikes near the resonant frequencies, but only when the drive frequency is far from the damping frequency; one of these parasitic spikes is shown in Fig. 2.12(b), but only for the $\zeta = 2000$ curve. In the other three curves, any possible parasitic spikes are mollified by the viscoelastic damping.
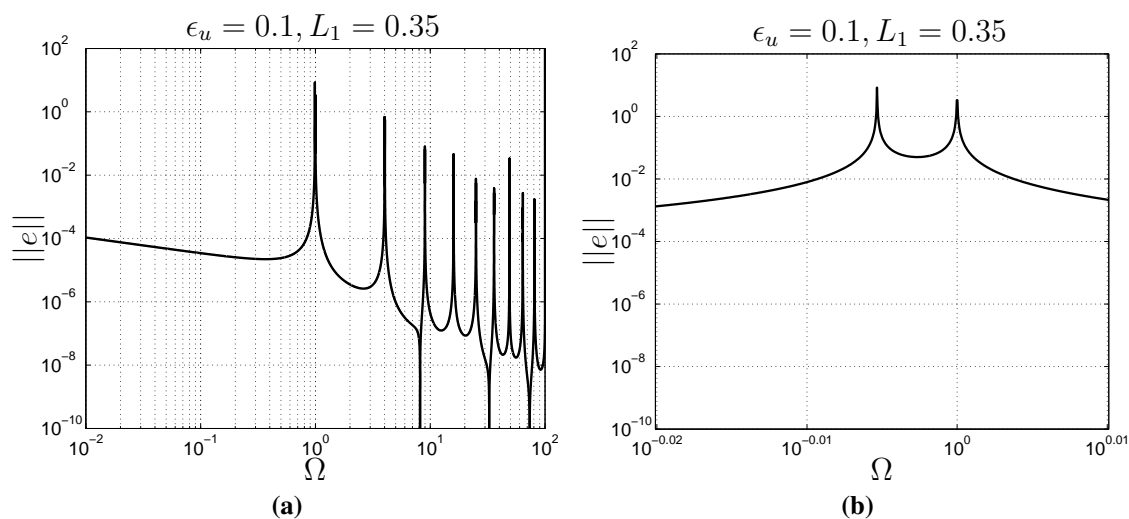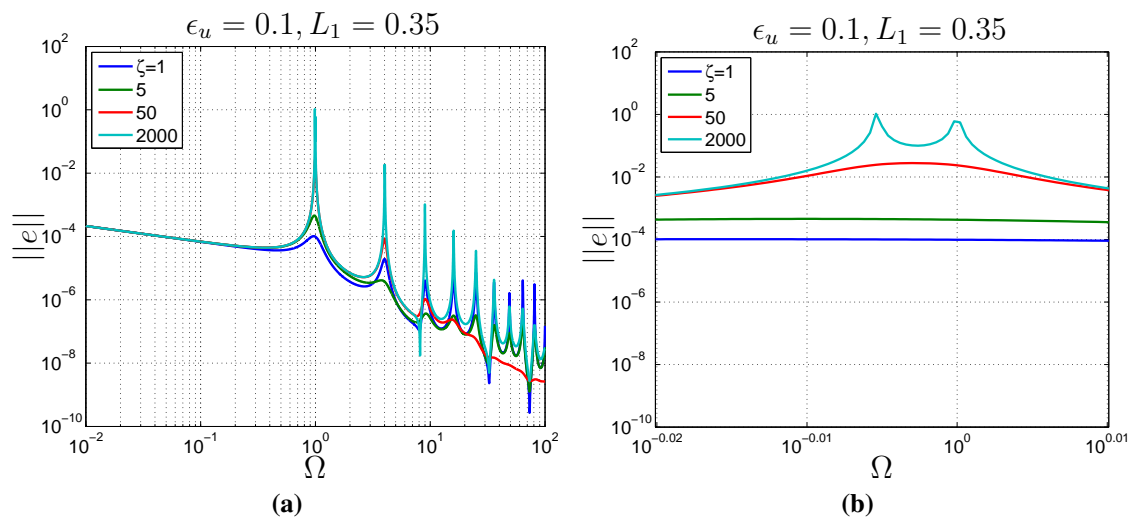
Fig. 2.12 Error Norms: (a) A frequency sweep of the viscoelastic pinned-pinned beam with $\epsilon_u = 0.1$ on a log-log plot for various values of ζ. (b) A zoomed-in plot of the parasitic resonant spike to the left of $\Omega = 1$.
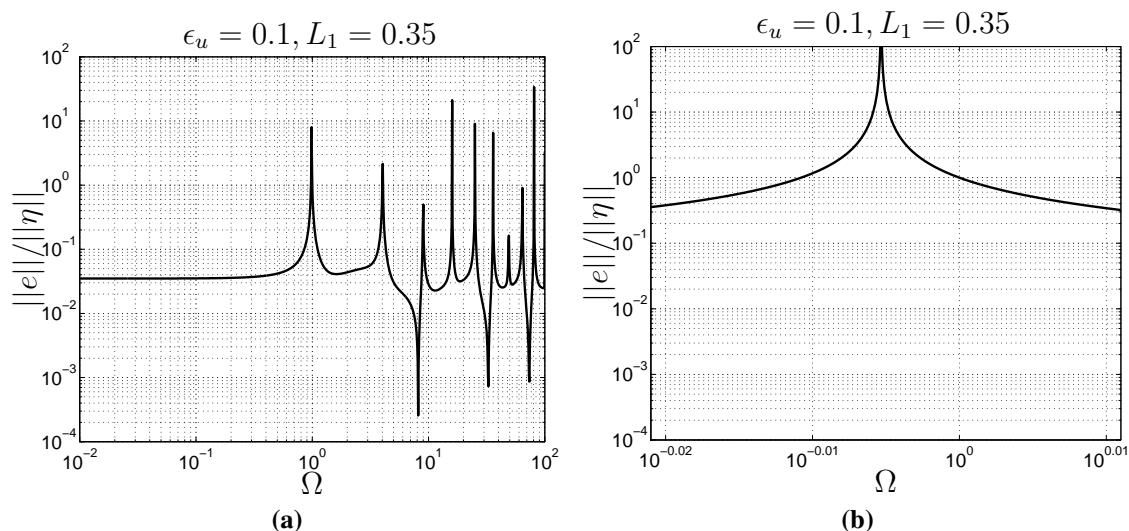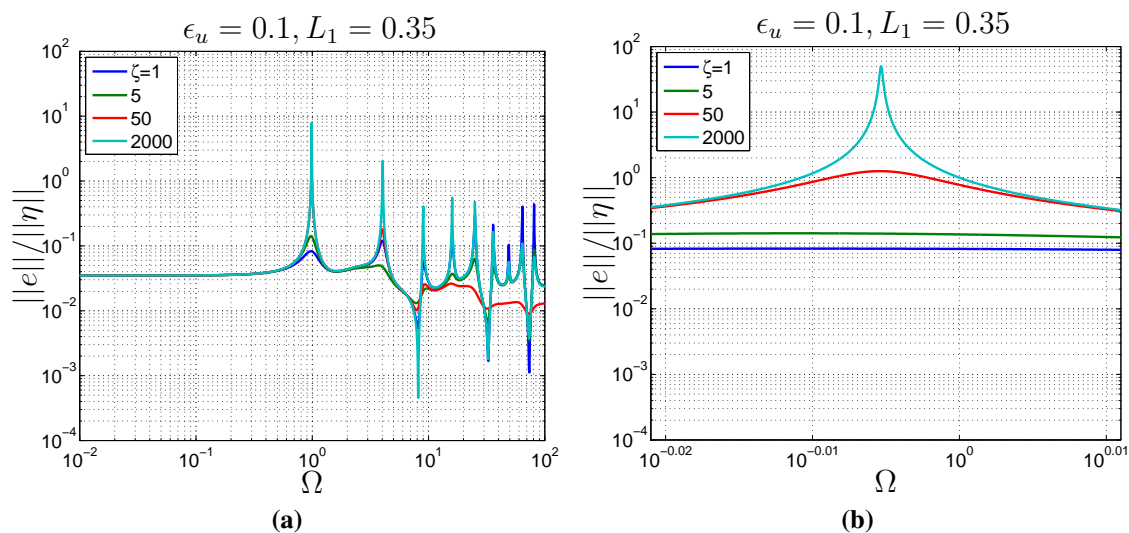

Fig. 2.13 Normalized Error Norms: (a) A frequency sweep of the viscoelastic pinned-pinned beam with $\varepsilon_u = 0.1$ on a log-log plot for various values of ζ. (b) A zoomed-in plot of the parasitic resonant spike to the left of $\Omega = 1$.

When present, these parasitic spikes oscillate around the resonant frequency peaks as L_1 grows from zero to one and the amplitude of these oscillations are related to the value of $\varepsilon_{(\bullet)}$ just as in the elastic case. As before, normalized error plots are helpful for interpreting the results as shown in Fig. 2.13. The general interpretations from the elastic case are

seen also to hold here with the caveat that the placement of damping peaks near (elastic) resonances will reduce errors. If one instead introduces phase error, d_u (see Fig. 2.14), one observes behavior similar to the elastic case – again with the same caveat. When the applied frequency is near the damping frequency, the error is reduced around the resonant frequencies. When the applied frequency is far from the damping frequency, the error curves resemble those for the elastic case. Also, similar to the elastic case below $\Omega = 1$, the error behaves the same as in Figs. 2.8(a) and 2.9(a).
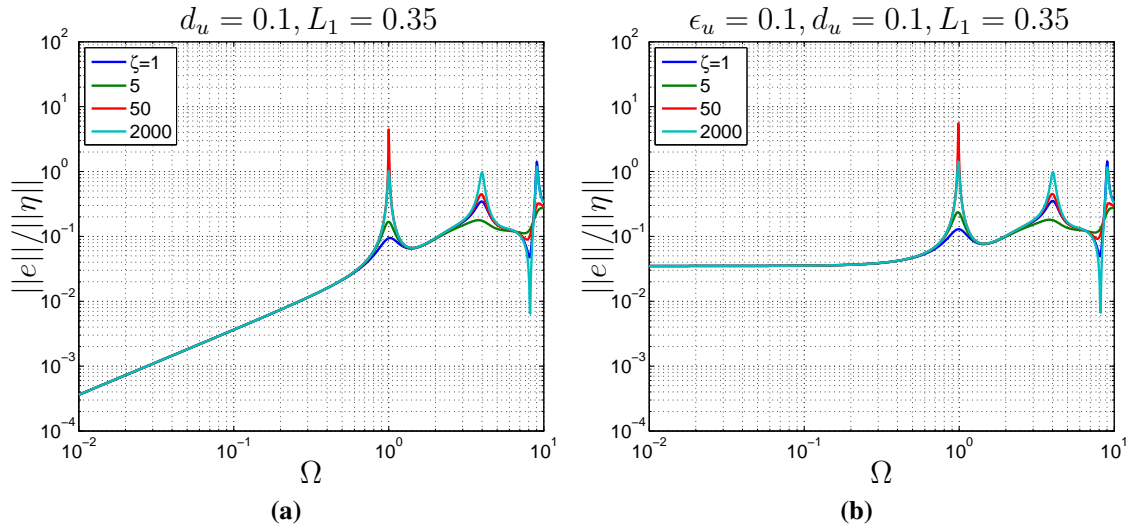
Fig. 2.14   (a) A frequency sweep of the viscoelastic pinned-pinned beam with $d_u = 0.1$ on a log-log plot with varying ζ. (b) A frequency sweep of the viscoelastic pinned-pinned beam with $\varepsilon_u = 0.1$ and $d_u = 0.1$ on a log-log plot with varying ζ.

In order to determine how the error parameters interact in the viscoelastic case, two error parameters are applied to the hybrid system. Figure 2.14(b) has $\varepsilon_u = 0.1$ and $d_u = 0.1$. Below $\Omega = 1$, the normalized error is seen to be consistent with Fig. 2.13(a) and not with Fig. 2.14(a). This indicates that the larger error of the individual error parameters controls the error of the system with multiple non-zero error parameters, which is consistent with the elastic beam case. Further inspection of Figs. 2.13(a) and 2.14 reveals a sharp drop in the error to the left of $\Omega = 10$. This drop in error occurs when $\sin(\kappa L_1) = 0$. In fact for non-zero ε_u, ε_M, d_u, and d_M error drops occur whenever $\sin(\kappa L_1) = 0$. For non-zero ε_θ, ε_V, d_θ, and d_V such error drops occur whenever $\cos(\kappa L_1) = 0$. These observations also hold for the elastic case but are largely irrelevant there since in the elastic case one should never exceed $\Omega = 1$.

Effect of Varying ε_u: Magnitude of Tracking Error

To understand the effect of varying ε_u in the viscoelastic case, consider the fixed frequency $\Omega = 0.8$ at multiple values for ζ within the range of -0.5 to 0.5. As shown in

Fig. 2.15(a), the shape of the error curves are identical to the one in Fig. 2.10(a). However, the curve for $\zeta = 1$ is ever so slightly below the rest of the curves due to the fact that the damping frequency is close to the excitation frequency. Also, as in the elastic case, the error changes rapidly for small ε_u and levels off as ε_u grows in magnitude. The effect of varying ε_θ, ε_M, and ε_V are similar and thus are not shown.
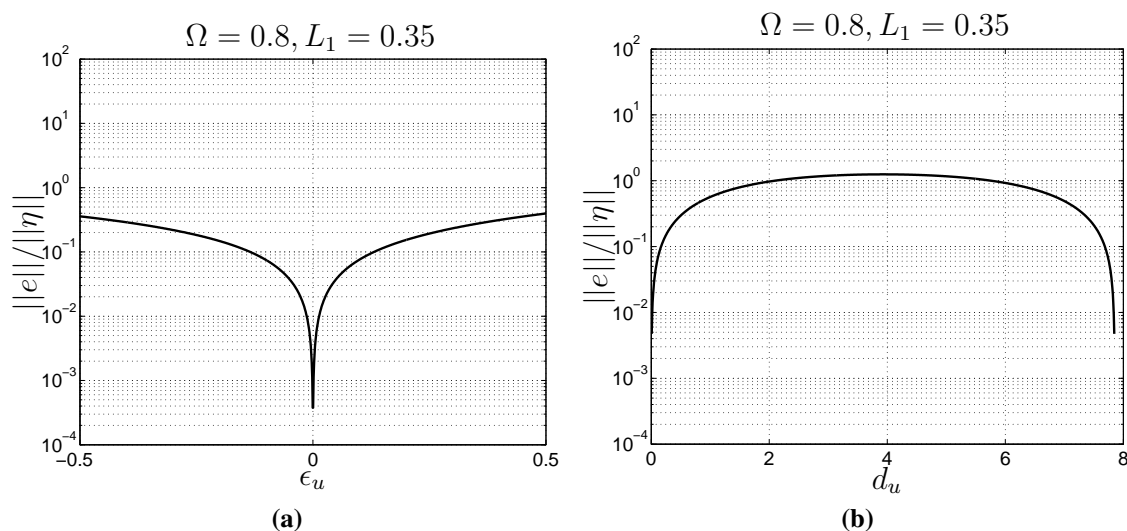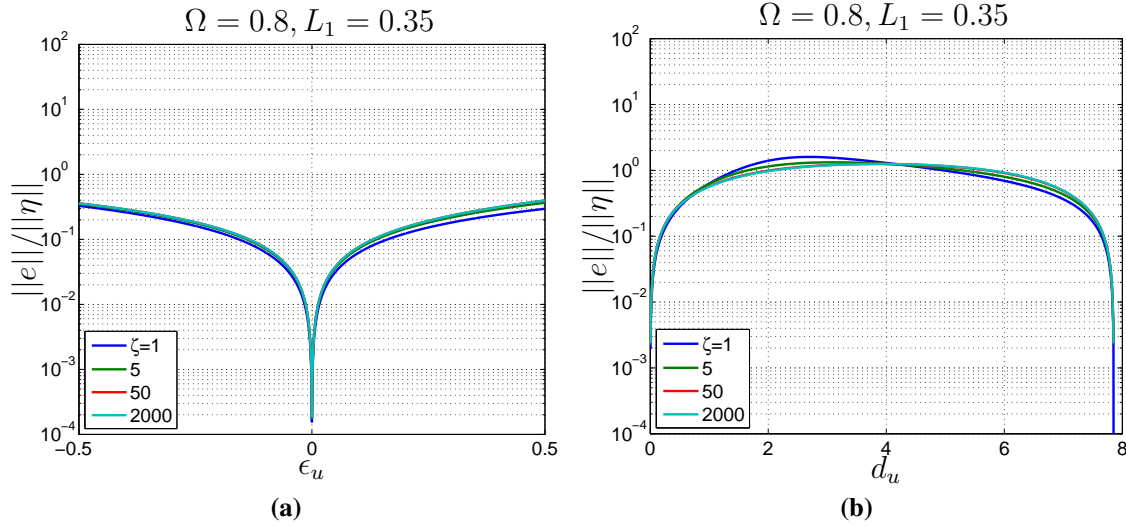

Fig. 2.15 (a) The effect of varying ε_u for the viscoelastic beam with no other imposed error on a linear-log plot. (b) The effect of varying d_u for the viscoelastic beam with no other imposed error on a linear-log plot.

Effect of Varying d$_u$: Phase of Tracking Error

The effect of varying d_u in the viscoelastic case is shown in Fig. 2.15(b). As noted earlier, the effects of d_u are periodic over the range 0 to $2\pi/\Omega$. As a concrete example, Fig. 2.15(b) shows the case of $\Omega = 0.8$. When the applied frequency is far from the damping frequency, the curves behave similar to that of the elastic case, cf Fig. 2.10(b). However, when the damping frequency is closer to the applied frequency, the error, while remaining essentially the same, develops a slight asymmetry relative to the center of the range as seen with the curves for $\zeta = 1$ and $\zeta = 5$. Varying d_θ, d_M, and d_V produces similar results.

Note that in the viscoelastic case, when the applied frequency is far from the damping frequency, the error curves behave in the same manner as the elastic case. This is to be expected, because away from the damping frequency, the viscoelastic equations approach the elastic ones. Finally, note that almost all conclusions gained from the elastic case are repeated for the viscoelastic case, except for special treatment of the parameter ζ.

2.6 Conclusions

The analysis in this chapter demonstrates the theoretical performance of hybrid simulation for an elastic and a viscoelastic beam for the special case where the only errors that are present are those associated with the interface mismatch (systematic errors) of the hybrid system. A harmonic excitation was applied and only the steady-state solution was studied. Our analysis ignores any transient response that may occur in experimental implementations of hybrid simulation. The results show that the resonant frequencies have an over sized impact on the error of the simulation system. Thus, in order for real-time hybrid simulation to be effective as a simulation technique, one must be aware of the forcing frequencies, and keep them below the first resonant frequency for the elastic case or possibly near the damping frequency in the viscoelastic case. The error due to $\varepsilon_{(\bullet)}$ grows quickly around $\varepsilon_{(\bullet)} = 0$ and reaches a large error value for small $\varepsilon_{(\bullet)}$ values. Thus, it is somewhat impractical to reduce the $\varepsilon_{(\bullet)}$ parameters in order to reduce the error in the system, because unless one could make the $\varepsilon_{(\bullet)}$ values quite small, the system error does not significantly change. All of the results stated in the analysis section have also been corroborated with hybrid formulations for an elastic and a viscoelastic axially loaded bar [17] as well as for a classical elastic Kirchhoff-Love plate [4]. This indicates that there are universal errors that occur in hybrid simulation, even for simple one-dimensional and two-dimensional problems. Awareness of the causes of these errors can allow for real-time hybrid simulations to be conducted in a way that reduces or even prevents these errors.

In this chapter it was assumed that $\varepsilon_{(\bullet)}$ and $d_{(\bullet)}$ are constants. However, this is not always the case, they may in fact be functions of the frequency, such that at higher frequencies the time-delay or magnitude error may increase. To include this effect, one could introduce models of the form

$$d_{\bullet} = \frac{d_0}{\left(1 + \exp(\Omega_0 - \Omega)\right)^2}, \tag{2.45}$$

where d_0 is the maximum time delay and Ω_0 is the frequency of maximum growth rate [4]. Similar equations can be applied to $\varepsilon_{(\bullet)}$. Such models modify the details of the error responses; however, the trends remain fundamentally the same.

This chapter considered a single homogeneous linear material that could be modeled by Eq. (2.14). This is not always the case for an experimental setup of hybrid simulation. For example, many hybrid simulation setups are for many bars and beams at the same time, each interacting with the whole system [33, 43]. In such cases analytic response solutions are likely to not be available but one does not expect the observed general trends to be altered.

The error measure that has been focused on was the L^2-norm of the displacement error but that only shows one part of error in the system. The error in the rotation, shear force, and bending moment can also be studied with the use of Sobolev-seminorms on the displacement field [36]. Understanding the error in these quantities is as important as understanding the error in the displacement because in some situations these quantities can be

of equal or even greater importance to the structural and mechanical behavior of a system than the displacement [22].

Chapter 3

Hybrid Simulation Theory Applied to the Damped, Driven Nonlinear Pendulum

3.1 Introduction

In this chapter, the previous framework is applied to a nonlinear dynamical system in order to understand the behavior of hybrid-simulation in the presence of kinematic nonlinearities. As a model problem the damped, driven nonlinear pendulum is used; see [2] for an in depth analysis of the dynamics of this system. This system is one of the most basic nonlinear systems that has a clear physical representation. Despite the simplicity of this system, it has a wide variety of properties that make it interesting to study. For instance, this system exhibits a rich dynamical response with both periodic and chaotic trajectories; see [58] for a discussion on these types of trajectories. These two behaviors can help show how a hybrid split affects the overall dynamics of a nonlinear mechanical system. Also, a spring-mass-damper actuator system which is controlled by a PI controller is used to connect the two hybrid interfaces. This setup for the hybrid system gives a more advanced representation of the hybrid system in comparison to the constant error methodology used in [4, 20].

3.2 Damped, Driven Nonlinear Pendulum

The Reference System

The first system discussed in this chapter is the reference damped, driven nonlinear pendulum; a diagram of which is shown in Fig. 3.1. The pendulum consists of a uniform rigid rod of mass m and length ℓ that rotates about the point O. There is an applied moment $M(t)$ at O, and there is linear viscous damping at O with damping constant c. The kinetic

Fig. 3.1 The damped, driven nonlinear pendulum with a rigid body rotating about O with applied moment $M(t)$.

energy of the system is given by

$$T = \frac{m\ell^2}{6}\dot{\theta}^2,$$
(3.1)

and the potential energy is given by

$$U = mg\left(\frac{\ell}{2} - \frac{\ell}{2}\cos(\theta)\right).$$
(3.2)

Using Lagrange's prescription for finding the equations of motion [48] one has

$$\frac{d}{dt}\left(\frac{\partial T}{\partial \dot{\theta}}\right) - \frac{\partial T}{\partial \theta} + \frac{\partial U}{\partial \theta} = M_{nc},$$
(3.3)

where

$$M_{nc} = -c\dot{\theta} + M(t).$$
(3.4)

This gives

$$\frac{m\ell^2}{3}\ddot{\theta} + c\dot{\theta} + mg\frac{\ell}{2}\sin(\theta) = M(t),$$
(3.5)

the equation that determines the true motion of the system.

The Hybrid System

Next, the hybrid pendulum is developed; a diagram of which is shown in Fig. 3.2. In this case, the rigid body is split into two distinct bodies with distinct angles of rotation, θ_c
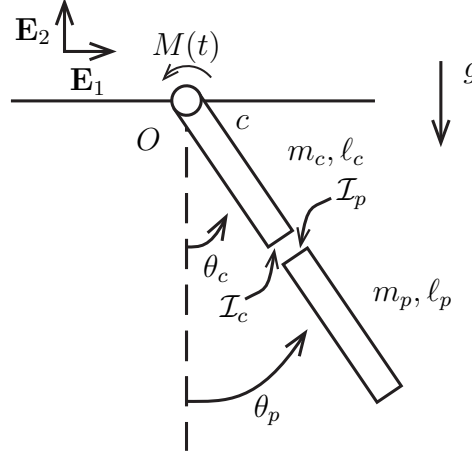
Fig. 3.2   The hybrid pendulum with the rigid body split into two pieces rotating
about O with applied moment $M(t)$.

and θ_p, but both bodies still rotate about O. Also, the lengths $\ell_p + \ell_c = \ell$, and the masses
$m_p = \frac{\ell_p}{\ell}m$, and $m_c = \frac{\ell_c}{\ell}m$, thus $m_p + m_c = m$. The kinetic energy is given by

$$\hat{T} = \frac{m_c\ell_c^2}{6}\dot{\theta}_c^2 + \left(\frac{m_p\ell_p^2}{6} + \frac{m_c\ell_p^2 + m_p\ell_c^2}{2} \right)\dot{\theta}_p^2, \tag{3.6}$$

and the potential energy is given by

$$\hat{U} = m_cg\left(\frac{\ell_c}{2} - \frac{\ell_c}{2}\cos(\theta_c) \right) + m_pg\left(\left(\ell_c + \frac{\ell_p}{2} \right) - \left(\ell_c + \frac{\ell_p}{2} \right)\cos(\theta_p) \right), \tag{3.7}$$

where the hat, $\hat{\bullet}$, represents a quantity in the hybrid system. Lagrange's prescription is
applied with respect to θ_c and θ_p, which is

$$\frac{d}{dt}\left(\frac{\partial\hat{T}}{\partial\dot{\theta}_i} \right) - \frac{\partial\hat{T}}{\partial\theta_i} + \frac{\partial\hat{U}}{\partial\theta_i} = \hat{M}_{nci}, \tag{3.8}$$

for $i = c, p$, where

$$\hat{M}_{ncc} = -c\dot{\theta}_c + M(t) + M_c, \qquad \hat{M}_{ncp} = M_p. \tag{3.9}$$

Here, M_c is the moment at $\mathcal{I}_c$ and M_p is the moment at $\mathcal{I}_p$. In this setup, M_c is an input to
the computational model and M_p is measured by sensors. Expanding Eq. (3.8) gives

$$\frac{m_c\ell_c^2}{3}\ddot{\theta}_c + c\dot{\theta}_c + m_cg\frac{\ell_c}{2}\sin(\theta_c) = M(t) + M_c, \tag{3.10}$$

and

$$\left(\frac{m_p\ell_p^2}{3} + m_c\ell_p^2 + m_p\ell_c^2 \right)\ddot{\theta}_p + m_pg\left(\ell_c + \frac{\ell_p}{2} \right)\sin(\theta_p) = M_p. \tag{3.11}$$

It is noted that, in the ideal setting with no sensor error, $M_c = -M_p$. This assumption is made so the focus can be on the systematic errors rather than sensor errors. Doing so allows Eqs. (3.10) and (3.11) to be combined into a single equation, given by

$$\frac{m_c \ell_c^2}{3} \ddot{\theta}_c + \left(\frac{m_p \ell_p^2}{3} + m_c \ell_p^2 + m_p \ell_c^2 \right) \ddot{\theta}_p + c\dot{\theta}_c$$

$$+ m_c g \frac{\ell_c}{2} \sin(\theta_c) + m_p g \left(\ell_c + \frac{\ell_p}{2} \right) \sin(\theta_p) = M(t). \tag{3.12}$$

However, at this point, there is only one equation, Eq. (3.12), and two unknowns, θ_c and θ_p. To get a second equation, a model for the sensor and actuator system that connects the two bodies is needed. For this chapter, this is modeled as a spring-mass-damper system controlled by a PI controller [47]. The use a spring-mass-damper was chosen purely for its mechanical simplicity and ease of understanding. The spring-mass-damper system can be easily used to introduce phase and magnitude errors – known hybrid simulation errors [9, 56, 67] – at the hybrid interface while still allowing one to have an analytical model that can be solved using standard numerical techniques, such as the Runge-Kutta methods. For the model chosen, the definition from the previous chapter for internal boundary conditions is used, or

$$\underline{D}_c[\hat{\mathbf{u}}_c]\Big|_{\mathcal{I}_c} = \underline{D}_p[\hat{\mathbf{u}}_p]\Big|_{\mathcal{I}_p}. \tag{3.13}$$

In this case $\hat{\mathbf{u}}_c$ and $\hat{\mathbf{u}}_p$ are given by

$$[\hat{\mathbf{u}}_c] = \left[\theta_c \right], \qquad [\hat{\mathbf{u}}_p] = \left[\theta_p \right], \tag{3.14}$$

and the operators $\underline{D}_c[\hat{\mathbf{u}}_c]$ and $\underline{D}_p[\hat{\mathbf{u}}_p]$ have the following definitions:

$$\underline{D}_c[\hat{\mathbf{u}}_c] = \left(k_a k_i + \left(k_a k_p + c_a k_i \right) \frac{d}{dt} + c_a k_p \frac{d^2}{dt^2} \right) \hat{\mathbf{u}}_c, \tag{3.15}$$

and

$$\underline{D}_p[\hat{\mathbf{u}}_p] = \left(k_a k_i + \left(k_a (1 + k_p) + c_a k_i \right) \frac{d}{dt} + \left(c_a (1 + k_p) \right) \frac{d^2}{dt^2} + m_a \frac{d^3}{dt^3} \right) \hat{\mathbf{u}}_p, \tag{3.16}$$

where the parameters m_a, c_a, and k_a are the mass, damping constant, and stiffness of the spring-mass-damper system used to model the actuator. The parameters k_p and k_i are the proportional and integral gains of the PI controller. Applying these definitions ultimately leads to

$$c_a k_p \ddot{\theta}_c + (k_a k_p + c_a k_i) \dot{\theta}_c + k_a k_i \theta_c \tag{3.17}$$
$$= m_a \dddot{\theta}_p + (c_a (1 + k_p)) \ddot{\theta}_p + (k_a (1 + k_p) + c_a k_i) \dot{\theta}_p + k_a k_i \theta_p.$$

Thus, the equations of motion for the hybrid system are given by Eqs. (3.12) and (3.17). While the PI controller has been used in previous works [65], it is emphasized that the PI controller is only used here for concreteness. The entire exercise is easily repeatable with alternate control methodology; see e.g. [22, 43]. The controller that one should employ in an actual experiment is based on the experimental setup that is used, and one that minimizes errors that are important to problem at hand (amongst those metrics highlighted in this chapter and perhaps others of physical significance to the researcher). For these reasons, alternative control schemes are not discussed further in this chapter.

Non-Dimensionalization

For further analysis, it is beneficial to non-dimensionalize Eqs. (3.5), (3.12), and (3.17). In order to do this, the following non-dimensional quantities are defined:

$$\tau = t\sqrt{\frac{g}{\ell}}, \tag{3.18a}$$

$$L_c = \frac{\ell_c}{\ell}, \quad L_p = \frac{\ell_p}{\ell}, \tag{3.18b}$$

$$M_c = \frac{m_c}{m} = L_c, \quad M_p = \frac{m_p}{m} = L_p, \tag{3.18c}$$

$$\gamma = \frac{c}{m\ell\sqrt{g\ell}}, \tag{3.18d}$$

$$\mu(\tau) = \frac{M\left(t = \tau\sqrt{\frac{\ell}{g}}\right)}{mg\ell}, \tag{3.18e}$$

$$M_a = \frac{m_a}{m}, \quad \gamma_a = \frac{c_a}{m}\sqrt{\frac{\ell}{g}}, \quad K_a = \frac{k_a\ell}{mg}, \tag{3.18f}$$

$$K_p = k_p, \quad K_i = k_i\sqrt{\frac{\ell}{g}}. \tag{3.18g}$$

Using Eq. (3.18), Eqs. (3.5), (3.12), and (3.17) are rewritten as,

$$\frac{d^2\theta}{d\tau^2} + 3\gamma\frac{d\theta}{d\tau} + \frac{3}{2}\sin(\theta) = 3\mu(\tau), \tag{3.19}$$

$$\frac{L_c^3}{3}\frac{d^2\theta_c}{d\tau^2} + \left(\frac{L_p^3}{3} + L_cL_p\right)\frac{d^2\theta_p}{d\tau^2} + \gamma\frac{d\theta_c}{d\tau}$$
$$+ \frac{L_c^2}{2}\sin(\theta_c) + \left(L_pL_c + \frac{L_p^2}{2}\right)\sin(\theta_p) = \mu(\tau), \tag{3.20}$$

and

$$\gamma_a K_p \frac{d^2\theta_c}{d\tau^2} + (K_a K_p + \gamma_a K_i)\frac{d\theta_c}{d\tau} + K_a K_i \theta_c \tag{3.21}$$

$$= M_a \frac{d^3\theta_p}{d\tau^3} + (\gamma_a(1+K_p))\frac{d^2\theta_p}{d\tau^2} + (K_a(1+K_p) + \gamma_a K_i)\frac{d\theta_p}{d\tau} + K_a K_i \theta_p.$$

Equations (3.19)-(3.21) are the non-dimensionalized equations of motion for the reference and hybrid systems.

3.3   Analysis

For the analysis, the applied moment is given by

$$\mu(\tau) = \bar{\mu}\cos(\Omega\tau), \tag{3.22}$$

where $\bar{\mu}$ is the non-dimensional magnitude of the applied moment and Ω is the non-dimensional frequency of the applied moment. To start, the constants in the system are set as follows: $L_c = 0.6$, $L_p = 0.4$, $M_a = 0.5$, $\gamma = 0.1$, $\gamma_a = 25$, $K_a = 12.5$, $K_i = 3$, $K_p = 10$. Equations (3.19)-(3.21) are integrated numerically using the Dormand-Prince method, which is a type of the Runge-Kutta ODE solver [15]. A tolerance of 10^{-7} was used when evaluating the Dormand-Prince method. This method is a standard method used to evaluate non-stiff equations with medium accuracy.

Since the reference forced pendulum is a two-state non-autonomous system, the system will exhibit either periodic motion or chaotic motion depending on the values of the parameters, see [50]. The hybrid forced pendulum is a five-state non-autonomous system and will also exhibit either periodic or chaotic motion. If the motion is periodic, the period of the steady-state motion will be an integer multiple of the forcing period, nT, where $n = 1, 2, 3...$ and $T = \frac{2\pi}{\Omega}$; if $n > 1$, this corresponds to an excited subharmonic of period nT (see [32]). In order to determine the character of the motion of the systems, it is useful to employ the use of Lyapunov exponents; see [46]. If the largest Lyapunov exponent is positive, then the system will exhibit chaotic motion. If the largest Lyapunov exponent is 0, then the system will experience periodic motion; see [3]. Also, as long as the sum of all of the Lyapunov exponents is negative, the system is stable in the sense of Lyapunov. The Lyapunov exponents are found using the QR method for small continuous nonlinear systems as outlined by [13] and the FORTRAN code provided by [14] – LESNLS – was modified to calculate the Lyapunov exponents for the systems presented in this chapter. For a thorough discussion on the utility and implementation of the LESNLS code, please review the paper by Dieci et al. [13].

To begin, an examination of how the magnitude of the applied moment determines the behavior of the responses of both the reference and hybrid systems for a fixed frequency of the applied moment is preformed with $\Omega = 1$ for multiple values of $\bar{\mu}$. From this, the systems are determined to be either periodic or chaotic. Figure 3.3 shows the largest Lyapunov

exponent for the reference and hybrid systems as a function of the forcing magnitude. From Fig. 3.3 it is shown that, for the most part, the reference and hybrid systems exhibit the same type of behavior. However, there are a few instances that one system is periodic and the other is chaotic. This indicates that there are three separate cases that one needs to consider when performing an error analysis of the nonlinear pendulum hybrid simulation system: both responses are periodic, both responses are chaotic, and one response is periodic while the other is chaotic.
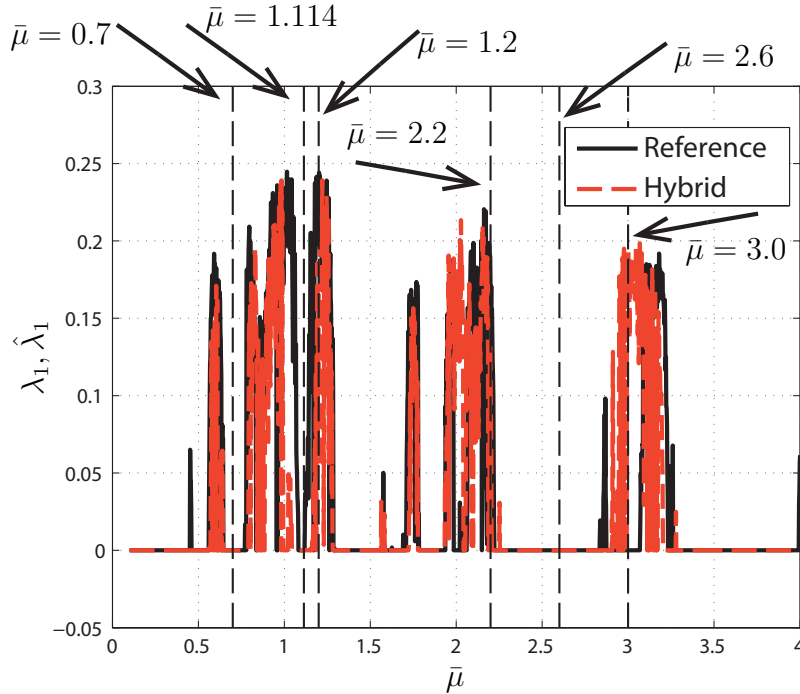
Fig. 3.3 The Lyapunov exponents for the reference, λ_1, and hybrid systems, $\hat{\lambda}_1$, when $\Omega = 1$.

Periodic Reference and Hybrid Systems

The first case analyzed is for when both the reference and hybrid systems are periodic. For this case, an L^2 error is utilized to gauge how well the hybrid system is matching the reference system in the same manner as [20]. The L^2 error is given by

$$E_2(\tau) = \frac{\sqrt{\int_0^\tau L_c\left(\left(\theta - \theta_c\right)^2 + \left(\frac{d\theta}{d\tau} - \frac{d\theta_c}{d\tau}\right)^2\right) + L_p\left(\left(\theta - \theta_p\right)^2 + \left(\frac{d\theta}{d\tau} - \frac{d\theta_p}{d\tau}\right)^2\right)}}{\sqrt{\int_0^\tau \theta^2 + \left(\frac{d\theta}{d\tau}\right)^2}}. \tag{3.23}$$

Note that the L^2 error used for the analysis is normalized with respect to the reference system. Also note that the difference in angles is always taken to be the smallest angular

distance between 0 and 2π. The L^2 error is calculated at three different values of $\bar{\mu}$: $\bar{\mu} = 0.7, 1.114, 2.6$. A careful examination of Fig. 3.3 shows that all three of these values will produce periodic motion in both systems. The L^2 error time series for these three values of $\bar{\mu}$ are shown in Fig. 3.4. This figure shows that when the transients are still present, small τ, the error varies rapidly. However, as τ increases, the error approaches a steady state value. This makes sense because both systems are approaching a periodic solution, thus the difference between the two solutions should be approximately constant. However, as can
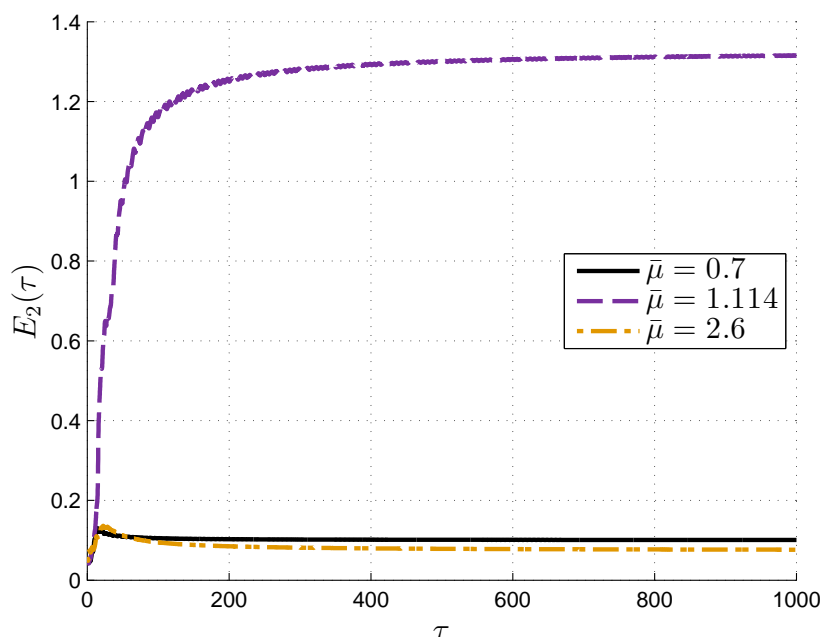
Fig. 3.4 The L_2 error for $\Omega = 1$ for three values of $\bar{\mu}$ with only periodic responses.

be seen in Fig. 3.4, for $\bar{\mu} = 1.114$, the L^2 error approaches a value near 1.3, or 130%. This indicates that the hybrid system is not tracking the reference system at all. Upon further study it is found that the reference system is traveling in a clockwise direction, while the hybrid system is traveling in a counter-clockwise direction. Thus, the hybrid system is matching the response of the reference system, just in the opposite direction. This is the cause of the large L^2 error. In order to more fully study the dynamical response, the state space of the two systems is analyzed, which is shown Fig. 3.5. Note, only θ_c and $\frac{d\theta_c}{d\tau}$ are plotted for clarity in the figures (see Appendix B for similar plots for θ_p and $\frac{d\theta_p}{d\tau}$). From this figure, it can be seen that the state space trajectories are similar in shape, but vary by a rotation in state space. Thus, as long as the exact trajectory is not required, the hybrid response can be useful in understanding the dynamics of the reference system. Note that Fig. 3.5 also clearly shows that subharmonics are being excited in this case.
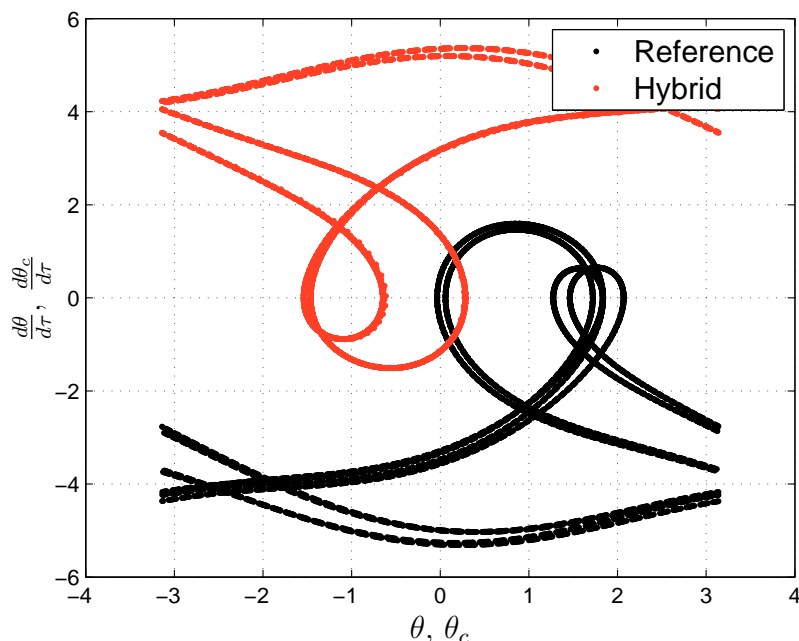
Fig. 3.5   The state space trajectories for the reference and hybrid systems with
$\bar{\mu} = 1.114$.

Chaotic Reference and Hybrid Systems

The next case analyzed is when both systems are chaotic. For the chaotic systems, the L^2 error is no longer a good metric for determining the error in the system. Instead, multiple aspects of the dynamics need to be compared to fully understand the relationship between the reference and hybrid systems. First, the systems are compared visually before comparing them with error metrics. The time series, specifically, the angular velocity time series, is used to make a visual comparison of the reference and hybrid systems. The Poincaré sections of the reference and hybrid systems are then compared. Note, for the plotting the Poincaré sections, the time series was calculated out to $\tau = 10000$, and with $\Omega = 1$, this gives just under 1600 points per Poincaré section. This allows one to compare the nature of the response on a more fundamental level. Two values of $\bar{\mu}$ are chosen for the chaotic case: $\bar{\mu} = 1.2, 2.2$. Again, Fig. 3.3 shows that these values will produce chaotic responses in both systems.

Figures 3.6 and 3.7 show the times series (of the angular velocities) for the systems with $\bar{\mu} = 1.2$ (see Appendix B for $\frac{d\theta_p}{d\tau}$ plots). It is clear that the two systems do not track each other very well. However, looking at Fig. 3.8, which shows the Poincaré sections for both the reference and hybrid systems with $\bar{\mu} = 1.2$, the similarities can easily be seen between the two Poincaré sections. This indicates that even when both systems are chaotic, the fundamental nature of the responses are nearly identical.

Next, the angular velocity time series for when $\bar{\mu} = 2.2$ are shown in Figs. 3.9 and 3.10,
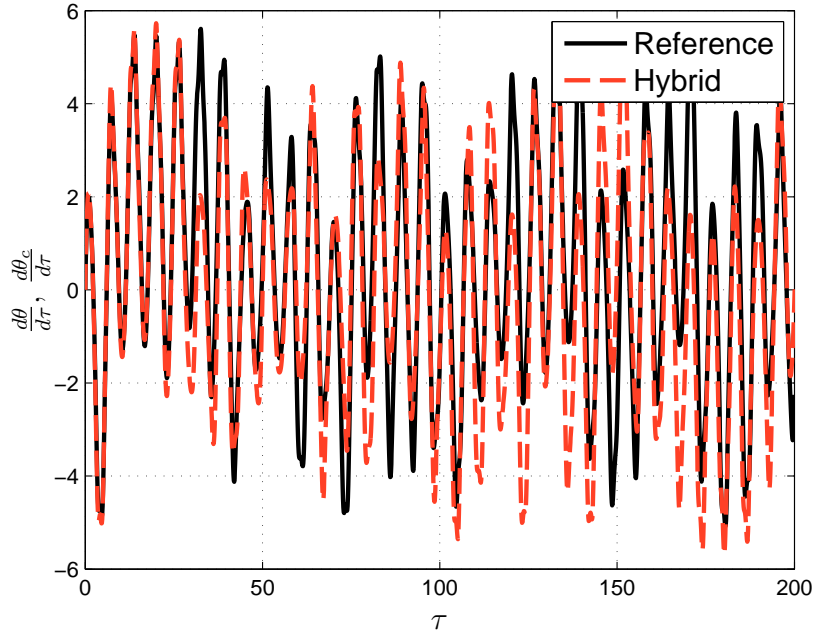
Fig. 3.6   The angular velocity time series of the reference and hybrid systems for $\bar{\mu} = 1.2$.

which show that the time series of the reference and hybrid systems match each other fairly well. However, the corresponding Poincaré sections, shown in Fig. 3.11, show very little correlation. Similar conclusions can be drawn from θ_p and $\frac{d\theta_p}{d\tau}$ as shown in Appendix B. So, even though the time series match well, their Poincaré sections do not. This confirms the need to examine multiple aspects of the dynamics.

Chaos Error Metrics

Besides the above described visual error analysis, three different error metrics were also used to give a numerical value to the error between two chaotic systems. First, a comparison of the Lyapunov exponents of the two systems, which allows for a direct comparison of the level of chaos in each system, as the Lyapunov exponent defines how quickly trajectories will diverge from each other due to small variations in the trajectories; see [29]. The second value compared is the Lyapunov dimension, d_L, which defines the *dimension* of the strange attractor and is calculated by

$$d_L = j + \frac{\lambda_1 + \lambda_2 + \cdots + \lambda_j}{|\lambda_{j+1}|}, \tag{3.24}$$

where j is the largest integer for which $\lambda_1 + \lambda_2 + \cdots + \lambda_j \geq 0$, see [28]. The Lyapunov dimension can be used to classify the complexity of a strange attractor, since a strange attractor
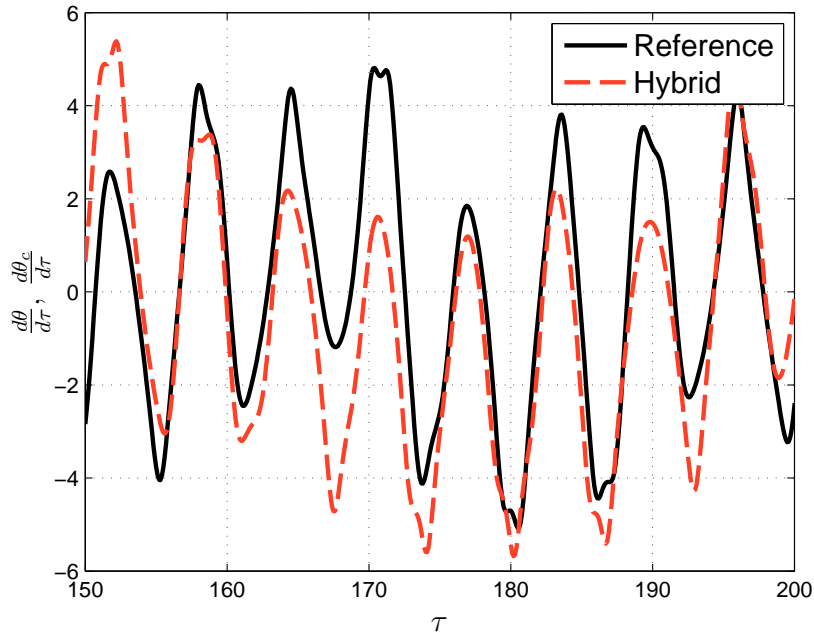
Fig. 3.7   A zoomed-in plot of the angular velocity time series of the reference and hybrid systems for $\bar{\mu} = 1.2$.
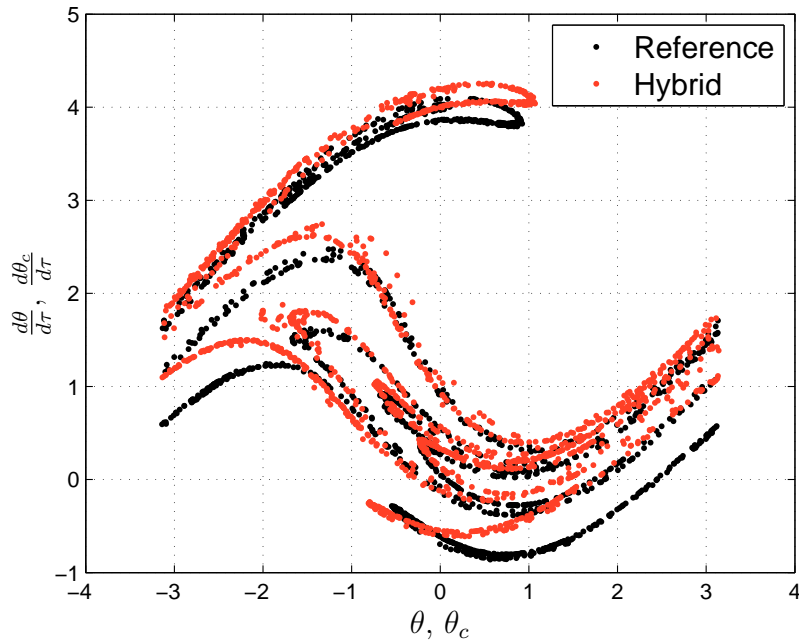
Fig. 3.8   The Poincaré sections of the reference and hybrid systems for $\bar{\mu} = 1.2$.
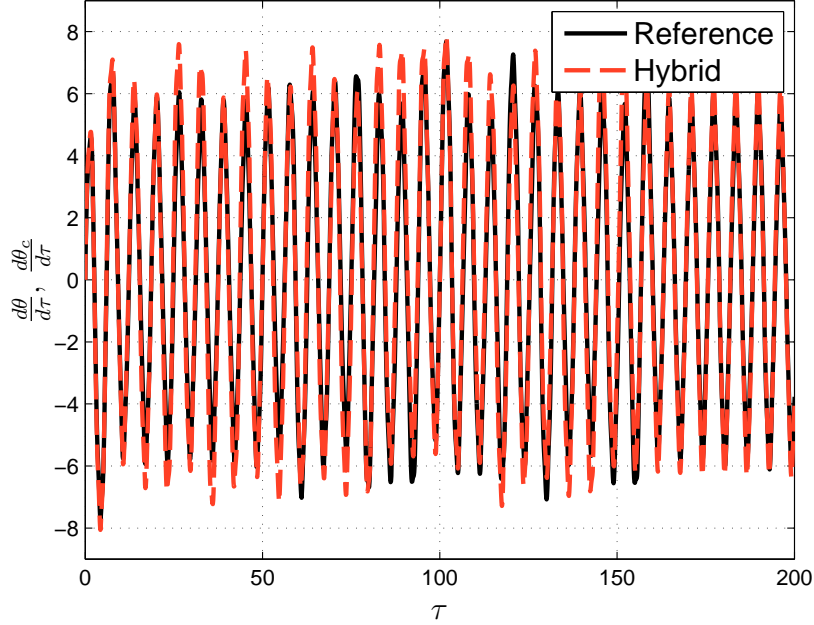
Fig. 3.9   The angular velocity time series of the reference and hybrid systems for
$\bar{\mu} = 2.2$.

will have a fractional dimension, whereas a non-strange attractor will have an integer dimension. All systems in this chapter have $j = 2$. Thirdly, the correlation exponent [30], v, is employed to characterize the chaotic error. The correlation exponent is used to measure the local structure of a strange attractor or Poincaré section; see [31]. The correlation exponent is based on how close the points on a strange attractor or Poincaré section are to one another, which is another measure for the complexity of a strange attractor or Poincaré section. In order to compute the correlation exponent, the correlation integral is calculated,

$$C(r) = \frac{1}{N^2} \sum_{i,j=1,i\neq j}^{N} H(r - |\mathbf{X}_i - \mathbf{X}_j|), \tag{3.25}$$

where $H(x)$ is the Heaviside function, r is the correlation radius, and $\mathbf{X}_i$ are the states of the system at the i-th time step with N time steps. Then using the relation

$$C(r) \propto r^v, \tag{3.26}$$

solve for the correlation exponent, v. In this chapter, the correlation exponent was calculated using the points in the Poincaré section. The errors with respect to these three metrics are calculated as follows:

$$err_\lambda = \frac{|\lambda_1 - \hat{\lambda}_1|}{\lambda_1}, \tag{3.27}$$

38
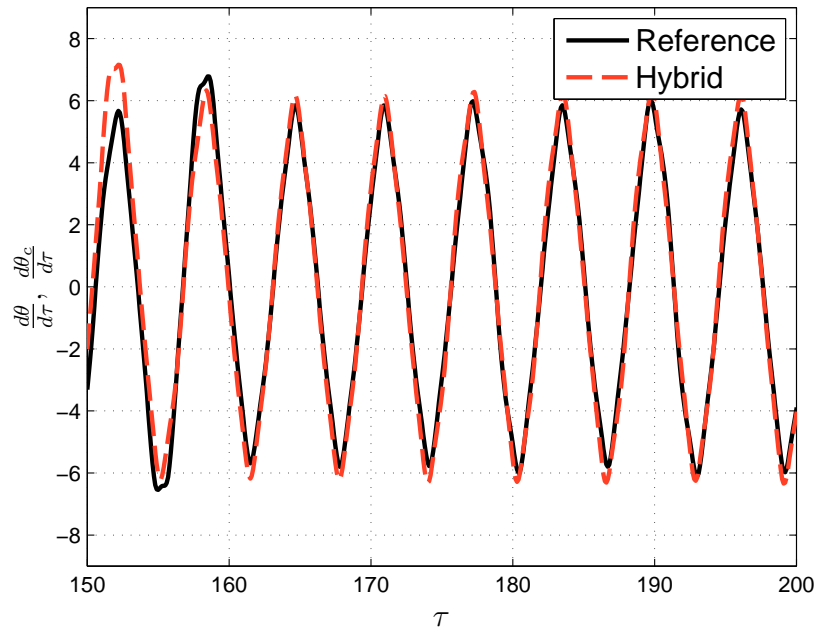
Fig. 3.10 A zoomed-in plot of the angular velocity time series of the reference and hybrid systems for $\bar{\mu} = 2.2$.
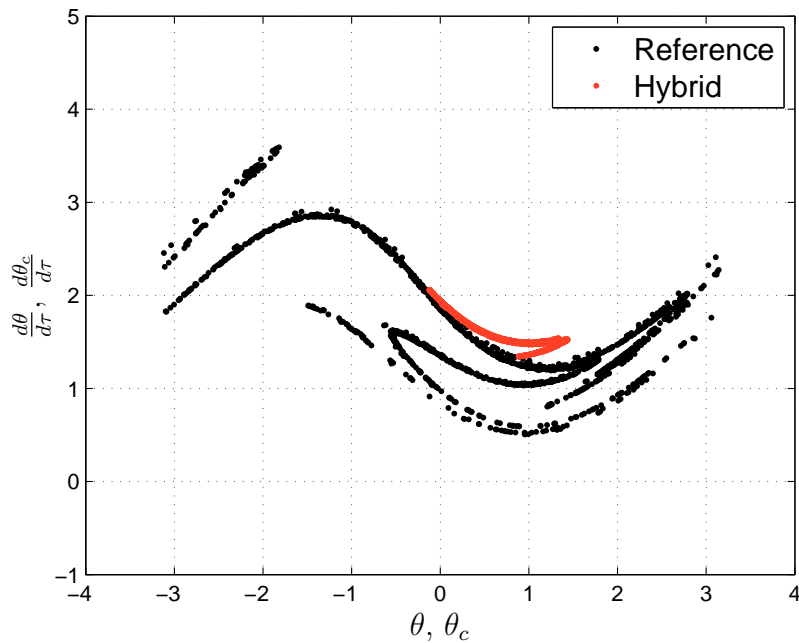
Fig. 3.11 The Poincaré sections of the reference and hybrid systems for $\bar{\mu} = 2.2$.

$$err_{d_L} = \frac{|d_L - \hat{d}_L|}{d_L}, \tag{3.28}$$

and

$$err_v = \frac{|v - \hat{v}|}{v}. \tag{3.29}$$

where the hat, $\hat{\bullet}$, again, represents quantities for the hybrid system. Figures 3.12, 3.13, and 3.14 show these error measures versus applied moment magnitude. Note, points are only calculated for values of $\bar{\mu}$ for which both the reference and hybrid system are chaotic.
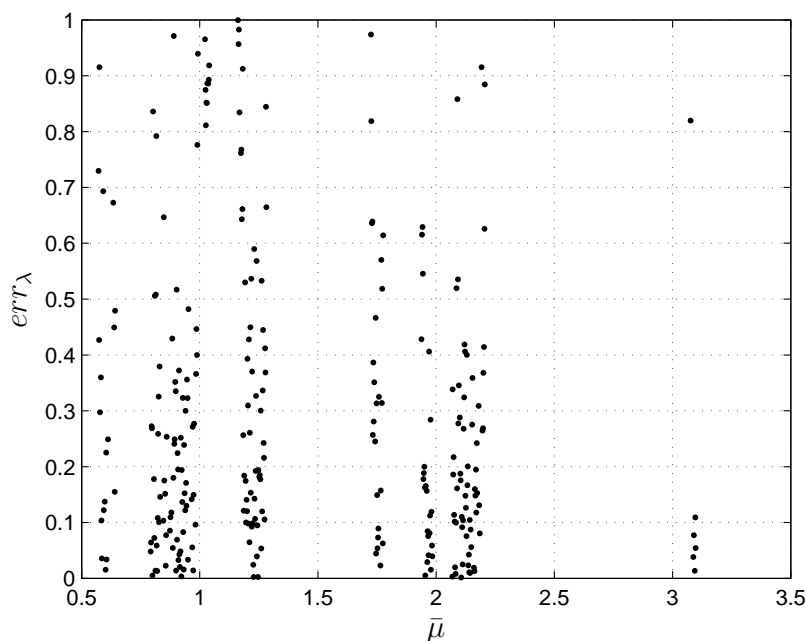
Fig. 3.12 The error between λ_1 and $\hat{\lambda}_1$ as a function of $\bar{\mu}$.

Examining Fig. 3.12, a wide variety of errors in the largest Lyapunov exponents can be seen, however, about half of all errors are less than 0.2, or less than 20%. This shows that about half the time the levels of chaos in both systems are equivalent, yet there are times when the two systems vary greatly. Looking at Fig. 3.13, all of the errors are below 0.4, and a significant portion, more than nine-tenths, are less than 0.2. This shows that there is much less deviation between the Lyapunov dimension of the reference and hybrid systems, indicating that the dimension of their strange attractors stay near one another. From examining Fig. 3.14, it is seen that there is a high density of points below 0.2, about two-thirds of all points are below 0.2. This shows that most of the time the Poincaré sections of the two systems match fairly well, however, there are still instances in which the two systems
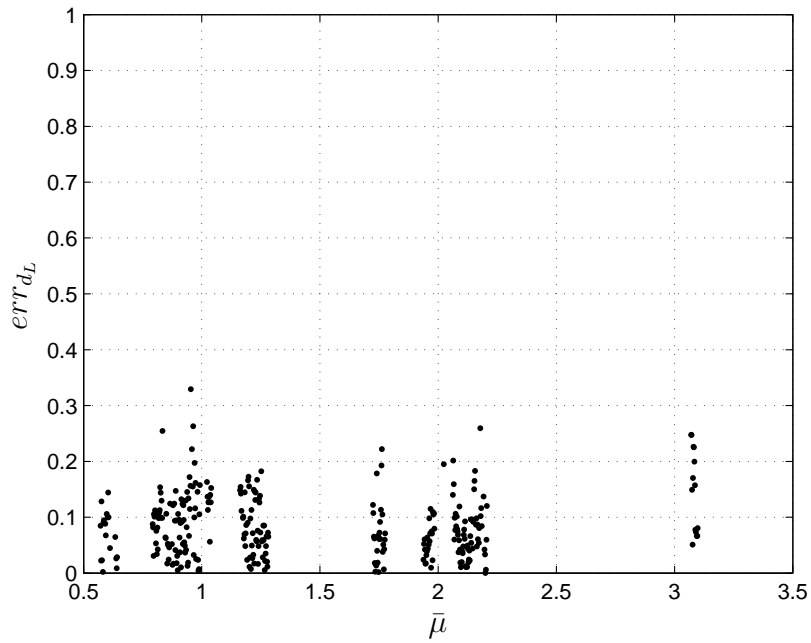
Fig. 3.13   The error in the Lyapunov dimension as a function of $\bar{\mu}$.
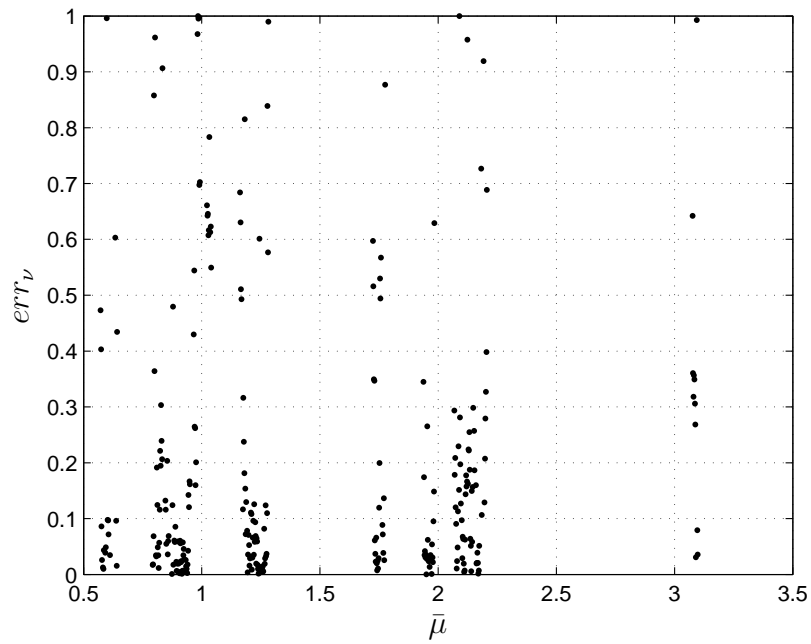
Fig. 3.14   The error in the correlation exponent of the Poincaré sections as a function of $\bar{\mu}$.

do not match well. For the cases which were visually examined above, $err_{\lambda_1} = 0.1203$, $err_{d_L} = 0.1552$, and $err_v = 0.0526$ when $\bar{\mu} = 1.2$, and $err_{\lambda_1} = 0.3680$, $err_{d_L} = 2.810 \times 10^{-4}$, and $err_v = 0.2792$ for $\bar{\mu} = 2.2$. These values again fit with the determination that multiple quantities are needed to properly assess the error between two chaotic responses.

One System Periodic and the Other Chaotic

The third case is when one system has a chaotic response and the other system has a periodic response. In this situation it is not possible to compare the two systems as the L^2 error breaks down for chaotic systems, and the Poincaré section for a periodic system will be a single point, whereas the Poincaré section for a chaotic system will be Cantor-like, see e.g. [50, 52]. For these reasons, it is clear the correlation between the two responses will be nonexistent.

Study of K_i

All of the above analysis was done with specific values of the control parameters. If a value of $K_i = 10$ was used instead, which was arbitrarily chosen, the Lyapunov exponents of the hybrid system match those of the reference system much better, as seen by comparing Fig. 3.3 and Fig. 3.15. This potentially indicates that an increase in the integral gain, K_i, gives better matching between the reference and hybrid systems. To investigate this
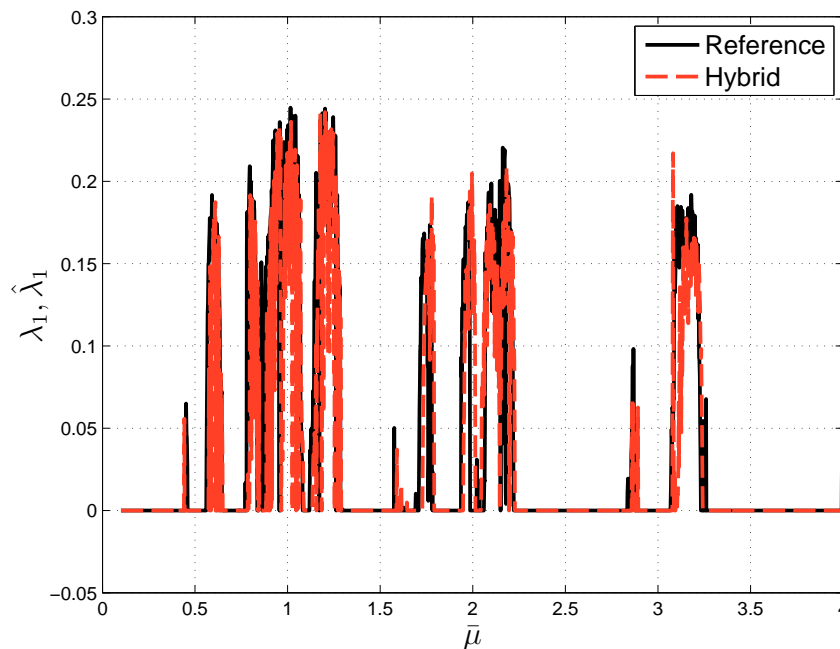
Fig. 3.15 The Lyapunov exponents for the reference and hybrid systems when $K_i = 10$.

further, the effects of changing the integral gain, K_i are examined. In the context of this chapter, holding K_p constant and increasing K_i means the response of the controlled system is quicker, but it becomes more oscillatory and less stable [47]. Thus, as K_i increases, the magnitude error at the hybrid interface increases while the phase error decreases. However, it is noted that this only applies for the simple PI controller used in this chapter. Three specific values of $\bar{\mu}$ are used: $\bar{\mu} = 1.114, 1.2, 3.0$. The first value was chosen because both the hybrid and reference systems were periodic at $K_i = 3$, but the hybrid system is going the opposite direction of the reference system. The second value was chosen because the response is chaotic for both systems at $K_i = 3$. And the third value was chosen because the reference response is periodic, while the hybrid response is chaotic at $K_i = 3$. For analyzing the effect of changing K_i, the hybrid L^2 error is used once the transients have died out and the error has reached steady state:

$$E_2^h(\tau = 1000) = \frac{\sqrt{\int_0^\tau \left(\theta_c - \theta_p\right)^2 + \left(\frac{d\theta_c}{d\tau} - \frac{d\theta_p}{d\tau}\right)^2}}{\sqrt{\int_0^\tau \theta_c^2 + \left(\frac{d\theta_c}{d\tau}\right)^2}}. \tag{3.30}$$

Note that E_2^h is normalized to the top piece of the hybrid pendulum. The hybrid L^2 error determines how well the two pieces of the hybrid pendulum are matching each other and is an error measure that can be applied independent of the chaotic or periodic nature of either system. As seen from Fig. 3.16, as K_i is increased, the hybrid L^2 error decreases for all three values of $\bar{\mu}$, which makes sense because K_i affects the steady state response, thus the two pieces should match better for larger values of K_i, see [47]. However, by looking at the steady state L^2 error in Fig. 3.17, it is noted that the L^2 error does not decrease as K_i is increased, in fact, all three values of $\bar{\mu}$ have different responses to increasing K_i.

For $\bar{\mu} = 1.114$, the error approximately goes between three values as K_i increases. This indicates that even though the hybrid pieces are matching each other better, the hybrid pendulum is not always matching the reference pendulum better. In fact, the highest value represents the hybrid pendulum spinning in the opposite direction of the reference pendulum, the middle value represents the hybrid pendulum spinning in the same direction as the reference pendulum, but taking a long time to reach the steady-state solution, and the low value represents the hybrid pendulum spinning in the same direction as the reference pendulum and reaching the steady-state solution more quickly.

For $\bar{\mu} = 1.2$, the L^2 error is not a good metric for analyzing the error. Instead, the Poincaré sections are used, as shown in Fig. 3.18 (see Appendix B for θ_p and $\frac{d\theta_p}{d\tau}$ plots). From a close comparison of Figs. 3.8 and 3.18, with $K_i = 10$, the Poincaré sections match better than when $K_i = 3$. This indicates that the hybrid response is better for larger values of K_i. Evaluating the error metrics from before, $err_{\lambda_1} = 0.5722$, $err_{d_L} = 0.0919$, and $err_v = 0.0332$. Comparing these values to those found before, the Lyapunov dimension error and correlation exponent error have decreased, while the Lyapunov exponent error has increased. This again indicates the need for multiple metrics to gauge the chaotic response because even though it appears that increasing K_i made the hybrid response better, there is actually a metric in which it became worse.
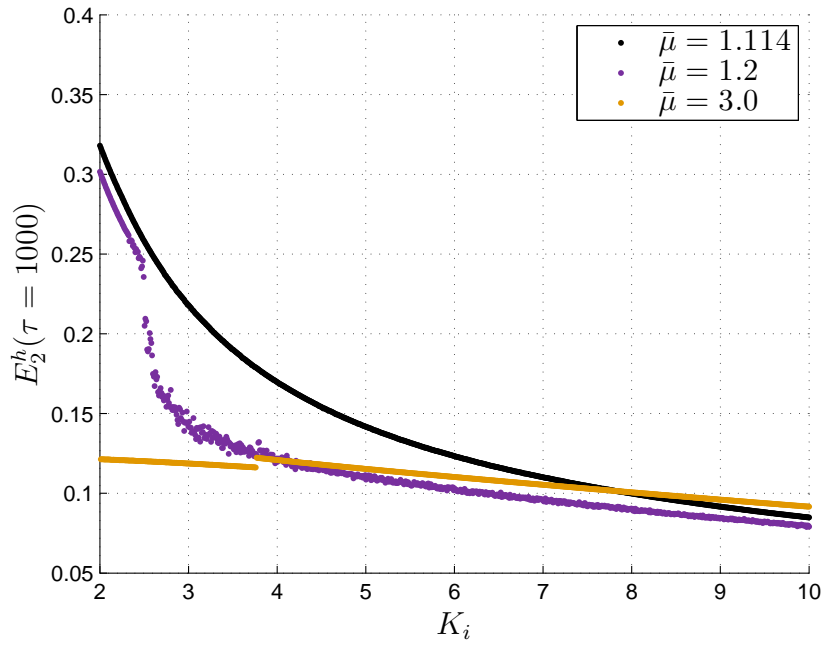
Fig. 3.16   The L_2^h error as a function of K_i for multiple values of $\bar{\mu}$.
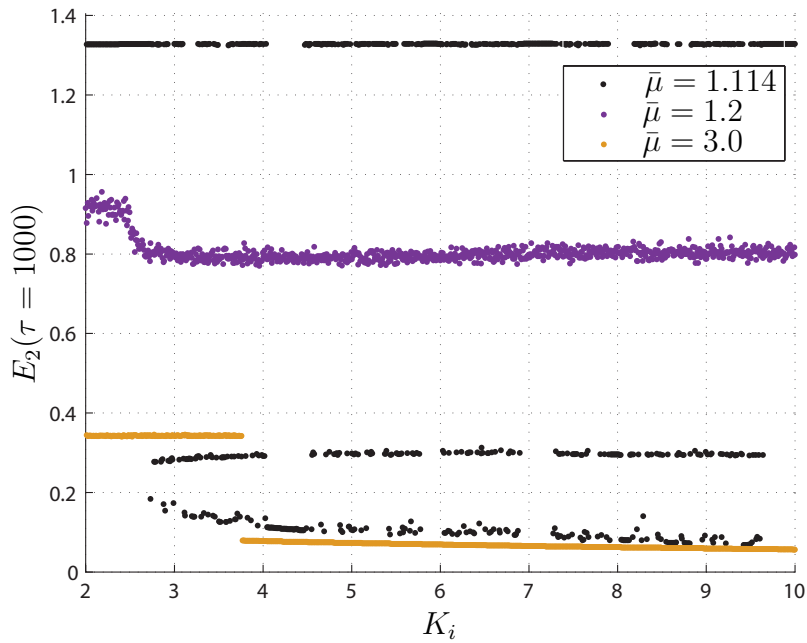
Fig. 3.17   The L_2 error as a function of K_i for multiple values of $\bar{\mu}$.
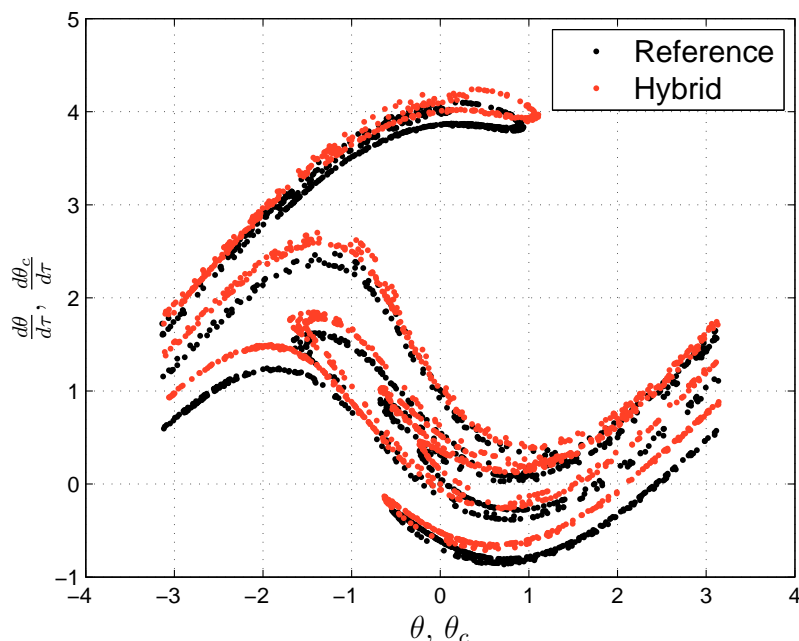
Fig. 3.18 The Poincaré sections of the reference and hybrid systems for $\bar{\mu} = 1.2$ and $K_i = 10$.

Finally, for $\bar{\mu} = 3.0$, the L^2 error sharply drops around $K_i = 4$. This occurs because the hybrid system changes from chaotic to periodic, while the reference system is periodic throughout. After the transition, the hybrid system has the same response type as the reference system. The L^2 error stays low because the hybrid system is traveling in the same direction as the reference system, and does not change direction, unlike the case of $\bar{\mu} = 1.114$. This confirms, for the most part, the conclusion about the usage of K_i reached from Fig. 3.15.

Discussion

From analyzing the reference and hybrid systems, there are three unique cases that can arise when considering the responses of the reference and hybrid systems: (1) both responses are periodic, (2) both responses are chaotic, and (3) one response is periodic while the other is chaotic.

1. For the periodic-periodic case, sometimes the hybrid system tracks the reference system well, low L^2 error, and other times it does not track the reference system well, high L^2 error. However, in the case of high L^2 error, it is noted that the two systems experience similar motions, despite not tracking well, which is shown in Fig. 3.5. This leads to a fundamental question of hybrid simulation: what does one expect to get from hybrid simulation? If one hopes to get perfect tracking with hybrid

simulation, while it is possible via adjustment of the control parameters, it is not to be expected or assumed with a *nonlinear* system, and thus hybrid simulation loses its utility if perfect tracking is the goal. If one wishes to understand the general response of the dynamical system in that the same parts of the phase space are traversed and at the same frequency, then hybrid simulation can still be useful, and the hybrid system can provide a good representation of the reference system response. Put another way, if one is content that the hybrid system experiences the same states as the true system, independent of temporal ordering, then hybrid simulation retains its utility in the nonlinear setting. While these statements do not align well with the current application of hybrid simulation in practical cases, the objective of the dissertation is to highlight potential issues with current applications.

2. This trend carries into the second case, where both systems are chaotic. In the first example – $\bar{\mu} = 1.2$ – poor time series matching was observed but there was good matching of the Poincaré sections, indicating a clear correlation in the dynamics of the two systems. And in the second example – $\bar{\mu} = 2.2$ – there was good time series matching, but little correlation between the two Poincaré sections. Thus, there is a need to compare more than one aspect of the dynamics, for example the largest Lyapunov exponents, the Lyapunov dimension, and the correlation exponent can be used to analyze the correspondence between the responses. Using Fig. 3.8, it is clear that responses are similar. Even though the time series of the reference and hybrid systems do not follow each other closely, the allowable motions for each system are closely related. Using Figs. 3.9 and 3.10, it is clear that the time series match well even though the Poincaré sections are not similar, which still indicates that responses of the reference and hybrid systems are correlated in the example. Thus, knowing the response of the hybrid system does give an approximation of how the reference system will respond. Again, as long as the exact trajectory is not needed, i.e. one is satisfied that the system moves through the correct states at the correct sampling frequency, then hybrid simulation is still useful for understanding the response of the reference system. This information linked with the numerical error metrics agrees with the conclusion made in the first case, in that one needs to be fully aware of what one wants from hybrid simulation; exact matching may not be possible, however, it is possible for hybrid simulation to properly reproduce certain dynamical quantities, which can be just as useful.

3. Finally, for the third case – one system is periodic and the other is chaotic – it is not useful to try and compare the two responses. For the periodic system, the response will approach a periodic steady-state, whereas in the chaotic system, the response will be an aperiodic solution. Thus all of the errors discussed in this chapter will indicate large differences in the behavior of the response. However, if one can make sure that both systems are behaving in the same manner, then that can be useful as well. One way to help make both systems have the same type of response is to increase the accuracy of the control scheme as seen by comparing Figs. 3.3 and 3.15.

The three cases discussed were all examined within the context with a single value of the integral gain, K_i, specifically $K_i = 3$. However, upon changing K_i one is able to understand more about the nature of the hybrid response. In all cases, the error internal to the hybrid system, $E_2^h(\tau = 1000)$, decreases as K_i is increased. Unfortunately, this does not directly translate to better tracking between the hybrid and reference systems as seen, for example, by comparing Figs. 3.16 and 3.17. In the case when both systems are periodic, it is possible, as K_i increases, for the hybrid system to change from a counter-clockwise rotation to a clockwise rotation and back. Notwithstanding, in almost all other instances, increasing K_i produces a better hybrid result. However, one can not simply increase the value of K_i to whatever one wishes, there are stability and physical constraints that determine the feasible range of K_i, thus understanding how to effectively use the control parameters is of great importance and here only one very simple control system has been examined since the underlying set of outcomes is independent of this choice and better controllers will not obviate the need to understand chaotic trajectories in the nonlinear case.

3.4 Conclusions

This chapter focused on the fundamental interface mismatch error that occurs during *nonlinear* hybrid simulation. To study this intrinsic error the behavior of a kinematically nonlinear hybrid system with a spring-mass-damper actuator system, controlled by a PI controller was examined. This is a relatively simple model, but it allowed for a lot of control over the study of the system. Most importantly, the setup was entirely theoretical and provided a true reference against which one could compare hybrid results. In particular it was found that:

1. In the nonlinear setting, hybrid simulation must account for three separate cases where the hybrid system and true system can separately take on either periodic or chaotic behavior.

2. The minimization of internal (interface) error does not necessarily mean that a hybrid system will faithfully track the true system response.

3. When good tracking does not occur, hybrid simulation can still be useful if one modifies one's objective to the notion that the hybrid system should move through the same parts of the system's state space at the same relative frequency.

4. In the case of chaotic system response, one needs to employ multiple metrics to ensure adequate accuracy.

Overall, it is concluded that the application of hybrid simulation to nonlinear systems is a delicate matter requiring an understanding of what one wishes to achieve, a knowledge of the three possible outcomes, and the application of multiple metrics to ensure fidelity.

Chapter 4

Hybrid Simulation Theory Applied to a Crane Structure

4.1 Introduction

The next model problem used in this dissertation is the station boom crane. This system has direct applications to a potential hybrid simulation experiment, in that understanding the motion of a crane structure during an earthquake can be invaluable. However, experimentally testing a full crane structure is impractical. This chapter aims to provide a framework for understanding how hybrid simulation affects the dynamical response of a given structure, even when that structure is quite complicated with many degrees of freedom. Multiple models already exist for these types of cranes [35, 38, 51], and are used as the basis for the model used in this chapter.

4.2 Crane System Setup: Equations of Motion

The Reference System

First, a model needs to be developed for the crane that will be used as a reference for which all subsequent hybrid systems will be compared. The reference system (RS) is that of a station boom crane. For the model in this chapter, the crane consists of a supporting beam structure with eight degrees of freedom given by u_1 to u_8. Connected to the crane structure is the crane cabin, which is a rigid body that can rotate about a pivot with a prescribed angel α and a flexing angle δ from the supporting structure. A flexible boom is connected to the cabin, and can pivot with respect to the cabin by some prescribed angle β and a flexing angle γ. Finally, a payload point mass is attached to the end of the boom via an extensible cable defined by a set of spherical polar coordinates, ϕ and θ and radius R. A diagram of the described crane structure can be seen in Fig. 4.1. The crane can be excited by ground motions in the 1-direction (u_{g1}) and 2-direction (u_{g2}).

48
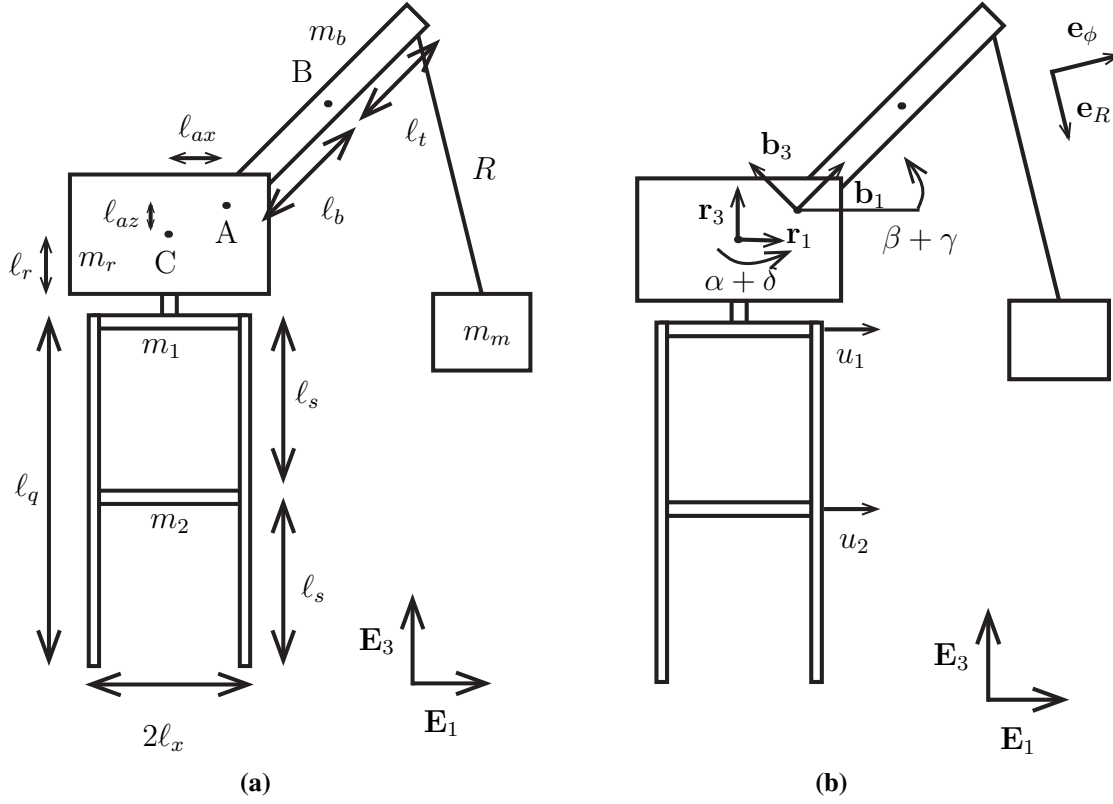
Fig. 4.1 A diagram of the Reference System (RS).

Next the equations of motion for RS need to be derived. To do this, Lagrange's prescription for the equations of motion are employed, given by Eq. (4.1) [48].

$$\frac{d}{dt}\left(\frac{\partial T}{\partial \dot{q}^i}\right) - \frac{\partial T}{\partial q^i} + \frac{\partial U}{\partial q^i} + \frac{\partial D}{\partial \dot{q}^i} = 0, \tag{4.1}$$

where

$$\begin{bmatrix} q^i \end{bmatrix} = \begin{bmatrix} R & \phi & \theta & \gamma & u_1 & u_2 & u_3 & u_4 & u_5 & u_6 & u_7 & u_8 \end{bmatrix}. \tag{4.2}$$

In this case, T is the kinetic energy, U is the potential energy, and D is the Rayleigh dissipation function (see [52]), which are given by the following:

$$T = \frac{1}{2}m_m \mathbf{v}_m \cdot \mathbf{v}_m + \frac{1}{2}m_b \mathbf{v}_b \cdot \mathbf{v}_b + \frac{1}{2}m_r \mathbf{v}_r \cdot \mathbf{v}_r \tag{4.3}$$

$$+ \frac{1}{2}\boldsymbol{\omega}_b \cdot \mathbf{J}_b \boldsymbol{\omega}_b + \frac{1}{2}\boldsymbol{\omega}_r \cdot \mathbf{J}_r \boldsymbol{\omega}_r + \frac{1}{2}\sum_{j=1}^{4} \dot{\mathbf{u}}_j^t \cdot \mathbf{M}_j \dot{\mathbf{u}}_j^t,$$

$$U = m_m g \mathbf{x}_m \cdot \mathbf{E}_3 + m_b g \mathbf{x}_b \cdot \mathbf{E}_3 + m_r g \mathbf{x}_r \cdot \mathbf{E}_3 \tag{4.4}$$

$$+ \frac{1}{2} k_m (R - R_0)^2 + \frac{1}{2} k_b \gamma^2 + \frac{1}{2} \sum_{j=1}^{4} \mathbf{u}_j \cdot \mathbf{K}_j \mathbf{u}_j,$$

$$D = \frac{1}{2} c_m \dot{R}^2 + \frac{1}{2} c_b \dot{\gamma}^2 + \frac{1}{2} \sum_{j=1}^{4} \dot{\mathbf{u}}_j \cdot \mathbf{C}_j \dot{\mathbf{u}}_j, \tag{4.5}$$

where m_m, c_m, and k_m are the mass, viscous damping constant, and stiffness of the payload and it's cable attachment, m_b, c_b, k_b, and $\mathbf{J}_b$ are the mass, viscous damping constant, stiffness, and rotational inertia matrix of the crane boom, m_r and $\mathbf{J}_r$ are the mass and rotational inertia matrix of the crane cabin, and $\mathbf{M}_j$, $\mathbf{C}_j$, and $\mathbf{K}_j$ are the *jth* mass, damping, and stiffness matrices for the crane supporting structure and are derived following the methods outlined by Chopra [10]. And $\mathbf{u}_j$ are the displacements for the supporting structure. The index j goes from 1 to 4, one for each side of the supporting structure.

First, position vectors used to describe the motion of RS are defined:

$$\mathbf{x}_g = u_{g1} \mathbf{E}_1 + u_{g2} \mathbf{E}_2, \tag{4.6}$$

which is the ground motion.

$$\mathbf{x}_s = 0.5(u_1 + u_5) \mathbf{E}_1 + 0.5(u_3 + u_7) \mathbf{E}_2 + \ell_q \mathbf{E}_3 + \mathbf{x}_g = x_s \mathbf{E}_1 + y_s \mathbf{E}_2 + \ell_q \mathbf{E}_3, \tag{4.7}$$

which is the position of the base of the crane cabin.

$$\mathbf{x}_r = \ell_r \mathbf{E}_3 + \mathbf{x}_s, \tag{4.8}$$

which is the center of mass of the crane cabin.

$$\mathbf{x}_a = \ell_{ax} \mathbf{r}_1 + \ell_{az} \mathbf{E}_3 + \mathbf{x}_r, \tag{4.9}$$

which is the position of the connection point of the boom.

$$\mathbf{x}_b = \ell_b \mathbf{b}_1 + \mathbf{x}_a, \tag{4.10}$$

which is the center of mass of the boom.

$$\mathbf{x}_t = \ell_t \mathbf{b}_1 + \mathbf{x}_b, \tag{4.11}$$

which is the position of the end of the boom.

$$\mathbf{x}_m = R \mathbf{e}_R + \mathbf{x}_t, \tag{4.12}$$

which is the position of the payload.

$$[\mathbf{u}_j] = [u_{2j-1} \ u_{2j}]^T, \tag{4.13}$$

which are the displacements of the supporting structure. Also,

$$x_s = 0.5(u_1 + u_5) + u_{g1}, \quad y_s = 0.5(u_3 + u_7) + u_{g2}, \tag{4.14}$$

$$\delta = 0.25 \left(\frac{u_1 - u_5}{l_x} + \frac{u_3 - u_7}{l_y} \right).$$

Also, the following vectors and rotation tensors are defined:

$$\mathbf{r}_i = \mathbf{R}_1 \mathbf{E}_i, \tag{4.15}$$

where $\mathbf{r}_i$ is the co-rotational basis of the crane cabin.

$$\mathbf{b}_i = \mathbf{R}_2 \mathbf{r}_i, \tag{4.16}$$

where $\mathbf{b}_i$ is the co-rotational basis of the boom.

$$\mathbf{R}_1 = \begin{bmatrix} \cos(\alpha + \delta) & -\sin(\alpha + \delta) & 0 \\ \sin(\alpha + \delta) & \cos(\alpha + \delta) & 0 \\ 0 & 0 & 1 \end{bmatrix}_{\mathbf{E}_i \otimes \mathbf{E}_j} \tag{4.17}$$

is the rotation tensor from the Cartesian basis to the $\mathbf{r}_i$ basis.

$$\mathbf{R}_2 = \begin{bmatrix} \cos(\beta + \gamma) & 0 & -\sin(\beta + \gamma) \\ 0 & 1 & 0 \\ \sin(\beta + \gamma) & 0 & \cos(\beta + \gamma) \end{bmatrix}_{\mathbf{r}_i \otimes \mathbf{r}_j} \tag{4.18}$$

is the rotation tensor from the $\mathbf{r}_i$ basis to the $\mathbf{b}_i$ basis.

$$\mathbf{e}_R = \cos(\theta)\sin(\phi)\mathbf{E}_1 + \cos(\phi)\mathbf{E}_2 - \sin(\theta)\sin(\phi)\mathbf{E}_3, \tag{4.19}$$

$$\mathbf{e}_\phi = \cos(\theta)\cos(\phi)\mathbf{E}_1 - \sin(\phi)\mathbf{E}_2 - \sin(\theta)\cos(\phi)\mathbf{E}_3, \tag{4.20}$$

and

$$\mathbf{e}_\theta = -\sin(\theta)\mathbf{E}_1 - \cos(\theta)\mathbf{E}_3, \tag{4.21}$$

define the spherical basis vectors used to define the position of the payload. Next the velocity vectors for the system are defined:

$$\mathbf{v}_g = \dot{u}_{g1}\mathbf{E}_1 + \dot{u}_{g2}\mathbf{E}_2, \tag{4.22}$$

$$\mathbf{v}_s = 0.5(\dot{u}_1 + \dot{u}_5)\mathbf{E}_1 + 0.5(\dot{u}_3 + \dot{u}_7)\mathbf{E}_2 + \mathbf{v}_g = \dot{x}_s\mathbf{E}_1 + \dot{y}_s\mathbf{E}_2, \tag{4.23}$$

$$\mathbf{v}_r = \mathbf{v}_s, \tag{4.24}$$

$$\mathbf{v}_a = \ell_{ax}(\dot{\alpha} + \dot{\delta})\mathbf{r}_2 + \mathbf{v}_r, \tag{4.25}$$

$$\mathbf{v}_b = \ell_b(\dot{\beta} + \dot{\gamma})\mathbf{b}_3 + \ell_b(\dot{\alpha} + \dot{\delta})\cos(\beta + \gamma)\mathbf{r}_2 + \mathbf{v}_a, \tag{4.26}$$

$$\mathbf{v}_t = \ell_t(\dot{\beta} + \dot{\gamma})\mathbf{b}_3 + \ell_t(\dot{\alpha} + \dot{\delta})\cos(\beta + \gamma)\mathbf{r}_2 + \mathbf{v}_b, \tag{4.27}$$

$$\mathbf{v}_m = \dot{R}\mathbf{e}_R + R\dot{\theta}\mathbf{e}_\phi + R\sin(\phi)\dot{\theta}\mathbf{e}_\theta + \mathbf{v}_t, \tag{4.28}$$

$$[\dot{\mathbf{u}}_j^t] = [\dot{u}_{2j-1} \ \dot{u}_{2j}]^T - \begin{cases} [\dot{u}_{g1} \ \dot{u}_{g1}]^T \text{ if } j \text{ is odd} \\ [\dot{u}_{g2} \ \dot{u}_{g2}]^T \text{ if } j \text{ is even,} \end{cases} \tag{4.29}$$

where Eqs. (4.22)-(4.29) are the velocities of the positions defined in Eqs. (4.6)-(4.13). Also, the angular velocities of the crane cabin and boom are

$$\boldsymbol{\omega}_r = (\dot{\alpha} + \dot{\delta})\mathbf{E}_3, \tag{4.30}$$

and

$$\boldsymbol{\omega}_b = -(\dot{\beta} + \dot{\gamma})\mathbf{r}_2 + \boldsymbol{\omega}_r, \tag{4.31}$$

respectively.

The previous equations give all of the necessary information to expand Eq. (4.1) to give the 12 equations of motion that can then be solved using a numerical integrator.

The First Hybrid System

Next, the first hybrid system (HS1) model is setup. In this case, the hybrid split is applied at the connection between the supporting structure and cabin, as can be seen in Fig. 4.2. In this case, the supporting structure is considered the computational side, or $\mathcal{C}$-side, and everything else is considered the physical side, or $\mathcal{P}$-side. By introducing this hybrid split, three new degrees of freedom are introduced: x_{sp}, y_{sp}, and δ_p which are the $\mathbf{E}_1$ position, $\mathbf{E}_2$ position, and rotation angle of the base of the crane cabin from the physical side.

Again, the equations of motion for the first hybrid system are determined by Lagrange's prescription, given by

$$\frac{d}{dt}\left(\frac{\partial \hat{T}_1}{\partial \dot{\hat{q}}_1^i}\right) - \frac{\partial \hat{T}_1}{\partial \hat{q}_1^i} + \frac{\partial \hat{U}_1}{\partial \hat{q}_1^i} + \frac{\partial \hat{D}_1}{\partial \dot{\hat{q}}_1^i} = \mathbf{F}_{1p} \cdot \frac{\partial \mathbf{v}_{sp}}{\partial \dot{\hat{q}}_1^i} + \mathbf{F}_{1c} \cdot \frac{\partial \mathbf{v}_{sc}}{\partial \dot{\hat{q}}_1^i} \tag{4.32}$$
$$+ \mathbf{M}_{1p} \cdot \frac{\partial \boldsymbol{\omega}_{rp}}{\partial \dot{\hat{q}}_1^i} + \mathbf{M}_{1c} \cdot \frac{\partial \boldsymbol{\omega}_{rc}}{\partial \dot{\hat{q}}_1^i},$$

where

$$[\hat{q}_1^i] = \begin{bmatrix} R & \phi & \theta & \gamma & x_{sp} & y_{sp} & \delta_p & u_1 & u_2 & u_3 & u_4 & u_5 & u_6 & u_7 & u_8 \end{bmatrix}. \tag{4.33}$$

Note, that a superposed hat (^) is used to denote a quantity for a hybrid system. Where $\hat{T}_1$ is the kinetic energy for the first hybrid system. And similarly, $\hat{U}_1$ is the potential energy
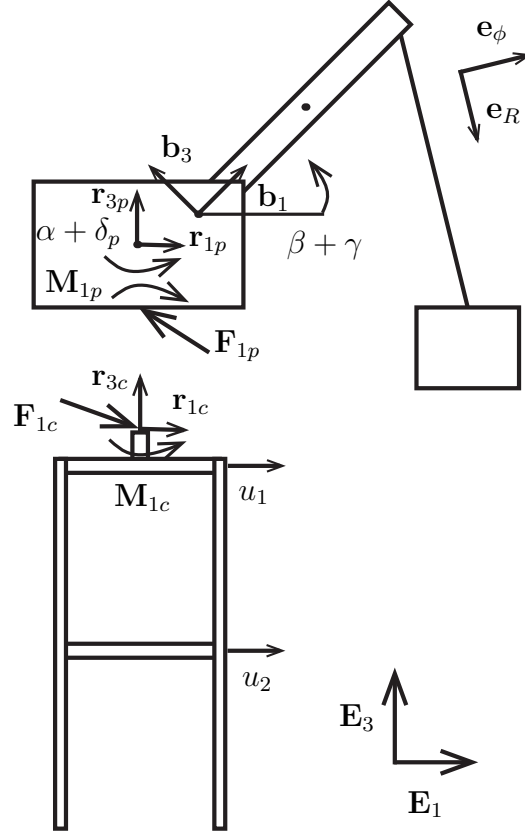
Fig. 4.2   A diagram of the First Hybrid System (HS1).

and $\hat{D}_1$ is the Rayleigh dissipation function for the first hybrid system, and are defined as follows:

$$\hat{T}_1 = \frac{1}{2}m_m\mathbf{v}_m\cdot\mathbf{v}_m + \frac{1}{2}m_b\mathbf{v}_b\cdot\mathbf{v}_b + \frac{1}{2}m_r\mathbf{v}_r\cdot\mathbf{v}_r \tag{4.34}$$
$$+ \frac{1}{2}\boldsymbol{\omega}_b\cdot\mathbf{J}_b\boldsymbol{\omega}_b + \frac{1}{2}\boldsymbol{\omega}_r\cdot\mathbf{J}_r\boldsymbol{\omega}_r + \frac{1}{2}\sum_{j=1}^{4}\dot{\mathbf{u}}_j^t\cdot\mathbf{M}_j\dot{\mathbf{u}}_j^t,$$

$$\hat{U}_1 = m_m g\mathbf{x}_m\cdot\mathbf{E}_3 + m_b g\mathbf{x}_b\cdot\mathbf{E}_3 + m_r g\mathbf{x}_r\cdot\mathbf{E}_3 \tag{4.35}$$
$$+ \frac{1}{2}k_m(R-R_0)^2 + \frac{1}{2}k_b\gamma^2 + \frac{1}{2}\sum_{j=1}^{4}\mathbf{u}_j\cdot\mathbf{K}_j\mathbf{u}_j,$$

$$\hat{D}_1 = \frac{1}{2}c_m\dot{R}^2 + \frac{1}{2}c_b\dot{\gamma}^2 + \frac{1}{2}\sum_{j=1}^{4}\dot{\mathbf{u}}_j\cdot\mathbf{C}_j\dot{\mathbf{u}}_j. \tag{4.36}$$

Note that all of the physical quantities, such as masses, stiffness, lengths, etc. are the same as those for RS. For HS1, the additional terms of $\mathbf{F}_{1p}$, $\mathbf{F}_{1c}$, $\mathbf{M}_{1p}$, and $\mathbf{M}_{1c}$ are introduced in to the equations of motion. In this case, $\mathbf{F}_{1p}$ and $\mathbf{M}_{1p}$ represent the force and moment read by sensors on the physical substructure, and $\mathbf{F}_{1c}$ and $\mathbf{M}_{1c}$ are the force and moment used as inputs to the computational model. The position vectors for HS1 are now defined:

$$\mathbf{x}_g = u_{g1}\mathbf{E}_1 + u_{g2}\mathbf{E}_2, \tag{4.37}$$

$$\mathbf{x}_{sc} = 0.5(u_1 + u_5)\mathbf{E}_1 + 0.5(u_3 + u_7)\mathbf{E}_2 + \ell_q\mathbf{E}_3 + \mathbf{x}_g = x_{sc}\mathbf{E}_1 + y_{sc}\mathbf{E}_2 + \ell_q\mathbf{E}_3, \tag{4.38}$$

$$\mathbf{x}_{sp} = x_{sp}\mathbf{E}_1 + y_{sp}\mathbf{E}_2 + \ell_q\mathbf{E}_3, \tag{4.39}$$

$$\mathbf{x}_r = \ell_r\mathbf{E}_3 + \mathbf{x}_{sp}, \tag{4.40}$$

$$\mathbf{x}_a = \ell_{ax}\mathbf{r}_{1p} + \ell_{az}\mathbf{E}_3 + \mathbf{x}_r, \tag{4.41}$$

$$\mathbf{x}_b = \ell_b\mathbf{b}_1 + \mathbf{x}_a, \tag{4.42}$$

$$\mathbf{x}_t = \ell_t\mathbf{b}_1 + \mathbf{x}_b, \tag{4.43}$$

$$\mathbf{x}_m = R\mathbf{e}_R + \mathbf{x}_t, \tag{4.44}$$

$$[\mathbf{u}_j] = [u_{2j-1}\ u_{2j}]^T, \tag{4.45}$$

where Eqs. (4.37)-(4.45) have the same physical meaning as their corresponding Eqs. (4.6)-(4.13), except that $\mathbf{x}_{sc}$ defines the position of the base of the crane cabin from the computational side and $\mathbf{x}_{sp}$ defines the position of the base of the crane cabin from the physical side. Where the following quantities are defined as:

$$x_{sc} = 0.5(u_1 + u_5) + u_{g1}, \quad y_{sc} = 0.5(u_3 + u_7) + u_{g2}, \tag{4.46}$$

$$\delta_c = 0.25\left(\frac{u_1 - u_5}{l_x} + \frac{u_3 - u_7}{l_y}\right).$$

The following vectors and rotation tensors are defined as:

$$\mathbf{r}_{ip} = \mathbf{R}_{1p}\mathbf{E}_i, \tag{4.47}$$

where $\mathbf{r}_{ip}$ is the co-rotational basis for the crane cabin, which is on the physical side.

$$\mathbf{b}_i = \mathbf{R}_2\mathbf{r}_{ip}, \tag{4.48}$$

where $\mathbf{b}_i$ is the co-rotational basis for the boom.

$$\mathbf{R}_{1p} = \begin{bmatrix} \cos(\alpha + \delta_p) & -\sin(\alpha + \delta_p) & 0 \\ \sin(\alpha + \delta_p) & \cos(\alpha + \delta_p) & 0 \\ 0 & 0 & 1 \end{bmatrix}_{\mathbf{E}_i \otimes \mathbf{E}_j} \tag{4.49}$$

is the rotation tensor from the Cartesian basis to the $\mathbf{r}_{ip}$ basis.

$$\mathbf{R}_2 = \begin{bmatrix} \cos(\beta + \gamma) & 0 & -\sin(\beta + \gamma) \\ 0 & 1 & 0 \\ \sin(\beta + \gamma) & 0 & \cos(\beta + \gamma) \end{bmatrix}_{\mathbf{r}_{ip} \otimes \mathbf{r}_{jp}} \tag{4.50}$$

is the rotation tensor from the $\mathbf{r}_{ip}$ basis to the $\mathbf{b}_i$ basis.

$$\mathbf{e}_R = \cos(\theta)\sin(\phi)\mathbf{E}_1 + \cos(\phi)\mathbf{E}_2 - \sin(\theta)\sin(\phi)\mathbf{E}_3, \tag{4.51}$$

$$\mathbf{e}_\phi = \cos(\theta)\cos(\phi)\mathbf{E}_1 - \sin(\phi)\mathbf{E}_2 - \sin(\theta)\cos(\phi)\mathbf{E}_3, \tag{4.52}$$

and

$$\mathbf{e}_\theta = -\sin(\theta)\mathbf{E}_1 - \cos(\theta)\mathbf{E}_3, \tag{4.53}$$

define the spherical basis vectors to define the position of the payload. Next the velocity vectors for HS1 are defined:

$$\mathbf{v}_g = \dot{u}_{g1}\mathbf{E}_1 + \dot{u}_{g2}\mathbf{E}_2, \tag{4.54}$$
$$\mathbf{v}_{sc} = 0.5(\dot{u}_1 + \dot{u}_5)\mathbf{E}_1 + 0.5(\dot{u}_3 + \dot{u}_7)\mathbf{E}_2 + \mathbf{v}_g = \dot{x}_{sc}\mathbf{E}_1 + \dot{y}_{sc}\mathbf{E}_2, \tag{4.55}$$
$$\mathbf{v}_{sp} = \dot{x}_{sp}\mathbf{E}_1 + \dot{y}_{sp}\mathbf{E}_2, \tag{4.56}$$
$$\mathbf{v}_r = \mathbf{v}_{sp}, \tag{4.57}$$
$$\mathbf{v}_a = \ell_{ax}(\dot{\alpha} + \dot{\delta}_p)\mathbf{r}_{2p} + \mathbf{v}_r, \tag{4.58}$$
$$\mathbf{v}_b = \ell_b(\dot{\beta} + \dot{\gamma})\mathbf{b}_3 + \ell_b(\dot{\alpha} + \dot{\delta}_p)\cos(\beta + \gamma)\mathbf{r}_{2p} + \mathbf{v}_a, \tag{4.59}$$
$$\mathbf{v}_t = \ell_t(\dot{\beta} + \dot{\gamma})\mathbf{b}_3 + \ell_t(\dot{\alpha} + \dot{\delta}_p)\cos(\beta + \gamma)\mathbf{r}_{2p} + \mathbf{v}_b, \tag{4.60}$$
$$\mathbf{v}_m = \dot{R}\mathbf{e}_R + R\dot{\theta}\mathbf{e}_\phi + R\sin(\phi)\dot{\theta}\mathbf{e}_\theta + \mathbf{v}_t, \tag{4.61}$$
$$[\dot{\mathbf{u}}_j^t] = [\dot{u}_{2j-1} \ \dot{u}_{2j}]^T - \begin{cases} [\dot{u}_{g1} \ \dot{u}_{g1}]^T \text{ if } j \text{ is odd} \\ [\dot{u}_{g2} \ \dot{u}_{g2}]^T \text{ if } j \text{ is even,} \end{cases} \tag{4.62}$$

where Eqs. (4.54)-(4.62) are the velocity vectors of the corresponding position vectors from Eqs. (4.37)-(4.45). The following angular velocity vectors are defined as:

$$\boldsymbol{\omega}_{rc} = (\dot{\alpha} + \dot{\delta}_c)\mathbf{E}_3, \tag{4.63}$$

which is the rotational velocity of the crane cabin from the computational side,

$$\boldsymbol{\omega}_{rp} = (\dot{\alpha} + \dot{\delta}_p)\mathbf{E}_3, \tag{4.64}$$

which is the rotational velocity of the crane cabin from the physical side,

$$\boldsymbol{\omega}_b = -(\dot{\beta} + \dot{\gamma})\mathbf{r}_{2p} + \boldsymbol{\omega}_{rp}, \tag{4.65}$$

which is the rotational velocity of the boom.

In the ideal setting (i.e. no sensor error), the following relations hold:

$$\mathbf{F}_{1c} \cdot \mathbf{E}_1 = -\mathbf{F}_{1p} \cdot \mathbf{E}_1, \quad \mathbf{F}_{1c} \cdot \mathbf{E}_2 = -\mathbf{F}_{1p} \cdot \mathbf{E}_2, \quad \mathbf{M}_{1c} \cdot \mathbf{E}_3 = -\mathbf{M}_{1p} \cdot \mathbf{E}_3. \tag{4.66}$$

However, at this point, there are not enough equations to fully determine the motion of HS1. In order to get the remaining equations, a model for the error at the hybrid split is required. For this chapter, the error is modeled as a spring-mass-damper system controlled by a PI controller [47]. For the error model chosen, the definition of Drazin [20] for internal boundary conditions is utilized, or

$$\underline{D}_c[\hat{\mathbf{u}}_{c1}]\Big|_{\mathcal{I}_{c1}} = \underline{D}_p[\hat{\mathbf{u}}_{p1}]\Big|_{\mathcal{I}_{p1}}. \tag{4.67}$$

In this case $\hat{\mathbf{u}}_{c1}$ and $\hat{\mathbf{u}}_{p1}$ are given by

$$[\hat{\mathbf{u}}_{c1}] = \begin{bmatrix} x_{sc} & y_{sc} & \delta_c \end{bmatrix}^T, \qquad [\hat{\mathbf{u}}_{p1}] = \begin{bmatrix} x_{sp} & y_{sp} & \delta_p \end{bmatrix}^T, \tag{4.68}$$

where the operators $\underline{D}_c[\hat{\mathbf{u}}_{c1}]$ and $\underline{D}_p[\hat{\mathbf{u}}_{p1}]$ have the following definitions:

$$\underline{D}_c[\hat{\mathbf{u}}_{c1}] = \left(k_a k_i + (k_a k_p + c_a k_i)\frac{d}{dt} + c_a k_p \frac{d^2}{dt^2} \right)\hat{\mathbf{u}}_{c1}, \tag{4.69}$$

and

$$\underline{D}_p[\hat{\mathbf{u}}_{p1}] = \left(k_a k_i + (k_a(1+k_p) + c_a k_i)\frac{d}{dt} + (c_a(1+k_p))\frac{d^2}{dt^2} + m_a\frac{d^3}{dt^3} \right)\hat{\mathbf{u}}_{p1}, \tag{4.70}$$

where the parameters m_a, c_a, and k_a are the mass, damping constant, and stiffness of the spring-mass-damper system used to model the actuator. The parameters k_p and k_i are the proportional and integral gains of the PI controller. Now there are an equal number of unknowns as there are equations, which allows one to solve the equations of motion for HS1 with the use of a numerical integrator.

The Second Hybrid System

The second hybrid system (HS2) has the hybrid split applied to the boom-cabin joint. A diagram of HS2 can be seen in Fig. 4.3. In this case, the supporting structure and cabin are considered the physical substructure, $\mathcal{P}$-side, and everything else is considered the computational model, $\mathcal{C}$-side. By introducing this hybrid split, three new degrees of freedom are created: x_{ac}, y_{ac}, and δ_c, which are the $\mathbf{E}_1$ position, the $\mathbf{E}_2$ position, and rotation angle of the connection point between the crane cabin and boom from the computational side. Lagrange's equations for HS2 are given by

$$\frac{d}{dt}\left(\frac{\partial \hat{T}_2}{\partial \dot{\hat{q}}_2^i} \right) - \frac{\partial \hat{T}_2}{\partial \hat{q}_2^i} + \frac{\partial \hat{U}_2}{\partial \hat{q}_2^i} + \frac{\partial \hat{D}_2}{\partial \dot{\hat{q}}_2^i} = \mathbf{F}_{2p} \cdot \frac{\partial \mathbf{v}_{ap}}{\partial \dot{\hat{q}}_2^i} + \mathbf{F}_{2c} \cdot \frac{\partial \mathbf{v}_{ac}}{\partial \dot{\hat{q}}_2^i} \tag{4.71}$$
$$+ \mathbf{M}_{2p} \cdot \frac{\partial \boldsymbol{\omega}_{rp}}{\partial \dot{\hat{q}}_2^i} + \mathbf{M}_{2c} \cdot \frac{\partial \boldsymbol{\omega}_{rc}}{\partial \dot{\hat{q}}_2^i},$$
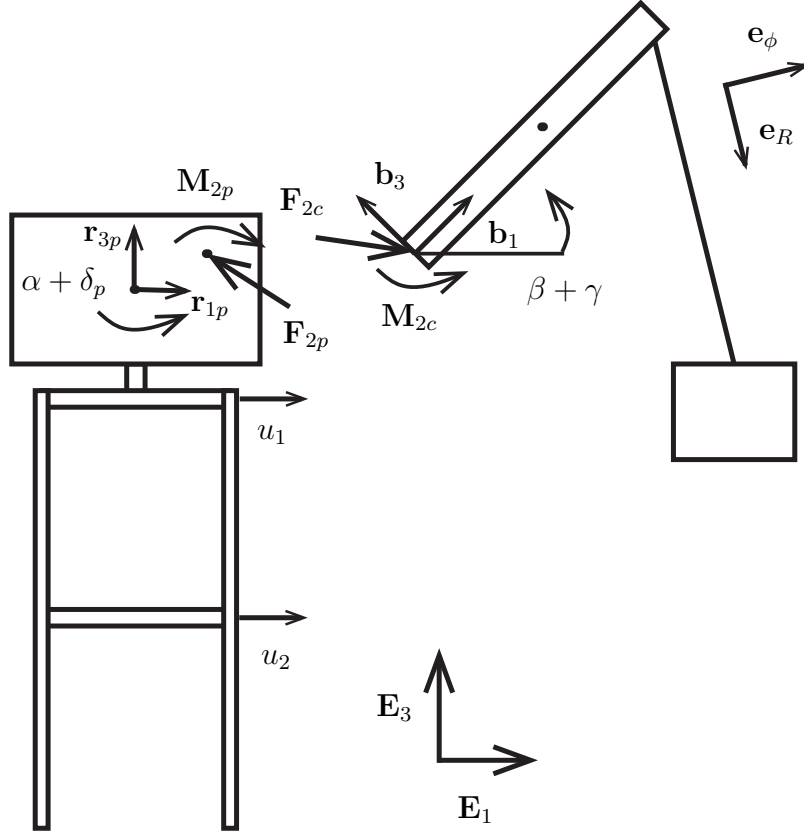
Fig. 4.3 A diagram of the Second Hybrid System (HS2).

where

$$\left[\hat{q}_2^i\right] = \begin{bmatrix} R & \phi & \theta & \gamma & x_{ac} & y_{ac} & \delta_c & u_1 & u_2 & u_3 & u_4 & u_5 & u_6 & u_7 & u_8 \end{bmatrix}. \tag{4.72}$$

The kinetic energy, $\hat{T}_2$, the potential energy, $\hat{U}_2$, and the Rayleigh dissipation function, $\hat{D}_2$, are defined as follows:

$$\hat{T}_2 = \frac{1}{2}m_m\mathbf{v}_m \cdot \mathbf{v}_m + \frac{1}{2}m_b\mathbf{v}_b \cdot \mathbf{v}_b + \frac{1}{2}m_r\mathbf{v}_r \cdot \mathbf{v}_r \tag{4.73}$$

$$+ \frac{1}{2}\boldsymbol{\omega}_b \cdot \mathbf{J}_b\boldsymbol{\omega}_b + \frac{1}{2}\boldsymbol{\omega}_r \cdot \mathbf{J}_r\boldsymbol{\omega}_r + \frac{1}{2}\sum_{j=1}^{4}\dot{\mathbf{u}}_j^t \cdot \mathbf{M}_j\dot{\mathbf{u}}_j^t,$$

$$\hat{U}_2 = m_mg\mathbf{x}_m \cdot \mathbf{E}_3 + m_bg\mathbf{x}_b \cdot \mathbf{E}_3 + m_rg\mathbf{x}_r \cdot \mathbf{E}_3 \tag{4.74}$$

$$+ \frac{1}{2}k_m(R-R_0)^2 + \frac{1}{2}k_b\gamma^2 + \frac{1}{2}\sum_{j=1}^{4}\mathbf{u}_j \cdot \mathbf{K}_j\mathbf{u}_j,$$

$$\hat{D}_2 = \frac{1}{2}c_m\dot{R}^2 + \frac{1}{2}c_b\dot{\gamma}^2 + \frac{1}{2}\sum_{j=1}^{4}\dot{\mathbf{u}}_j \cdot \mathbf{C}_j\dot{\mathbf{u}}_j. \tag{4.75}$$

57

For HS2, $\mathbf{F}_{2p}$, $\mathbf{F}_{2c}$, $\mathbf{M}_{2p}$, and $\mathbf{M}_{2c}$ are introduced into the equations of motion. In this case, $\mathbf{F}_{2p}$ and $\mathbf{M}_{2p}$ represent the force and moment read by sensors on the physical substructure, and $\mathbf{F}_{2c}$ and $\mathbf{M}_{2c}$ are the force and moment used as inputs to the computational model. The position vectors are now defined as:

$$\mathbf{x}_g = u_{g1}\mathbf{E}_1 + u_{g2}\mathbf{E}_2, \tag{4.76}$$

$$\mathbf{x}_s = 0.5(u_1 + u_5)\mathbf{E}_1 + 0.5(u_3 + u_7)\mathbf{E}_2 + \ell_q\mathbf{E}_3 + \mathbf{x}_g = x_{sp}\mathbf{E}_1 + y_{sp}\mathbf{E}_2 + \ell_q\mathbf{E}_3, \tag{4.77}$$

$$\mathbf{x}_r = \ell_r\mathbf{E}_3 + \mathbf{x}_s, \tag{4.78}$$

$$\mathbf{x}_{ap} = \ell_{ax}\mathbf{r}_{1p} + \ell_{az}\mathbf{E}_3 + \mathbf{x}_r = x_{ap}\mathbf{E}_1 + y_{ap}\mathbf{E}_2 + (\ell_q + \ell_c + \ell_{az})\mathbf{E}_3, \tag{4.79}$$

$$\mathbf{x}_{ac} = x_{ac}\mathbf{E}_1 + y_{ac}\mathbf{E}_2 + (\ell_q + \ell_c + \ell_{az})\mathbf{E}_3, \tag{4.80}$$

$$\mathbf{x}_b = \ell_b\mathbf{b}_1 + \mathbf{x}_{ac}, \tag{4.81}$$

$$\mathbf{x}_t = \ell_t\mathbf{b}_1 + \mathbf{x}_b, \tag{4.82}$$

$$\mathbf{x}_m = R\mathbf{e}_R + \mathbf{x}_t, \tag{4.83}$$

$$[\mathbf{u}_j] = [u_{2j-1} \ u_{2j}]^T, \tag{4.84}$$

where Eqs. (4.76)-(4.84) have the same physical meaning as the corresponding Eqs. (4.6)-(4.13), except that $\mathbf{x}_{ac}$ is the position of the connection point between the crane cabin and the boom from the computational side and $\mathbf{x}_{ap}$ is the position of the connection point between the crane cabin and the boom from the physical side. Where the followings quantities are defined as:

$$x_{sp} = 0.5(u_1 + u_5) + u_{g1}, \quad y_{sp} = 0.5(u_3 + u_7) + u_{g2}, \tag{4.85}$$

$$\delta_p = 0.25\left(\frac{u_1 - u_5}{l_x} + \frac{u_3 - u_7}{l_y}\right),$$

and

$$x_{ap} = x_{sp} + l_{ax}\cos(\alpha + \delta_p), \quad y_{ap} = y_{sp} + l_{ax}\sin(\alpha + \delta_p). \tag{4.86}$$

The following vectors and rotation tensors are also needed:

$$\mathbf{r}_{ip} = \mathbf{R}_{1p}\mathbf{E}_i, \tag{4.87}$$

where $\mathbf{r}_{ip}$ is the co-rotational basis of the crane cabin from the physical side.

$$\mathbf{r}_{ic} = \mathbf{R}_{1c}\mathbf{E}_i, \tag{4.88}$$

where $\mathbf{r}_{ic}$ is the co-rotational basis of the crane cabin from the computational side.

$$\mathbf{b}_i = \mathbf{R}_2\mathbf{r}_{ic}, \tag{4.89}$$

where $\mathbf{b}_i$ is the co-rotational basis of the boom.

$$\mathbf{R}_{1p} = \begin{bmatrix} \cos(\alpha + \delta_p) & -\sin(\alpha + \delta_p) & 0 \\ \sin(\alpha + \delta_p) & \cos(\alpha + \delta_p) & 0 \\ 0 & 0 & 1 \end{bmatrix}_{\mathbf{E}_i \otimes \mathbf{E}_j} \tag{4.90}$$

is the rotation tensor from the Cartesian basis to the $\mathbf{r}_{ip}$ basis.

$$\mathbf{R}_{1c} = \begin{bmatrix} \cos(\alpha + \delta_c) & -\sin(\alpha + \delta_c) & 0 \\ \sin(\alpha + \delta_c) & \cos(\alpha + \delta_c) & 0 \\ 0 & 0 & 1 \end{bmatrix}_{\mathbf{E}_i \otimes \mathbf{E}_j} \tag{4.91}$$

is the rotation tensor from the Cartesian basis to the $\mathbf{r}_{ic}$ basis.

$$\mathbf{R}_2 = \begin{bmatrix} \cos(\beta + \gamma) & 0 & -\sin(\beta + \gamma) \\ 0 & 1 & 0 \\ \sin(\beta + \gamma) & 0 & \cos(\beta + \gamma) \end{bmatrix}_{\mathbf{r}_{ic} \otimes \mathbf{r}_{jc}} \tag{4.92}$$

is the rotation tensor from the $\mathbf{r}_{ic}$ basis to the $\mathbf{b}_i$ basis.

$$\mathbf{e}_R = \cos(\theta)\sin(\phi)\mathbf{E}_1 + \cos(\phi)\mathbf{E}_2 - \sin(\theta)\sin(\phi)\mathbf{E}_3, \tag{4.93}$$

$$\mathbf{e}_\phi = \cos(\theta)\cos(\phi)\mathbf{E}_1 - \sin(\phi)\mathbf{E}_2 - \sin(\theta)\cos(\phi)\mathbf{E}_3, \tag{4.94}$$

and

$$\mathbf{e}_\theta = -\sin(\theta)\mathbf{E}_1 - \cos(\theta)\mathbf{E}_3, \tag{4.95}$$

define the spherical basis vectors to define the position of the payload. And the required velocity vectors:

$$\mathbf{v}_g = \dot{u}_{g1}\mathbf{E}_1 + \dot{u}_{g2}\mathbf{E}_2, \tag{4.96}$$

$$\mathbf{v}_{sp} = 0.5(\dot{u}_1 + \dot{u}_5)\mathbf{E}_1 + 0.5(\dot{u}_3 + \dot{u}_7)\mathbf{E}_2 + \mathbf{v}_g = \dot{x}_{sp}\mathbf{E}_1 + \dot{y}_{sp}\mathbf{E}_2, \tag{4.97}$$

$$\mathbf{v}_r = \mathbf{v}_{sp}, \tag{4.98}$$

$$\mathbf{v}_{ap} = \ell_{ax}(\dot{\alpha} + \dot{\delta}_p)\mathbf{r}_{2p} + \mathbf{v}_r, \tag{4.99}$$

$$\mathbf{v}_{ac} = \dot{x}_{ac}\mathbf{E}_1 + \dot{y}_{ac}\mathbf{E}_2, \tag{4.100}$$

$$\mathbf{v}_b = \ell_b(\dot{\beta} + \dot{\gamma})\mathbf{b}_3 + \ell_b(\dot{\alpha} + \dot{\delta}_c)\cos(\beta + \gamma)\mathbf{r}_{2c} + \mathbf{v}_{ac}, \tag{4.101}$$

$$\mathbf{v}_t = \ell_t(\dot{\beta} + \dot{\gamma})\mathbf{b}_3 + \ell_t(\dot{\alpha} + \dot{\delta}_c)\cos(\beta + \gamma)\mathbf{r}_{2c} + \mathbf{v}_b, \tag{4.102}$$

$$\mathbf{v}_m = \dot{R}\mathbf{e}_R + R\dot{\theta}\mathbf{e}_\phi + R\sin(\phi)\dot{\theta}\mathbf{e}_\theta + \mathbf{v}_t, \tag{4.103}$$

$$[\dot{\mathbf{u}}_j^t] = [\dot{u}_{2j-1} \ \dot{u}_{2j}]^T - \begin{cases} [\dot{u}_{g1} \ \dot{u}_{g1}]^T & \text{if } j \text{ is odd} \\ [\dot{u}_{g2} \ \dot{u}_{g2}]^T & \text{if } j \text{ is even,} \end{cases} \tag{4.104}$$

where Eqs. (4.96)-(4.104) are the velocities of the positions from Eqs. (4.76)-(4.84). Also, the following angular velocity vectors are defined as:

$$\boldsymbol{\omega}_{rc} = (\dot{\alpha} + \dot{\delta}_c)\mathbf{E}_3, \tag{4.105}$$

which is the angular velocity of the crane cabin from the computational side,

$$\boldsymbol{\omega}_{rp} = (\dot{\alpha} + \dot{\delta}_p)\mathbf{E}_3, \tag{4.106}$$

which is the angular velocity of the crane cabin from the physical side,

$$\boldsymbol{\omega}_b = -(\dot{\beta} + \dot{\gamma})\mathbf{r}_{2c} + \boldsymbol{\omega}_{rc}, \tag{4.107}$$

which is the angular velocity of the boom.

In the ideal setting, the following relations hold:

$$\mathbf{F}_{2c} \cdot \mathbf{E}_1 = -\mathbf{F}_{2p} \cdot \mathbf{E}_1, \quad \mathbf{F}_{2c} \cdot \mathbf{E}_2 = -\mathbf{F}_{2p} \cdot \mathbf{E}_2, \quad \mathbf{M}_{2c} \cdot \mathbf{E}_3 = -\mathbf{M}_{2p} \cdot \mathbf{E}_3. \tag{4.108}$$

Again, at this point, there are not enough equations to match the number of unknowns. To get the remaining equations, a model for the error at the split is required. Similar to HS1, the error is modeled as a spring-mass-damper system controlled by a PI controller:

$$\underline{D}_c[\hat{\mathbf{u}}_{c2}]\Big|_{\mathcal{I}_{c2}} = \underline{D}_p[\hat{\mathbf{u}}_{p2}]\Big|_{\mathcal{I}_{p2}}. \tag{4.109}$$

In this case $\hat{\mathbf{u}}_{c2}$ and $\hat{\mathbf{u}}_{p2}$ are given by

$$[\hat{\mathbf{u}}_{c2}] = \begin{bmatrix} x_{ac} & y_{ac} & \delta_c \end{bmatrix}^T, \qquad [\hat{\mathbf{u}}_{p2}] = \begin{bmatrix} x_{ap} & y_{ap} & \delta_p \end{bmatrix}^T, \tag{4.110}$$

where the operators $\underline{D}_c[\hat{\mathbf{u}}_{c2}]$ and $\underline{D}_p[\hat{\mathbf{u}}_{p2}]$ have the following definitions:

$$\underline{D}_c[\hat{\mathbf{u}}_{c2}] = \left(k_a k_i + (k_a k_p + c_a k_i)\frac{d}{dt} + c_a k_p \frac{d^2}{dt^2} \right)\hat{\mathbf{u}}_{c2}, \tag{4.111}$$

and

$$\underline{D}_p[\hat{\mathbf{u}}_{p2}] = \left(k_a k_i + (k_a(1+k_p) + c_a k_i)\frac{d}{dt} + (c_a(1+k_p))\frac{d^2}{dt^2} + m_a\frac{d^3}{dt^3} \right)\hat{\mathbf{u}}_{p2}, \tag{4.112}$$

where the parameters are the same as those for HS1. There are now a sufficient number of equations to solve for the motion of HS2.

The Third Hybrid System

For the third hybrid system (HS3), there are two hybrid splits. The first split is at the connection between the supporting structure and the cabin. The second split is at the connection between the cabin and the boom. In this case the cabin is considered the physical substructure, $\mathcal{P}$-side, and everything else is considered the computational model, $\mathcal{C}$-side. Introducing these hybrid splits introduces six new degrees of freedom: x_{sp}, y_{sp}, δ_p, x_{ac}, y_{ac}, and δ_{c2}. Where x_{sp}, y_{sp}, and δ_p are the $\mathbf{E}_1$ position, $\mathbf{E}_2$ position, and rotation angle of the base of the crane cabin from the physical side and x_{ac}, y_{ac}, and δ_{c2} are the $\mathbf{E}_1$ position, the
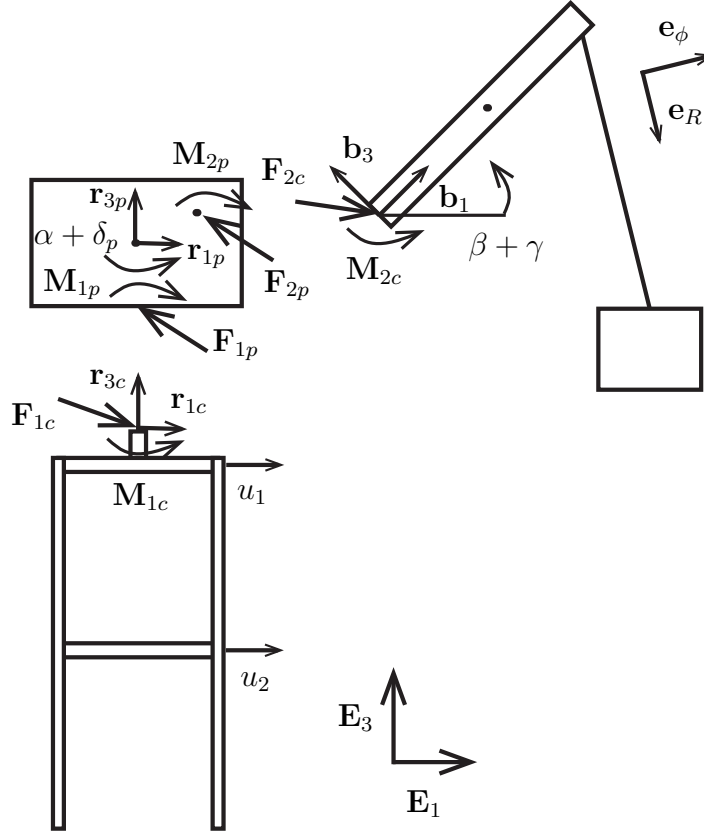
Fig. 4.4   A diagram of the Third Hybrid System (HS3).

$\mathbf{E}_2$ position, and rotation angle of the connection point between the crane cabin and boom from the computational side. A figure of HS3 is shown in Fig. 4.4, where the two hybrid splits can clearly be seen. Note that HS3 is a combination of HS1 and HS2, in that it has both of the hybrid splits from the previous two hybrid systems.

Lagrange's equation are given by the following:

$$
\frac{d}{dt}\left(\frac{\partial \hat{T}_3}{\partial \dot{\hat{q}}_3^i}\right) - \frac{\partial \hat{T}_3}{\partial \hat{q}_3^i} + \frac{\partial \hat{U}_3}{\partial \hat{q}_3^i} + \frac{\partial \hat{D}_3}{\partial \dot{\hat{q}}_3^i} = \mathbf{F}_{1p} \cdot \frac{\partial \mathbf{v}_{sp}}{\partial \dot{\hat{q}}_3^i} + \mathbf{F}_{1c} \cdot \frac{\partial \mathbf{v}_{sc}}{\partial \dot{\hat{q}}_3^i} + \mathbf{M}_{1p} \cdot \frac{\partial \boldsymbol{\omega}_{rp}}{\partial \dot{\hat{q}}_3^i} \tag{4.113}
$$

$$
+ \mathbf{M}_{1c} \cdot \frac{\partial \boldsymbol{\omega}_{rc}}{\partial \dot{\hat{q}}_3^i} + \mathbf{F}_{2p} \cdot \frac{\partial \mathbf{v}_{ap}}{\partial \dot{\hat{q}}_3^i} + \mathbf{F}_{2c} \cdot \frac{\partial \mathbf{v}_{ac}}{\partial \dot{\hat{q}}_3^i}
$$

$$
+ \mathbf{M}_{2p} \cdot \frac{\partial \boldsymbol{\omega}_{rp}}{\partial \dot{\hat{q}}_3^i} + \mathbf{M}_{2c} \cdot \frac{\partial \boldsymbol{\omega}_{rc}}{\partial \dot{\hat{q}}_3^i},
$$

where

$$
\left[\hat{q}_3^i\right] = \begin{bmatrix} R & \phi & \theta & \gamma & x_{sp} & y_{sp} & \delta_p & x_{ac} & y_{ac} & \delta_{c2} & u_1 & u_2 & u_3 & u_4 & u_5 & u_6 & u_7 & u_8 \end{bmatrix}. \tag{4.114}
$$

Similarly for the third hybrid system, the kinetic energy is denoted by $\hat{T}_3$, the potential energy is denoted by $\hat{U}_3$, and the Rayleigh dissipation function is denoted by $\hat{D}_3$, and are defined as follows:

$$\hat{U}_3 = m_m g \mathbf{x}_m \cdot \mathbf{E}_3 + m_b g \mathbf{x}_b \cdot \mathbf{E}_3 + m_r g \mathbf{x}_r \cdot \mathbf{E}_3 \tag{4.115}$$
$$+ \frac{1}{2} k_m (R - R_0)^2 + \frac{1}{2} k_b \gamma^2 + \frac{1}{2} \sum_{j=1}^{4} \mathbf{u}_j \cdot \mathbf{K}_j \mathbf{u}_j,$$

$$\hat{T}_3 = \frac{1}{2} m_m \mathbf{v}_m \cdot \mathbf{v}_m + \frac{1}{2} m_b \mathbf{v}_b \cdot \mathbf{v}_b + \frac{1}{2} m_r \mathbf{v}_r \cdot \mathbf{v}_r \tag{4.116}$$
$$+ \frac{1}{2} \boldsymbol{\omega}_b \cdot \mathbf{J}_b \boldsymbol{\omega}_b + \frac{1}{2} \boldsymbol{\omega}_r \cdot \mathbf{J}_r \boldsymbol{\omega}_r + \frac{1}{2} \sum_{j=1}^{4} \dot{\mathbf{u}}_j^t \cdot \mathbf{M}_j \dot{\mathbf{u}}_j^t,$$

$$\hat{D}_3 = \frac{1}{2} c_m \dot{R}^2 + \frac{1}{2} c_b \dot{\gamma}^2 + \frac{1}{2} \sum_{j=1}^{4} \dot{\mathbf{u}}_j \cdot \mathbf{C}_j \dot{\mathbf{u}}_j. \tag{4.117}$$

In this case, $\mathbf{F}_{1p}$, $\mathbf{F}_{1c}$, $\mathbf{M}_{1p}$, $\mathbf{M}_{1c}$, $\mathbf{F}_{2p}$, $\mathbf{F}_{2c}$, $\mathbf{M}_{2p}$, and $\mathbf{M}_{2c}$ are introduced into the equations of motion, which all follow the same definitions as those from HS1 and HS2. The position vectors are defined as:

$$\mathbf{x}_g = u_{g1} \mathbf{E}_1 + u_{g2} \mathbf{E}_2, \tag{4.118}$$
$$\mathbf{x}_{sc} = 0.5(u_1 + u_5) \mathbf{E}_1 + 0.5(u_3 + u_7) \mathbf{E}_2 + \ell_q \mathbf{E}_3 + \mathbf{x}_g = x_{sc} \mathbf{E}_1 + y_{sc} \mathbf{E}_2 + \ell_q \mathbf{E}_3, \tag{4.119}$$
$$\mathbf{x}_{sp} = x_{sp} \mathbf{E}_1 + y_{sp} \mathbf{E}_2 + \ell_q \mathbf{E}_3, \tag{4.120}$$
$$\mathbf{x}_r = \ell_r \mathbf{E}_3 + \mathbf{x}_{sp}, \tag{4.121}$$
$$\mathbf{x}_{ap} = \ell_{ax} \mathbf{r}_{1p} + \ell_{az} \mathbf{E}_3 + \mathbf{x}_r, \tag{4.122}$$
$$\mathbf{x}_{ac} = x_{ac} \mathbf{E}_1 + y_{ac} \mathbf{E}_2 + (\ell_q + \ell_c + \ell_{az}) \mathbf{E}_3, \tag{4.123}$$
$$\mathbf{x}_b = \ell_b \mathbf{b}_1 + \mathbf{x}_{ac}, \tag{4.124}$$
$$\mathbf{x}_t = \ell_t \mathbf{b}_1 + \mathbf{x}_b, \tag{4.125}$$
$$\mathbf{x}_m = R \mathbf{e}_R + \mathbf{x}_t, \tag{4.126}$$
$$[\mathbf{u}_j] = [u_{2j-1} \ u_{2j}]^T, \tag{4.127}$$

where Eqs. (4.118)-(4.127) all have the same physical meaning as their corresponding Eqs. (4.6)-(4.13), except that $\mathbf{x}_{sc}$ defines the position of the base of the crane cabin from the computational side and $\mathbf{x}_{sp}$ defines the position of the base of the crane cabin from the physical side and $\mathbf{x}_{ac}$ is the position of the connection point between the crane cabin and the boom from the computational side and $\mathbf{x}_{ap}$ is the position of the connection point between

the crane cabin and the boom from the physical side. Also, the following quantities are defined as:

$$x_{sc} = 0.5(u_1 + u_5) + u_{g1}, \quad y_{sc} = 0.5(u_3 + u_7) + u_{g2}, \tag{4.128}$$

$$\delta_c = 0.25 \left(\frac{u_1 - u_5}{l_x} + \frac{u_3 - u_7}{l_y} \right).$$

The required vectors and rotation tensors are given by:

$$\mathbf{r}_{ip} = \mathbf{R}_{1p} \mathbf{E}_i, \tag{4.129}$$

where $\mathbf{r}_{ip}$ is the co-rotational basis of the crane cabin from the physical side.

$$\mathbf{r}_{ic} = \mathbf{R}_{1c} \mathbf{E}_i, \tag{4.130}$$

where $\mathbf{r}_{ic}$ is the co-rotational basis of the crane cabin from the computational side.

$$\mathbf{b}_i = \mathbf{R}_2 \mathbf{r}_{ic}, \tag{4.131}$$

where $\mathbf{b}_i$ is the co-rotational basis of the boom.

$$\mathbf{R}_{1p} = \begin{bmatrix} \cos(\alpha + \delta_p) & -\sin(\alpha + \delta_p) & 0 \\ \sin(\alpha + \delta_p) & \cos(\alpha + \delta_p) & 0 \\ 0 & 0 & 1 \end{bmatrix}_{\mathbf{E}_i \otimes \mathbf{E}_j} \tag{4.132}$$

is the rotation tensor from the Cartesian basis to the $\mathbf{r}_{ip}$ basis.

$$\mathbf{R}_{1c} = \begin{bmatrix} \cos(\alpha + \delta_{c2}) & -\sin(\alpha + \delta_{c2}) & 0 \\ \sin(\alpha + \delta_{c2}) & \cos(\alpha + \delta_{c2}) & 0 \\ 0 & 0 & 1 \end{bmatrix}_{\mathbf{E}_i \otimes \mathbf{E}_j} \tag{4.133}$$

is the rotation tensor from the Cartesian basis to the $\mathbf{r}_{ic}$ basis.

$$\mathbf{R}_2 = \begin{bmatrix} \cos(\beta + \gamma) & 0 & -\sin(\beta + \gamma) \\ 0 & 1 & 0 \\ \sin(\beta + \gamma) & 0 & \cos(\beta + \gamma) \end{bmatrix}_{\mathbf{r}_{ic} \otimes \mathbf{r}_{jc}} \tag{4.134}$$

is the rotation tensor from the $\mathbf{r}_{ic}$ basis to the $\mathbf{b}_i$ basis.

$$\mathbf{e}_R = \cos(\theta)\sin(\phi)\mathbf{E}_1 + \cos(\phi)\mathbf{E}_2 - \sin(\theta)\sin(\phi)\mathbf{E}_3, \tag{4.135}$$

$$\mathbf{e}_\phi = \cos(\theta)\cos(\phi)\mathbf{E}_1 - \sin(\phi)\mathbf{E}_2 - \sin(\theta)\cos(\phi)\mathbf{E}_3, \tag{4.136}$$

and

$$\mathbf{e}_\theta = -\sin(\theta)\mathbf{E}_1 - \cos(\theta)\mathbf{E}_3, \tag{4.137}$$

define the spherical basis vectors to define the position of the payload. Finally, the velocity vectors are as follows:

$$\mathbf{v}_g = \dot{u}_{g1}\mathbf{E}_1 + \dot{u}_{g2}\mathbf{E}_2, \tag{4.138}$$

$$\mathbf{v}_{sc} = 0.5(\dot{u}_1 + \dot{u}_5)\mathbf{E}_1 + 0.5(\dot{u}_3 + \dot{u}_7)\mathbf{E}_2 + \mathbf{v}_g = \dot{x}_{sc}\mathbf{E}_1 + \dot{y}_{sc}\mathbf{E}_2, \tag{4.139}$$

$$\mathbf{v}_{sp} = \dot{x}_{sp}\mathbf{E}_1 + \dot{y}_{sp}\mathbf{E}_2, \tag{4.140}$$

$$\mathbf{v}_r = \mathbf{v}_{sp}, \tag{4.141}$$

$$\mathbf{v}_{ap} = \ell_{ax}(\dot{\alpha} + \dot{\delta}_p)\mathbf{r}_{2p} + \mathbf{v}_r, \tag{4.142}$$

$$\mathbf{v}_{ac} = \dot{x}_{ac}\mathbf{E}_1 + \dot{y}_{ac}\mathbf{E}_2, \tag{4.143}$$

$$\mathbf{v}_b = \ell_b(\dot{\beta} + \dot{\gamma})\mathbf{b}_3 + \ell_b(\dot{\alpha} + \dot{\delta}_{c2})\cos(\beta + \gamma)\mathbf{r}_{2c} + \mathbf{v}_{ac}, \tag{4.144}$$

$$\mathbf{v}_t = \ell_t(\dot{\beta} + \dot{\gamma})\mathbf{b}_3 + \ell_t(\dot{\alpha} + \dot{\delta}_{c2})\cos(\beta + \gamma)\mathbf{r}_{2c} + \mathbf{v}_b, \tag{4.145}$$

$$\mathbf{v}_m = \dot{R}\mathbf{e}_R + R\dot{\theta}\mathbf{e}_\phi + R\sin(\phi)\dot{\theta}\mathbf{e}_\theta + \mathbf{v}_t, \tag{4.146}$$

$$[\dot{\mathbf{u}}_j^t] = [\dot{u}_{2j-1} \ \dot{u}_{2j}]^T - \begin{cases} [\dot{u}_{g1} \ \dot{u}_{g1}]^T & \text{if } j \text{ is odd} \\ [\dot{u}_{g2} \ \dot{u}_{g2}]^T & \text{if } j \text{ is even,} \end{cases} \tag{4.147}$$

where Eqs. (4.138)-(4.147) are the velocities of the positions from Eqs. (4.118)-(4.127). Also, the following angular velocity vectors are given by:

$$\boldsymbol{\omega}_{rc} = (\dot{\alpha} + \dot{\delta}_{c2})\mathbf{E}_3, \tag{4.148}$$

which is the angular velocity of the crane cabin from the computational side,

$$\boldsymbol{\omega}_{rp} = (\dot{\alpha} + \dot{\delta}_p)\mathbf{E}_3, \tag{4.149}$$

which is the angular velocity of the crane cabin from the physical side,

$$\boldsymbol{\omega}_b = -(\dot{\beta} + \dot{\gamma})\mathbf{r}_{2c} + \boldsymbol{\omega}_{rc}, \tag{4.150}$$

which is the angular velocity of the boom.

In the ideal setting, the following relations hold:

$$\mathbf{F}_{1c} \cdot \mathbf{E}_1 = -\mathbf{F}_{1p} \cdot \mathbf{E}_1, \quad \mathbf{F}_{1c} \cdot \mathbf{E}_2 = -\mathbf{F}_{1p} \cdot \mathbf{E}_2, \quad \mathbf{M}_{1c} \cdot \mathbf{E}_3 = -\mathbf{M}_{1p} \cdot \mathbf{E}_3. \tag{4.151}$$

and

$$\mathbf{F}_{2c} \cdot \mathbf{E}_1 = -\mathbf{F}_{2p} \cdot \mathbf{E}_1, \quad \mathbf{F}_{2c} \cdot \mathbf{E}_2 = -\mathbf{F}_{2p} \cdot \mathbf{E}_2, \quad \mathbf{M}_{2c} \cdot \mathbf{E}_3 = -\mathbf{M}_{2p} \cdot \mathbf{E}_3. \tag{4.152}$$

As was the case for HS1 and HS2, there are not enough equations to properly solve for the motion of HS3. To do this, the same error model described before is utilized: a spring-mass-damper system controlled by a PI controller. The equations for which are given by

$$\left. \underline{D}_c[\hat{\mathbf{u}}_{c3}] \right|_{\mathcal{I}_{c3}} = \left. \underline{D}_p[\hat{\mathbf{u}}_{p3}] \right|_{\mathcal{I}_{p3}}. \tag{4.153}$$

In this case $\hat{\mathbf{u}}_{c3}$ and $\hat{\mathbf{u}}_{p3}$ are given by

$$[\hat{\mathbf{u}}_{c3}] = \begin{bmatrix} x_{sc} & y_{sc} & \delta_c & x_{ac} & y_{ac} & \delta_{c2} \end{bmatrix}^T, \tag{4.154}$$

$$[\hat{\mathbf{u}}_{p3}] = \begin{bmatrix} x_{sp} & y_{sp} & \delta_p & x_{ap} & y_{ap} & \delta_{p2} \end{bmatrix}^T,$$

where the operators $\underline{D}_c[\hat{\mathbf{u}}_{c3}]$ and $\underline{D}_p[\hat{\mathbf{u}}_{p3}]$ have the following definitions:

$$\underline{D}_c[\hat{\mathbf{u}}_{c3}] = \left(k_a k_i + \left(k_a k_p + c_a k_i \right) \frac{d}{dt} + c_a k_p \frac{d^2}{dt^2} \right) \hat{\mathbf{u}}_{c3}, \tag{4.155}$$

and

$$\underline{D}_p[\hat{\mathbf{u}}_{p3}] = \left(k_a k_i + \left(k_a(1 + k_p) + c_a k_i \right) \frac{d}{dt} + \left(c_a(1 + k_p) \right) \frac{d^2}{dt^2} + m_a \frac{d^3}{dt^3} \right) \hat{\mathbf{u}}_{p3}, \tag{4.156}$$

where the parameters are the same as those mentioned for HS1. The system is subject to the following constraints:

$$x_{ap} = x_{sp} + l_{ax}\cos(\alpha + \delta_p), \quad y_{ap} = y_{sp} + l_{ax}\sin(\alpha + \delta_p), \quad \delta_p = \delta_{p2}, \tag{4.157}$$

in order to maintain rigid body motion for the cabin. All of the previous equations give the necessary equations to solve for the motion of HS3.

4.3   Analysis

For the analysis of the crane structure, all of the physical dimensions defined in the previous section need to be defined, along with a set of initial conditions for time integration. See Appendix C for all of the physical data, initial conditions, and other constants. Note that all values represent non-dimensionlized values. The majority of the analysis consists of evaluating how a harmonic displacement applied at the base of the structure affects the hybrid responses of the three different hybrid systems. To accomplish this, u_{g2} is defined as

$$u_{g2} = A\cos(\Omega t), \tag{4.158}$$

where A is the amplitude of the displacement and Ω is the angular frequency of the displacement, with $A = 0.1$ and Ω varying from 0.1 to 10 with a step size of 0.05. The equations of motion for each system are integrated numerically using the Dormand-Prince method, which is a type of the Runge-Kutta ODE solver [15]. A tolerance of 10^{-7} was used when evaluating the Dormand-Prince method. This method is a standard method used to evaluate non-stiff equations with medium accuracy.

Throughout the analysis, the L^2 norm [36] is used to evaluate the error. There are three different types of L^2 errors that are used in this chapter:

1. Whole System Error: when both reference system and hybrid system have equivalent quantities to compare.

$$E_\bullet^{WS}(t) = \frac{\sqrt{\int_0^t \|\mathbf{a}_\bullet - \hat{\mathbf{a}}_\bullet\|^2}}{\sqrt{\int_0^t \|\mathbf{a}_\bullet\|^2}}, \tag{4.159}$$

where $\mathbf{a}_\bullet$ and $\hat{\mathbf{a}}_\bullet$ are the state vectors for the reference and hybrid systems respectively for some physical quantities represented by $\bullet$. And $\| \bullet \|$ is the standard 2-norm of a vector.

2. Hybrid Interface Error: when the hybrid system has equivalent quantities on the $\mathcal{C}$-side and $\mathcal{P}$-side that both need to be compared to the reference system.

$$E_\bullet^{HI}(t) = \frac{\sqrt{\int_0^t \|\mathbf{a}_\bullet - \hat{\mathbf{a}}_{c\bullet}\|^2 + \|\mathbf{a}_\bullet - \hat{\mathbf{a}}_{p\bullet}\|^2}}{\sqrt{\int_0^t \|\mathbf{a}_\bullet\|^2}}, \tag{4.160}$$

where $\mathbf{a}_\bullet$, $\hat{\mathbf{a}}_{c\bullet}$, and $\hat{\mathbf{a}}_{p\bullet}$ are state vectors of the reference, computational side, and physical side, respectively, for some quantity represented by $\bullet$.

3. Hybrid System Error: the error between equivalent quantities on the $\mathcal{C}$-side and $\mathcal{P}$-side, which is the error at the hybrid interfaces.

$$E_\bullet^{HS}(t) = \frac{\sqrt{\int_0^t \|\hat{\mathbf{a}}_{c\bullet} - \hat{\mathbf{a}}_{p\bullet}\|^2}}{\sqrt{\int_0^t \|\hat{\mathbf{a}}_{c\bullet}\|^2}}, \tag{4.161}$$

where $\hat{\mathbf{a}}_{c\bullet}$, and $\hat{\mathbf{a}}_{p\bullet}$ are state vectors of the computational side and physical side, respectively, for some quantity represented by $\bullet$. Note, this type of error is not dependent upon the reference system.

Note, that in all three cases, the error is normalized, in the first two cases, to the reference system, and for the third case, to the $\mathcal{C}$-side. Whole system errors are computed for the states of the system ($\mathbf{a}_s$, $\hat{\mathbf{a}}_s$) and the total energy of the system ($\mathbf{a}_E$, $\hat{\mathbf{a}}_E$). Hybrid interface errors and hybrid system errors are computed for δ ($\mathbf{a}_\delta$, $\hat{\mathbf{a}}_{c\delta}$, $\hat{\mathbf{a}}_{p\delta}$), x_s ($\mathbf{a}_x$, $\hat{\mathbf{a}}_{cx}$, $\hat{\mathbf{a}}_{px}$), and y_s ($\mathbf{a}_y$, $\hat{\mathbf{a}}_{cy}$, $\hat{\mathbf{a}}_{py}$). See Appendix D for definitions of all of the previously mentioned vectors. In order to let all of the L^2 errors approach a steady-state value, the L^2 errors for the following figures are all computed out to a value of $t = 1000$.

Figures 4.5-4.12 show all of the L^2 errors for the different properties mentioned earlier. From examining these figures, fairly smooth curves for the all of the L^2 errors except around $\Omega = 1.75$ and $\Omega = 5.4$ are seen. First, the analysis ignores the areas around $\Omega = 1.75$ and $\Omega = 5.4$, and analysis of the cause and impact of those two regions comes afterward.
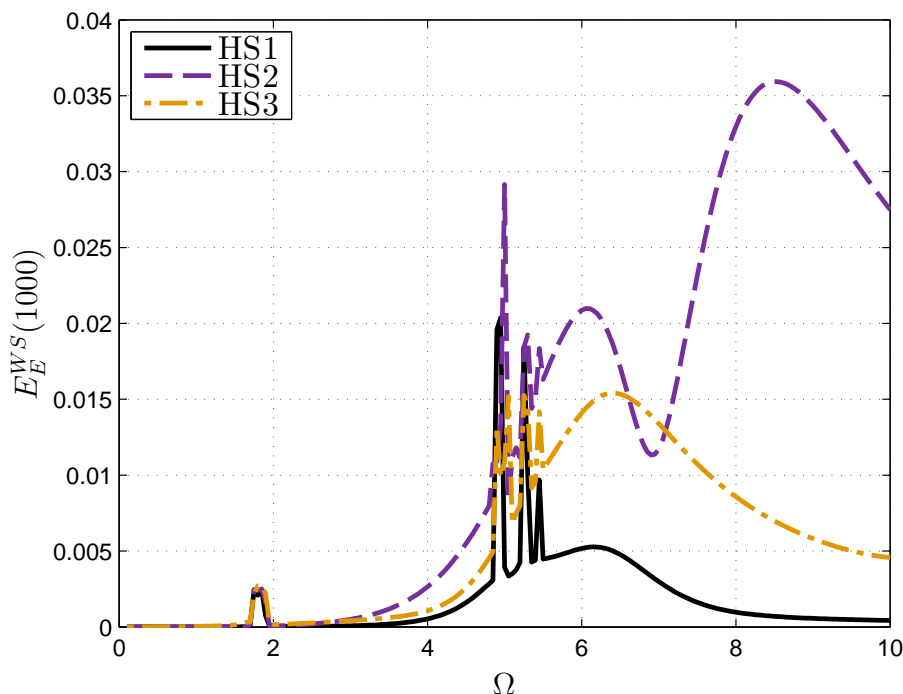
Fig. 4.5 The Whole System Error of the total energy for all three hybrid systems as a function of Ω.

Comparing the Reference System to the Hybrid Systems

While excluding the regions around $\Omega = 1.75$ and $\Omega = 5.4$, it is noticed that the errors tend to be the smallest towards $\Omega = 0$, and get larger as $\Omega = 10$. This makes sense because, as the frequency is increased, it is harder for the controller to maintain dynamic matching between both the $\mathcal{C}$-side and $\mathcal{P}$-side, which leads to larger errors. This effect is clearly shown in Figs. 4.10 and 4.11, which shows that the error between equivalent quantities on the $\mathcal{C}$-side and $\mathcal{P}$-side are approximately growing with Ω. It is noted that in some cases the L^2 error goes above 1, which is over 100% error, for example HS2 in Fig. 4.6, which indicates poor matching between the reference and hybrid systems. However, by examining Fig. 4.5, it can be seen that – even for higher frequencies – the error for HS2 never goes above 0.04, or 4%. This is interesting in that the states are not matching very well between the two systems, however, the total energy of the two systems is matching fairly well. This result is similar to one found by Drazin and Govindjee [18], indicating that different aspects of hybrid simulation can be accurate, while others can be inaccurate. This leads to a question of what is desired from hybrid simulation, and what can one reasonable expect from a hybrid simulation response. From comparing Figs. 4.5 and 4.6, it can be seen that the errors for all three systems are typically much smaller for E_E^{WS} than for E_s^{WS}. Since the E_s^{WS} represents how well the entire motion of the hybrid system matches that of
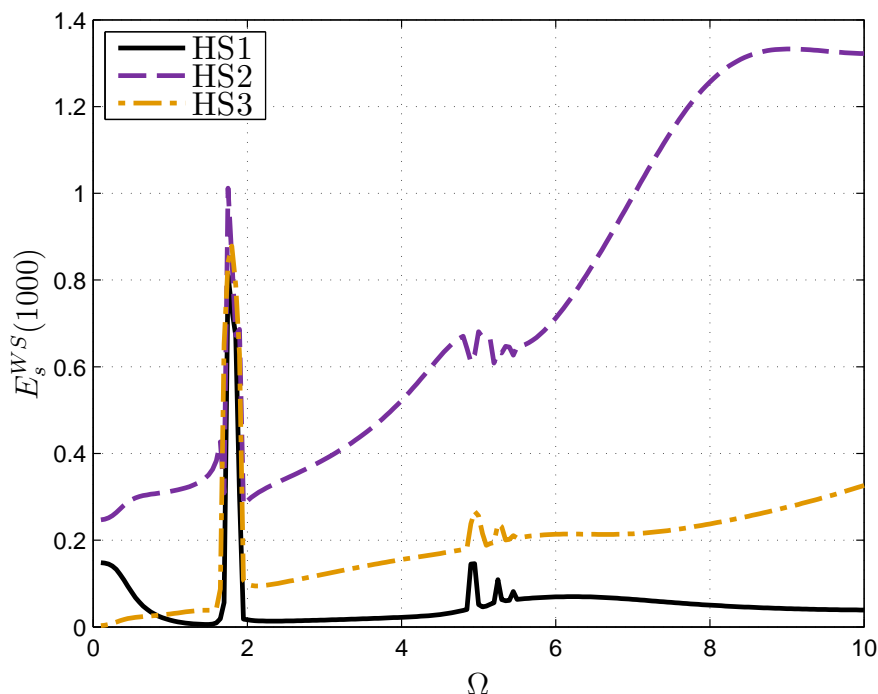
Fig. 4.6   The Whole System Error of the states for all three hybrid systems as a function of Ω.

the reference system, it is clear that the total energy of the system matches better than the actual motion of the system. Thus, even though it may seem like the hybrid simulation is not representative of the true dynamics – especially for the case of HS2 when E_s^{WS} goes above 1 – it can still provide accurate results for other physical properties of the system, in this case the total energy. This reinforces the conclusion that to fully utilize hybrid simulation, sometimes it is beneficial to look at as many physical quantities as possible, because the actual motion may not be as accurate as one would like to believe.

Comparing the Hybrid Systems to Each Other

From examining Figs. 4.5-4.12, it is clear that HS1, HS2, and HS3 all have unique error responses for all of the properties shown. This indicates that the location of the hybrid split affects the results produced from a hybrid simulation. For example, all of the L^2 errors for HS1 never goes above 0.4, whereas HS3 typically has a larger L^2 error than HS1, yet never goes above 0.7, and HS2 typically has the largest error, and in many cases goes above 1. From these results it seems that, on average, HS1 provides the best results, followed by HS3, and HS2 is the worst. This may be somewhat surprising, in that HS3 has two hybrid splits, whereas HS2 only has one, and one might expect that having only one hybrid split would imply that there is less chance for error to be introduced into the system. However,
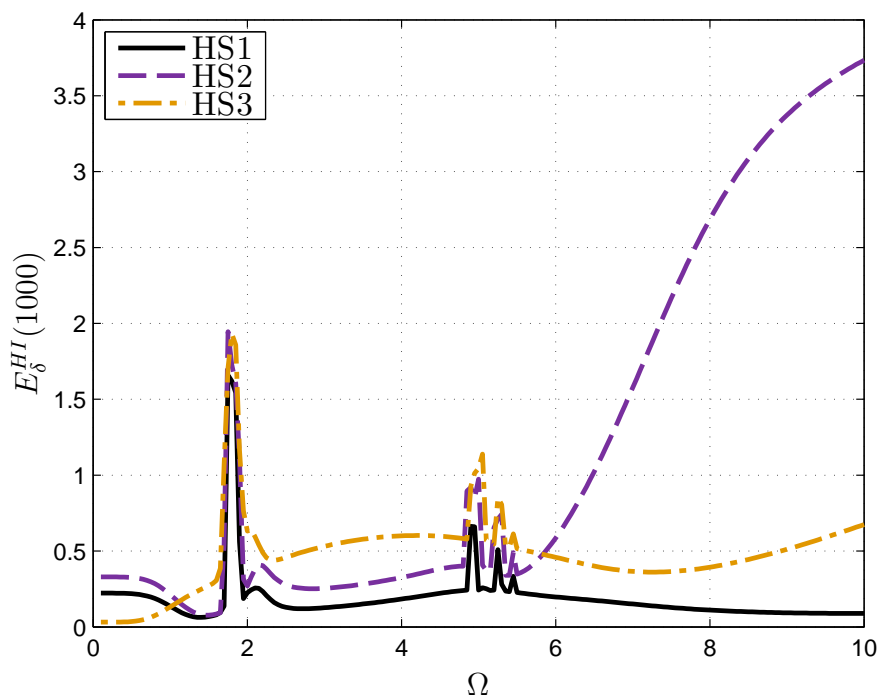
Fig. 4.7   The Hybrid Interface Error of δ for all three hybrid systems as a function of Ω.

the results show that more hybrid splits does not directly correlate to more error in the hybrid system. This implies that there are *good* and *bad* locations to create a hybrid split, where a *good* hybrid split location will be one that minimizes error introduced into the hybrid system, and a *bad* hybrid split location is one that will cause the error in the system to rise quickly. For instance, HS1 is the best hybrid system since it has the least amount of error in all three of the error metrics. This indicates that it has a *good* hybrid split location, or a hybrid split location that does not alter the system dynamics a great deal. Similarly, HS2 is the worst hybrid system, since it has the most error in all three of the error metrics. This indicates that it has a *bad* hybrid split location, or a split location that drastically changes the system dynamics. Since HS3 has the both split locations (the ones used by HS1 and HS2), it indicates that HS3 should have both a *good* and *bad* hybrid split location. Since HS3 is in between HS1 and HS2, when it comes to L^2 errors, it might indicate that *good* and *bad* locations have an averaging effect.

Analyzing the Frequency Response

From Figs. 4.5-4.12, there are fairly smooth curves for all of the L^2 errors except around $\Omega = 1.75$ and $\Omega = 5.4$, which have what seem to be random spikes in the error. To try to better understand the error spikes, the frequency response of the unforced system ($u_{g2} = 0$)
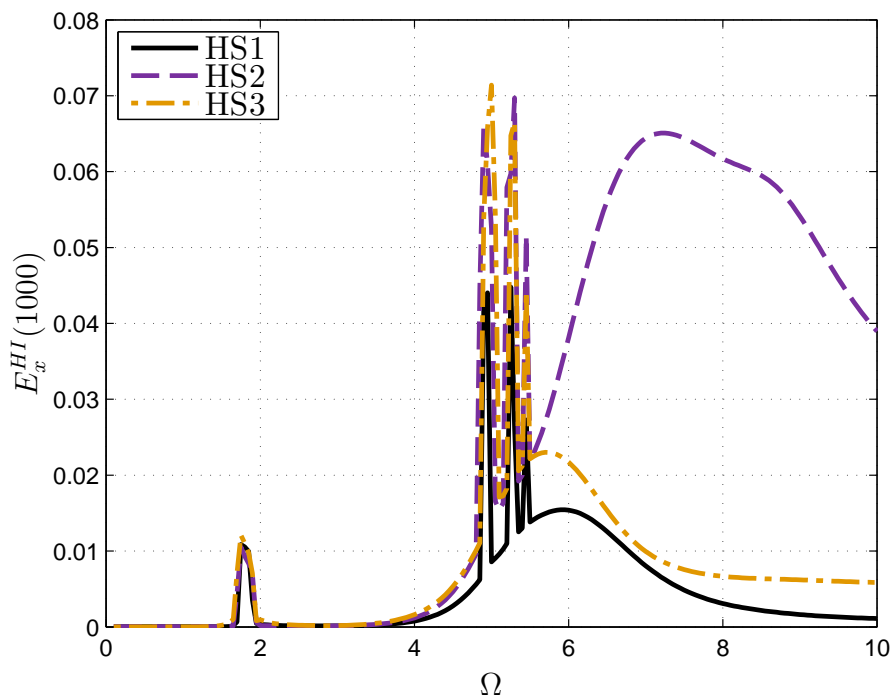
Fig. 4.8 The Hybrid Interface Error of x_s for all three hybrid systems as a function of Ω.

is analyzed. The frequency responses for all four systems are shown in Fig. 4.13, where it can be seen that there are frequency peaks around $\Omega = 1.75$ and $\Omega = 5.4$. This indicates that resonant frequencies of the system are causing the spikes in the L^2 error curves. These error spikes are similar to the error spikes found by Drazin et. al. [20] and Bakhaty et. al. [4], which were typically located near resonant frequencies of the system. Due to the appearance of error spikes in simple linear systems with constant error, as well as in this chapter with a nonlinear multi-degree of freedom system with basic PI controller, it seems to imply that error spikes near resonant frequencies are a fundamental aspect of hybrid simulation. This makes it clear that hybrid simulation has a hard time dealing with the resonant frequencies of a system, and one should be aware of this and try to avoid exciting the resonant frequencies when administering a hybrid simulation experiment in order to avoid any unnecessary error. However, it worth noting that all four systems have nearly identical frequency responses, as seen in Fig. 4.13, which indicates that the hybrid split did not change the frequency response of the system, and leaves the resonant frequencies intact. This can be an invaluable resource, in that, one can use the hybrid system to determine the resonant frequencies without actually having the reference system.
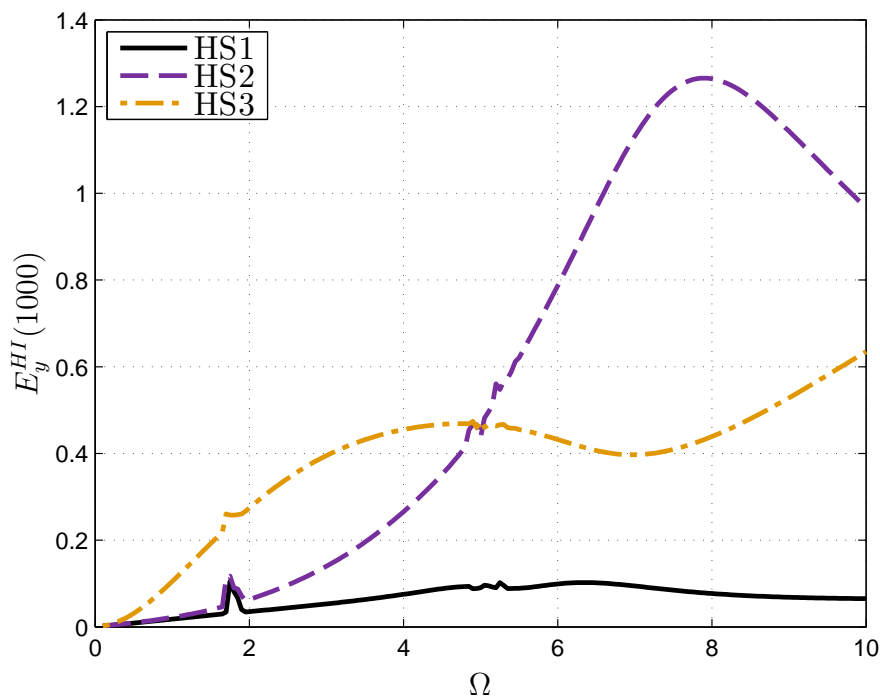
Fig. 4.9   The Hybrid Interface Error of y_s for all three hybrid systems as a function of Ω.

Discussion

In the previous section, different aspects of a theoretical hybrid simulation setup were analyzed. While there were situations in which the results of a hybrid test were comparable to that of the reference test, there were numerous occasions in which the hybrid results did not match the reference system. This indicates that the use of hybrid simulation to effectively test different mechanical systems and structures is not guaranteed, but rather requires careful consideration of how the hybrid system is constructed. As has been seen, it is possible for something as simple as the location of the hybrid split to drastically change the outcome of a hybrid test. It has also been seen that certain physical properties match fairly well while other properties do not match at all. However, all of this was determined with knowledge of the reference system. In an actual hybrid experiment, the reference system response most likely will not be known, which would make it impossible to calculate errors similar to those in this chapter. For this reason, a hybrid experiment needs to be well thought out beforehand to make sure that all error inducing situations are reduced as much as possible. In addition, a hybrid test should look at as many physical quantities as possible, such as displacements, velocities, energies, frequencies, etc., because this will give the user a greater chance at receiving useful and accurate data. If possible, it seems advisable to conduct as many hybrid tests as possible for a single mechanical system. By
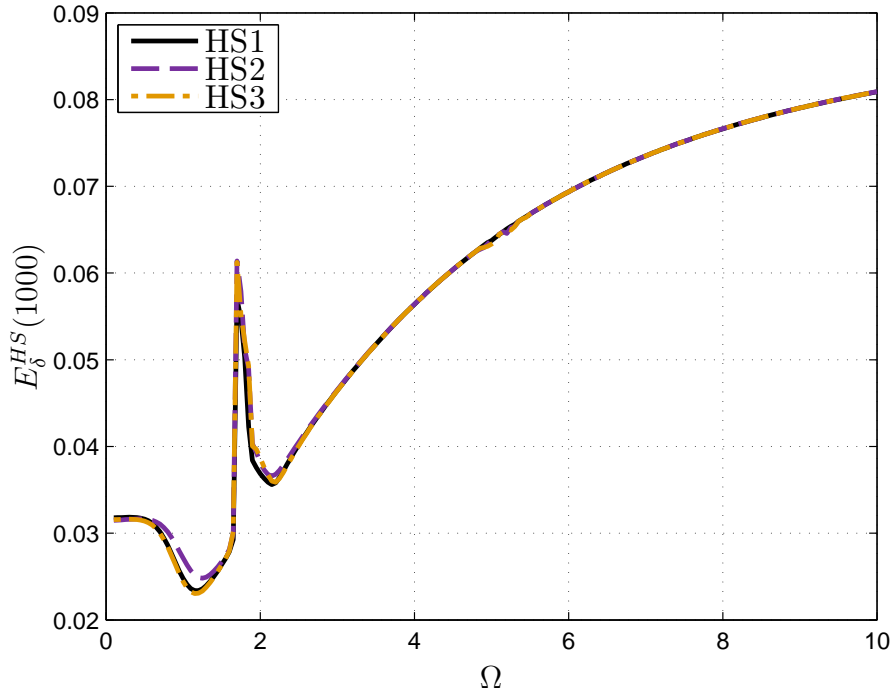
Fig. 4.10   The Hybrid System Error of δ for all three hybrid systems as a function of Ω.

doing this, there will then be multiple sets of data that can be compared to see if there is any correlation between the sets of data, which would potentially point in the direction of the reference response. Finally, with more data from multiple hybrid tests, it will provide possible ranges of motion that the mechanical system will experience; in essence creating bounds on the motion that will be useful for designing systems or structures that utilize the core component of original hybrid test.

4.4   Conclusions

This chapter aimed to expand upon the theoretical knowledge of hybrid simulation. It utilized a best case scenario for errors that might occur in a hybrid simulation experiment, namely systematic magnitude and phase mismatch at the hybrid interface through the application of a PI controller. While this is by no means a comprehensive list of all possible errors that might occur, it gives a good starting point. This chapter tested a multi-degree of freedom, nonlinear, crane structure with a theoretical hybrid simulation setup developed previously [4, 18, 20]. From this setup, three different hybrid systems were created: one with the split between the cabin and supporting structure, one with the split between the cabin and the boom, and one with both hybrid splits. The hybrid systems can be compared

72
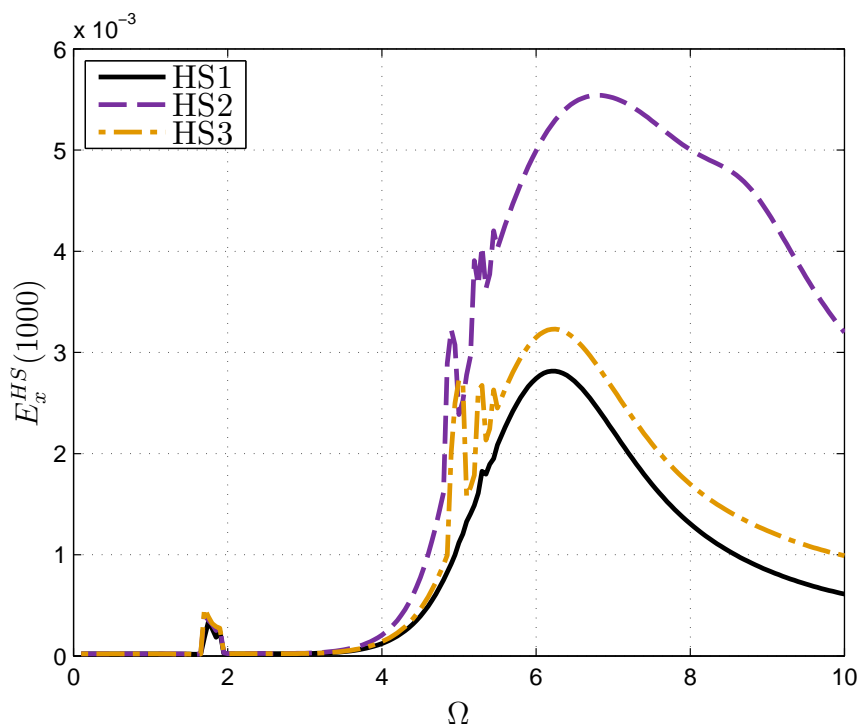
Fig. 4.11 The Hybrid System Error of x_s for all three hybrid systems as a function of Ω.

to the reference system as well as to each other in order to determine the effectiveness of each of the hybrid systems. In previous chapters, it was found that hybrid simulation can produce accurate results, but those were done with very simple linear or single degree of freedom nonlinear systems. This chapter explored the effects of how hybrid simulation scales with the size and complexity of the structure. While analyzing the hybrid systems, many correlations to previous chapters were found, such as the error spikes in the frequency domains [4, 20], as well as the fact that certain dynamical properties can be accurately described by a hybrid test while others can not [18]. This shows that the results and analysis from even the simple systems maintains its relevancy, even for more complicated structures. From comparing the hybrid systems to each other, it was found that the location of the hybrid splits, as well as how many hybrid splits there are, can have a significant impact on the overall results. This makes it critical that one fully understands the situation in which they are conducting a hybrid test. Thus, overall it can be seen that hybrid simulation can be quite effective if used properly and if proper care is taken when setting up the actual hybrid test.
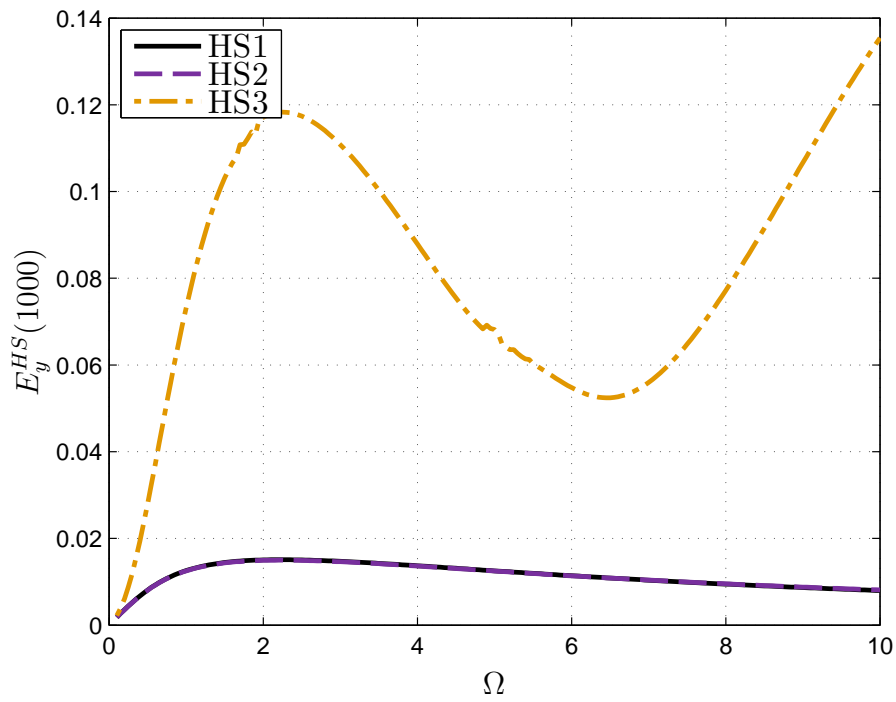
Fig. 4.12 The Hybrid System Error of y_s for all three hybrid systems as a function of Ω.
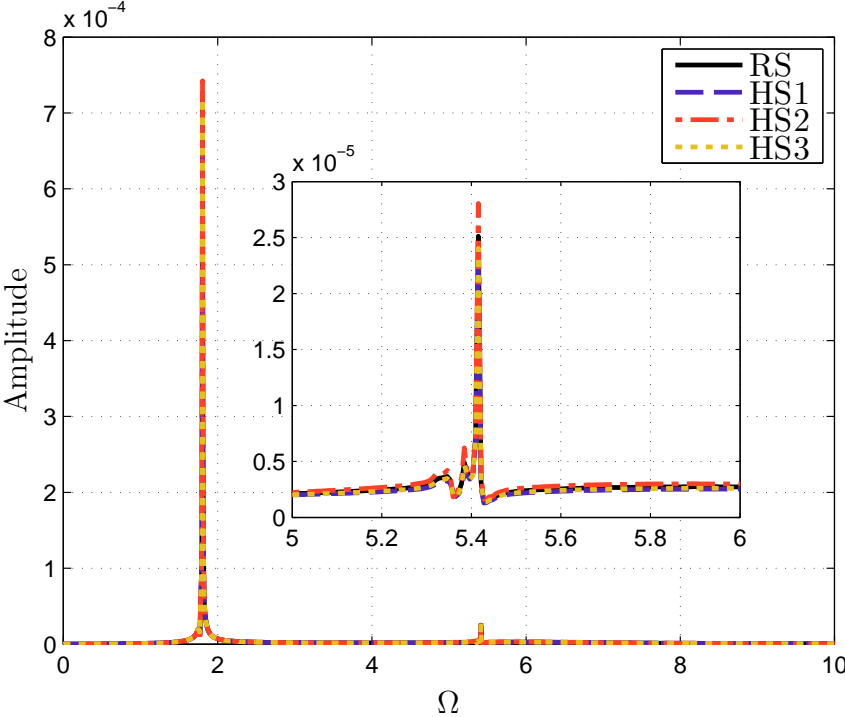
Fig. 4.13 Frequency response of the unforced system. The insert is a zoomed-in section around the peak near $\Omega = 5.4$.

Chapter 5

A Nonlinear Kinetic Model for Multi-Stage Friction Pendulum Systems

5.1 Introduction

This chapter aims to expand upon the current models for Multi-Stage Friction Pendulum systems (MSFPs), which will incorporate the full kinetics, with no linearization assumptions and no restrictions on the overall motion. A rigorous use of vectors to describe the kinematics of the internal sliders will help to clarify the overall motion of MSFPs. This will also aid in the setup of the kinetics of the MSFPs, as well as facilitating the modeling of multi-directional motion. The model to be developed will incorporate full vectorially-described motion with trajectories constrained to the configuration manifold as defined by mathematically precise constraints. Constructing the model in this way directly facilitates a number of modeling advances and naturally leads to robust numerical approximations. The advantages of the model will be (1) it will be a geometrically fully nonlinear model; (2) it will be able to naturally handle multi-directional motions, including complex rotary motions on the sliding surfaces, top and bottom plate rotations, etc.; (3) by construction, it will be fully dynamic and allow for rate dependent analysis; and (4) it will be modular and permit the use of advanced friction models. This chapter will apply the vectorized motion to that of the triple friction pendulum system, a type of MSFP, as a benchmark for the new model, but will be done in such a way that allows for easy expansion to other, more complicated MSFP systems.

5.2 Triple Friction Pendulum: Equations of Motion

First, the equations of motion for the TFP are defined, as this will allow one to see patterns in the equations so that they can be easily expanded to more complicated MSFPs. Figure 5.1 shows a cross-sectional view of the TFP used in this chapter.
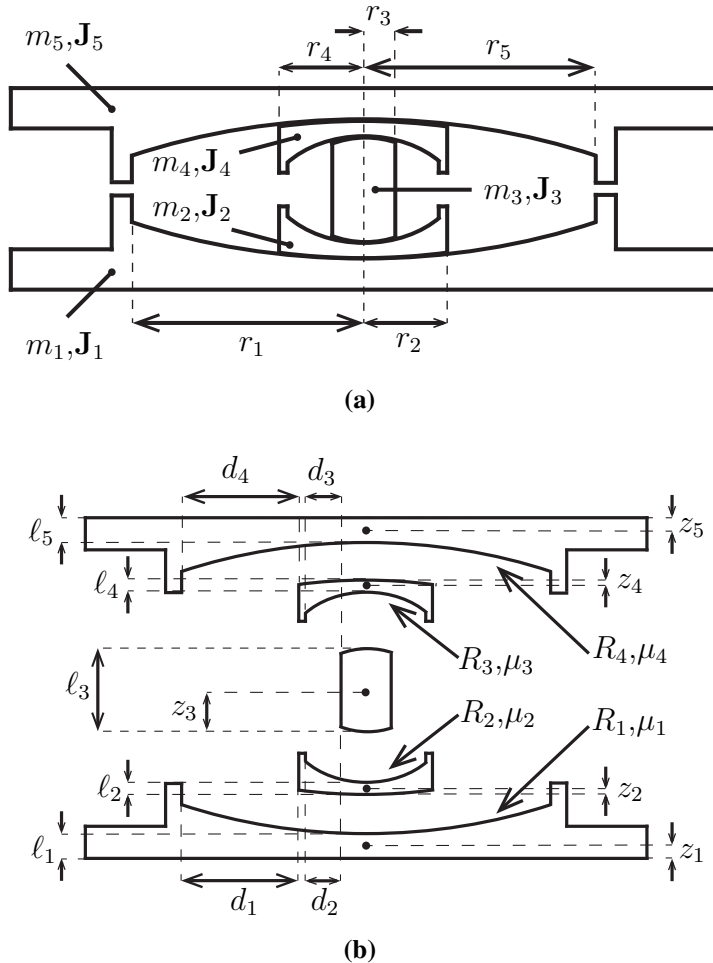
Fig. 5.1 (a) Diagram of a Triple Friction Pendulum (TFP) model. (b) Expanded
view of the TFP.

Kinematics

In order to define the equations of motion, the position vectors of all of the important
locations in the TFP need to be defined, such as center of mass of each bearing. Each
bearing will have its own set of co-rotational basis vectors defined using sets of 1-2-3
Euler angles [48], all relative to the previous bearing. It is worth noting that the Euler
angle singularity for the 1-2-3 set occurs when the second rotation angle – in this chapter
defined as θ_α – is equal to $\pm\frac{\pi}{2}$ [48]. In order to avoid this singularity, θ_α is restricted to
$\theta_\alpha \in \left(-\frac{\pi}{2}, \frac{\pi}{2}\right)$, which is well within the operating regime of MSFPs. By taking advantage of
the axial symmetry of the bearings, only the 1-2 Euler angles are needed to define the basis
vectors. Figure 5.2 shows graphically how the basis vectors are constructed from 1-2-3

Euler angles for the first set of Euler angles. The co-rotational basis are defined as:

$$\mathbf{t}_i^1 = \mathbf{R}_1 \mathbf{E}_i, \quad \mathbf{t}_i^2 = \mathbf{R}_2 \mathbf{t}_i^1, \quad \mathbf{t}_i^3 = \mathbf{R}_3 \mathbf{t}_i^2, \quad \mathbf{t}_i^4 = \mathbf{R}_4 \mathbf{t}_i^3, \quad \mathbf{t}_i^5 = \mathbf{R}_5 \mathbf{t}_i^4, \tag{5.1}$$

with the following rotation tensors:

$$\mathbf{R}_1 = \mathbf{R}(\psi_1, \theta_1; \mathbf{E}_i), \quad \mathbf{R}_2 = \mathbf{R}(\psi_2, \theta_2; \mathbf{t}_i^1), \quad \mathbf{R}_3 = \mathbf{R}(\psi_3, \theta_3; \mathbf{t}_i^2), \tag{5.2}$$
$$\mathbf{R}_4 = \mathbf{R}(\psi_4, \theta_4; \mathbf{t}_i^3), \quad \mathbf{R}_5 = \mathbf{R}(\psi_5, \theta_5; \mathbf{t}_i^4).$$

Each rotation tensor can be broken down into a series of two rotations as follows:

$$\mathbf{R}(\psi_1, \theta_1; \mathbf{E}_i) = \mathbf{L}_2(\theta_1; \mathbf{t}_i^{1'}) \mathbf{L}_1(\psi_1; \mathbf{E}_i), \tag{5.3}$$

where the individual rotations have the following definitions:

$$\mathbf{L}_1(\psi_1; \mathbf{E}_i) = \cos(\psi_1)(\mathbf{E}_2 \otimes \mathbf{E}_2 + \mathbf{E}_3 \otimes \mathbf{E}_3) \tag{5.4}$$
$$+ \sin(\psi_1)(\mathbf{E}_3 \otimes \mathbf{E}_2 - \mathbf{E}_2 \otimes \mathbf{E}_3) + \mathbf{E}_1 \otimes \mathbf{E}_1,$$

and

$$\mathbf{L}_2(\theta_1; \mathbf{t}_i^{1'}) = \cos(\theta_1)(\mathbf{t}_3^{1'} \otimes \mathbf{t}_3^{1'} + \mathbf{t}_1^{1'} \otimes \mathbf{t}_1^{1'}) \tag{5.5}$$
$$+ \sin(\theta_1)(\mathbf{t}_1^{1'} \otimes \mathbf{t}_3^{1'} - \mathbf{t}_3^{1'} \otimes \mathbf{t}_1^{1'}) + \mathbf{t}_2^{1'} \otimes \mathbf{t}_2^{1'},$$

where the intermediate co-rotational basis, $\mathbf{t}_i^{1'}$, is defined as

$$\mathbf{t}_i^{1'} = \mathbf{L}_1(\psi_1; \mathbf{E}_i) \mathbf{E}_i. \tag{5.6}$$

The co-rotational basis, $\mathbf{t}_i^{\alpha}$, is applied to the center of mass of the α bearing, an example for bearings 1 and 2 can be seen in Fig. 5.3.
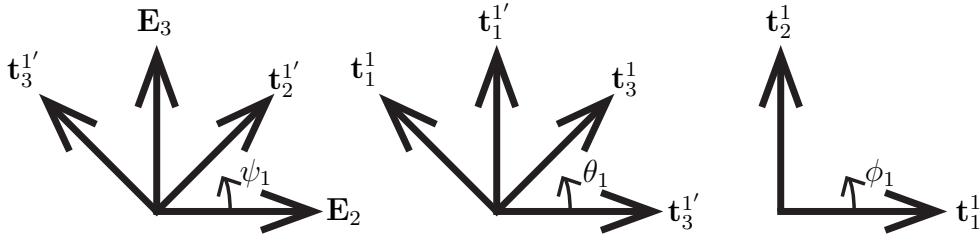
Fig. 5.2 The 2-D change of coordinates from the 1-2-3 Euler angles. Note that in each 2-D coordinate system shown, there is a third unit vector pointing out of the page following the right-hand rule about which the 2-D coordinate system is rotating.

The position vectors will all be defined relative to the previous bearing using these co-rotational bases, starting from the ground contact point with the bottom bearing, defined as
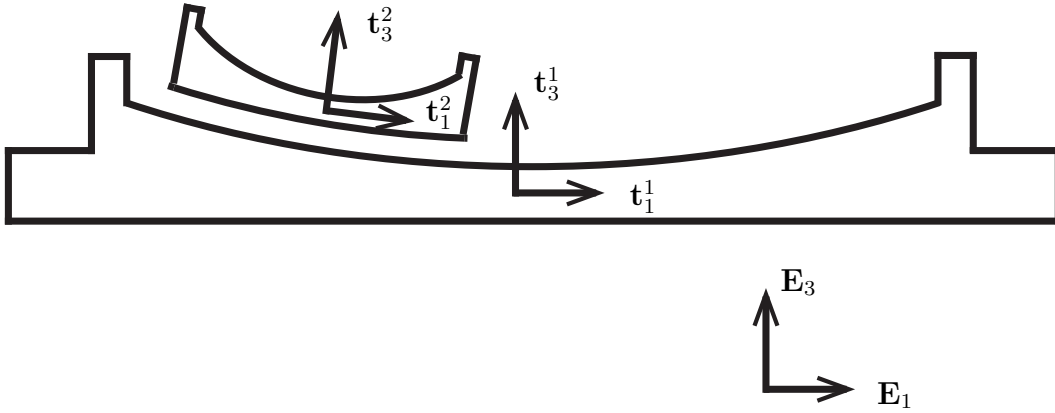
Fig. 5.3 Locations of the co-rotational basis vectors for the first two bearings. Note that for each coordinate system shown, there is a third vector pointing into the page following the right-hand rule.

$\mathbf{r}_{01}$, going all the way to the top of the final bearing, defined as $\mathbf{r}_{55}$. Figures 5.1 and 5.4 show what all of the physical quantities represent, as well as the physical locations of some of the required position vectors.

All of the required position vectors are defined as follows:

$$\mathbf{r}_{01} = u_{g1}\mathbf{E}_1 + u_{g2}\mathbf{E}_2 + u_{g3}\mathbf{E}_3, \tag{5.7}$$

which is the ground contact point of bearing one,

$$\mathbf{r}_1 = \mathbf{r}_{01} + z_1\mathbf{t}_3^1, \tag{5.8}$$

which is the center of mass of bearing one,

$$\mathbf{r}_{11} = \mathbf{r}_1 + (\ell_1 - z_1)\mathbf{t}_3^1, \tag{5.9}$$

which is the center top of bearing one,

$$\mathbf{r}_{1c} = \mathbf{r}_{11} + R_1\mathbf{t}_3^1, \tag{5.10}$$

which is the center of the sphere created by the sliding surface with radius R_1,

$$\mathbf{r}_{12} = \mathbf{r}_{1c} - R_1\mathbf{t}_3^2, \tag{5.11}$$

which is the center bottom of bearing two,

$$\mathbf{r}_2 = \mathbf{r}_{12} + z_2\mathbf{t}_3^2, \tag{5.12}$$
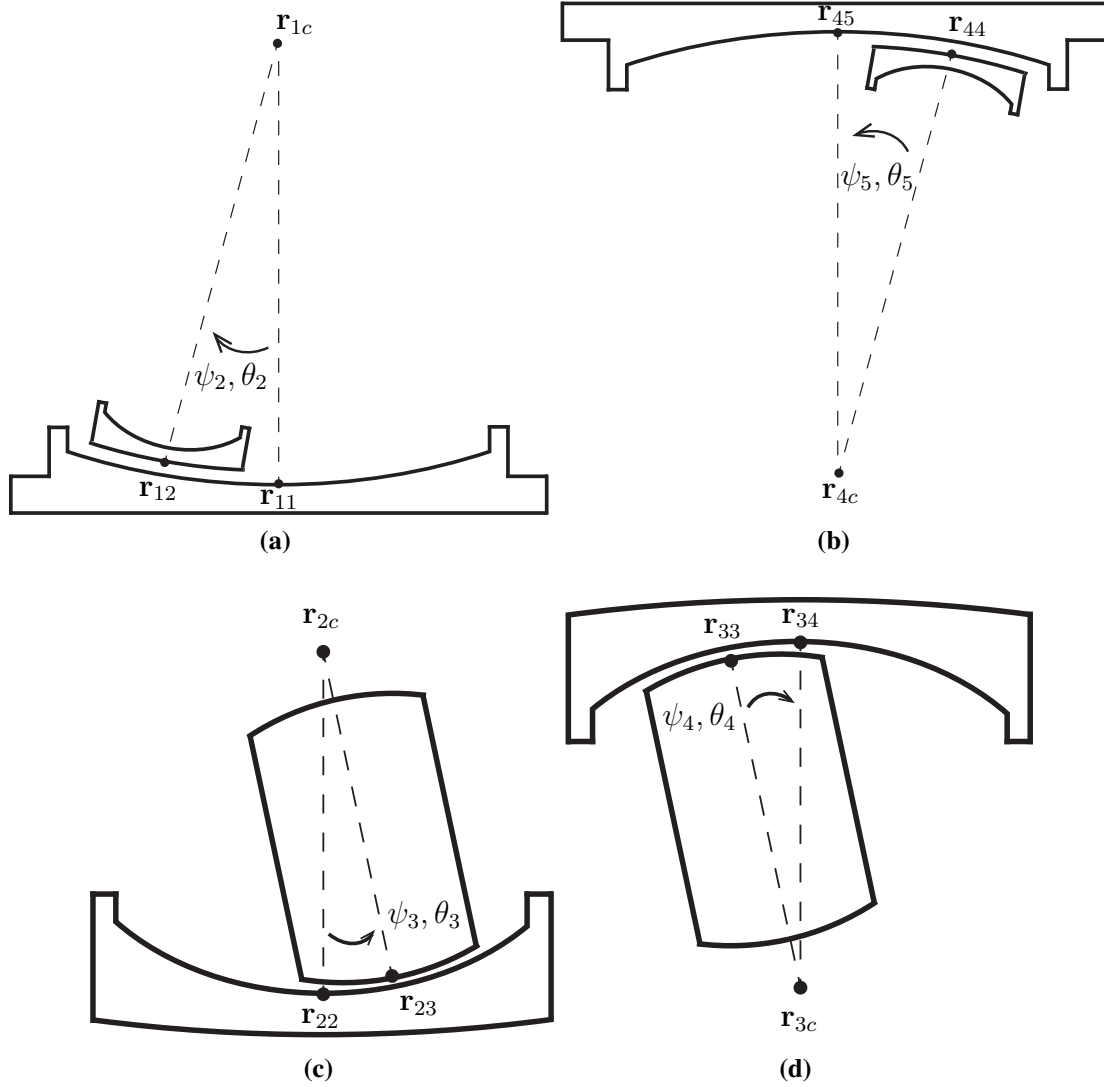
Fig. 5.4   Sliding angles for all four sliding surfaces.

which is the center of mass of bearing two,

$$\mathbf{r}_{22} = \mathbf{r}_2 + (\ell_2 - z_2)\mathbf{t}_3^2, \tag{5.13}$$

which is the center top of bearing two,

$$\mathbf{r}_{2c} = \mathbf{r}_{22} + R_2\mathbf{t}_3^2, \tag{5.14}$$

which is the center of the sphere created by the sliding surface with radius R_2,

$$\mathbf{r}_{23} = \mathbf{r}_{2c} - R_2\mathbf{t}_3^3, \tag{5.15}$$

which is the center bottom of bearing three,

$$\mathbf{r}_3 = \mathbf{r}_{23} + z_3\mathbf{t}_3^3, \tag{5.16}$$

which is the center of mass of bearing three,

$$\mathbf{r}_{33} = \mathbf{r}_3 + (\ell_3 - z_3)\mathbf{t}_3^3, \tag{5.17}$$

which is the center top of bearing three,

$$\mathbf{r}_{3c} = \mathbf{r}_{33} - R_3\mathbf{t}_3^3, \tag{5.18}$$

which is the center of the sphere created by the sliding surface with radius R_3,

$$\mathbf{r}_{34} = \mathbf{r}_{3c} + R_3\mathbf{t}_3^4, \tag{5.19}$$

which is the center bottom of bearing four,

$$\mathbf{r}_4 = \mathbf{r}_{34} + (\ell_4 - z_4)\mathbf{t}_3^4, \tag{5.20}$$

which is the center of mass of bearing four,

$$\mathbf{r}_{44} = \mathbf{r}_4 + z_4\mathbf{t}_3^4, \tag{5.21}$$

which is the center top of bearing four,

$$\mathbf{r}_{4c} = \mathbf{r}_{44} - R_4\mathbf{t}_3^4, \tag{5.22}$$

which is the center of the sphere created by the sliding surface with radius R_4,

$$\mathbf{r}_{45} = \mathbf{r}_{4c} + R_4\mathbf{t}_3^5, \tag{5.23}$$

which is center bottom of bearing five,

$$\mathbf{r}_5 = \mathbf{r}_{45} + (\ell_5 - z_5)\mathbf{t}_3^5, \tag{5.24}$$

which is the center of mass of bearing five and,

$$\mathbf{r}_{55} = \mathbf{r}_5 + z_5\mathbf{t}_3^5, \tag{5.25}$$

which is the center top of bearing five.

Now that all of the relevant position vectors have been defined, the velocity vectors associated with each position vector need to be defined. In addition, the angular velocities of each bearing are needed:

$$\boldsymbol{\omega}_1 = \dot{\theta}_1\mathbf{t}_2^1 + \dot{\psi}_1\mathbf{E}_1, \tag{5.26}$$

which is the angular velocity of bearing one excluding any rotation about the axis of symmetry,

$$\boldsymbol{\omega}_1^t = \dot{\phi}_1\mathbf{t}_3^1 + \boldsymbol{\omega}_1, \tag{5.27}$$

which is the total angular velocity of bearing one,

$$\boldsymbol{\omega}_2 = \dot{\theta}_2 \mathbf{t}_2^2 + \dot{\psi}_2 \mathbf{t}_1^1 + \boldsymbol{\omega}_1, \tag{5.28}$$

which is the angular velocity of bearing two excluding any rotation about the axis of symmetry,

$$\boldsymbol{\omega}_2^t = \dot{\phi}_2 \mathbf{t}_3^2 + \boldsymbol{\omega}_2, \tag{5.29}$$

which is the total angular velocity of bearing two,

$$\boldsymbol{\omega}_3 = \dot{\theta}_3 \mathbf{t}_2^3 + \dot{\psi}_3 \mathbf{t}_1^2 + \boldsymbol{\omega}_2, \tag{5.30}$$

which is the angular velocity of bearing three excluding any rotation about the axis of symmetry,

$$\boldsymbol{\omega}_3^t = \dot{\phi}_3 \mathbf{t}_3^3 + \boldsymbol{\omega}_3, \tag{5.31}$$

which is the total angular velocity of bearing three,

$$\boldsymbol{\omega}_4 = \dot{\theta}_4 \mathbf{t}_2^4 + \dot{\psi}_4 \mathbf{t}_1^3 + \boldsymbol{\omega}_3, \tag{5.32}$$

which is the angular velocity of bearing four excluding any rotation about the axis of symmetry,

$$\boldsymbol{\omega}_4^t = \dot{\phi}_4 \mathbf{t}_3^4 + \boldsymbol{\omega}_4, \tag{5.33}$$

which is the total angular velocity of bearing four,

$$\boldsymbol{\omega}_5 = \dot{\theta}_5 \mathbf{t}_2^5 + \dot{\psi}_5 \mathbf{t}_1^4 + \boldsymbol{\omega}_4, \tag{5.34}$$

which is the angular velocity of bearing five excluding any rotation about the axis of symmetry and

$$\boldsymbol{\omega}_5^t = \dot{\phi}_5 \mathbf{t}_3^5 + \boldsymbol{\omega}_5, \tag{5.35}$$

which is the total angular velocity of bearing five. And, using the following relations,

$$\dot{\mathbf{t}}_i^1 = \boldsymbol{\omega}_1 \times \mathbf{t}_i^1, \quad \dot{\mathbf{t}}_i^2 = \boldsymbol{\omega}_2 \times \mathbf{t}_i^2, \quad \dot{\mathbf{t}}_i^3 = \boldsymbol{\omega}_3 \times \mathbf{t}_i^3, \quad \dot{\mathbf{t}}_i^4 = \boldsymbol{\omega}_4 \times \mathbf{t}_i^4, \quad \dot{\mathbf{t}}_i^5 = \boldsymbol{\omega}_5 \times \mathbf{t}_i^5, \tag{5.36}$$

the velocity vectors are defined as follows:

$$\mathbf{v}_{01} = \dot{u}_{g1} \mathbf{E}_1 + \dot{u}_{g2} \mathbf{E}_2 + \dot{u}_{g3} \mathbf{E}_3, \tag{5.37}$$

$$\mathbf{v}_1 = \mathbf{v}_{01} + z_1 \boldsymbol{\omega}_1 \times \mathbf{t}_3^1, \tag{5.38}$$

$$\mathbf{v}_{11} = \mathbf{v}_1 + (\ell_1 - z_1) \boldsymbol{\omega}_1 \times \mathbf{t}_3^1, \tag{5.39}$$

$$\mathbf{v}_{1c} = \mathbf{v}_{11} + R_1 \boldsymbol{\omega}_1 \times \mathbf{t}_3^1, \tag{5.40}$$

$$\mathbf{v}_{12} = \mathbf{v}_{1c} - R_1 \boldsymbol{\omega}_2 \times \mathbf{t}_3^2, \tag{5.41}$$

$$\mathbf{v}_2 = \mathbf{v}_{12} + z_2 \boldsymbol{\omega}_2 \times \mathbf{t}_3^2, \tag{5.42}$$

$$\mathbf{v}_{22} = \mathbf{v}_2 + (\ell_2 - z_2)\boldsymbol{\omega}_2 \times \mathbf{t}_3^2, \tag{5.43}$$

$$\mathbf{v}_{2c} = \mathbf{v}_{22} + R_2 \boldsymbol{\omega}_2 \times \mathbf{t}_3^2, \tag{5.44}$$

$$\mathbf{v}_{23} = \mathbf{v}_{2c} - R_2 \boldsymbol{\omega}_3 \times \mathbf{t}_3^3, \tag{5.45}$$

$$\mathbf{v}_3 = \mathbf{v}_{23} + z_3 \boldsymbol{\omega}_3 \times \mathbf{t}_3^3, \tag{5.46}$$

$$\mathbf{v}_{33} = \mathbf{v}_3 + (\ell_3 - z_3)\boldsymbol{\omega}_3 \times \mathbf{t}_3^3, \tag{5.47}$$

$$\mathbf{v}_{3c} = \mathbf{v}_{33} - R_3 \boldsymbol{\omega}_3 \times \mathbf{t}_3^3, \tag{5.48}$$

$$\mathbf{v}_{34} = \mathbf{v}_{3c} + R_3 \boldsymbol{\omega}_4 \times \mathbf{t}_3^4, \tag{5.49}$$

$$\mathbf{v}_4 = \mathbf{v}_{34} + (\ell_4 - z_4)\boldsymbol{\omega}_4 \times \mathbf{t}_3^4, \tag{5.50}$$

$$\mathbf{v}_{44} = \mathbf{v}_4 + z_4 \boldsymbol{\omega}_4 \times \mathbf{t}_3^4, \tag{5.51}$$

$$\mathbf{v}_{4c} = \mathbf{v}_{44} - R_4 \boldsymbol{\omega}_4 \times \mathbf{t}_3^4, \tag{5.52}$$

$$\mathbf{v}_{45} = \mathbf{v}_{4c} + R_4 \boldsymbol{\omega}_5 \times \mathbf{t}_3^5, \tag{5.53}$$

$$\mathbf{v}_5 = \mathbf{v}_{45} + (\ell_5 - z_5)\boldsymbol{\omega}_5 \times \mathbf{t}_3^5, \tag{5.54}$$

$$\mathbf{v}_{55} = \mathbf{v}_5 + z_5 \boldsymbol{\omega}_5 \times \mathbf{t}_3^5, \tag{5.55}$$

where Eqs. (5.37)-(5.55) are the velocity vectors of the corresponding position vectors in Eqs. (5.7)-(5.25). Next, the following angular acceleration vectors are required:

$$\dot{\boldsymbol{\omega}}_1 = \ddot{\theta}_1 \mathbf{t}_2^1 + \boldsymbol{\omega}_1 \times \dot{\theta}_1 \mathbf{t}_2^1 + \ddot{\psi}_1 \mathbf{E}_1, \tag{5.56}$$

$$\dot{\boldsymbol{\omega}}_1^t = \ddot{\phi}_1 \mathbf{t}_3^1 + \boldsymbol{\omega}_1 \times \dot{\phi}_1 \mathbf{t}_3^1 + \dot{\boldsymbol{\omega}}_1, \tag{5.57}$$

$$\dot{\boldsymbol{\omega}}_2 = \ddot{\theta}_2 \mathbf{t}_2^2 + \boldsymbol{\omega}_2 \times \dot{\theta}_2 \mathbf{t}_2^2 + \ddot{\psi}_2 \mathbf{t}_1^1 + \boldsymbol{\omega}_1 \times \dot{\psi}_2 \mathbf{t}_1^1 + \dot{\boldsymbol{\omega}}_1, \tag{5.58}$$

$$\dot{\boldsymbol{\omega}}_2^t = \ddot{\phi}_2 \mathbf{t}_3^2 + \boldsymbol{\omega}_2 \times \dot{\phi}_2 \mathbf{t}_3^2 + \dot{\boldsymbol{\omega}}_2, \tag{5.59}$$

$$\dot{\boldsymbol{\omega}}_3 = \ddot{\theta}_3 \mathbf{t}_2^3 + \boldsymbol{\omega}_3 \times \dot{\theta}_3 \mathbf{t}_2^3 + \ddot{\psi}_3 \mathbf{t}_1^2 + \boldsymbol{\omega}_2 \times \dot{\psi}_3 \mathbf{t}_1^2 + \dot{\boldsymbol{\omega}}_2, \tag{5.60}$$

$$\dot{\boldsymbol{\omega}}_3^t = \ddot{\phi}_3 \mathbf{t}_3^3 + \boldsymbol{\omega}_3 \times \dot{\phi}_3 \mathbf{t}_3^3 + \dot{\boldsymbol{\omega}}_3, \tag{5.61}$$

$$\dot{\boldsymbol{\omega}}_4 = \ddot{\theta}_4 \mathbf{t}_2^4 + \boldsymbol{\omega}_4 \times \dot{\theta}_4 \mathbf{t}_2^4 + \ddot{\psi}_4 \mathbf{t}_1^3 + \boldsymbol{\omega}_3 \times \dot{\psi}_4 \mathbf{t}_1^3 + \dot{\boldsymbol{\omega}}_3, \tag{5.62}$$

$$\dot{\boldsymbol{\omega}}_4^t = \ddot{\phi}_4 \mathbf{t}_3^4 + \boldsymbol{\omega}_3 \times \dot{\phi}_4 \mathbf{t}_3^4 + \dot{\boldsymbol{\omega}}_4, \tag{5.63}$$

$$\dot{\boldsymbol{\omega}}_5 = \ddot{\theta}_5 \mathbf{t}_2^5 + \boldsymbol{\omega}_4 \times \dot{\theta}_5 \mathbf{t}_2^5 + \ddot{\psi}_5 \mathbf{t}_1^4 + \boldsymbol{\omega}_3 \times \dot{\psi}_5 \mathbf{t}_1^4 + \boldsymbol{\omega}_4, \tag{5.64}$$

$$\dot{\boldsymbol{\omega}}_5^t = \ddot{\phi}_5 \mathbf{t}_3^5 + \boldsymbol{\omega}_4 \times \dot{\phi}_5 \mathbf{t}_3^5 + \dot{\boldsymbol{\omega}}_5, \tag{5.65}$$

where Eqs. (5.56)-(5.65) are the angular acceleration vectors of the corresponding angular velocity vectors in Eqs. (5.26)-(5.35). Finally, the acceleration vectors of each of the above listed velocity vectors are defined as follows:

$$\dot{\mathbf{v}}_{01} = \ddot{u}_{g1} \mathbf{E}_1 + \ddot{u}_{g2} \mathbf{E}_2 + \ddot{u}_{g3} \mathbf{E}_3, \tag{5.66}$$

$$\dot{\mathbf{v}}_1 = \dot{\mathbf{v}}_{01} + z_1 \dot{\boldsymbol{\omega}}_1 \times \mathbf{t}_3^1 + z_1 \boldsymbol{\omega}_1 \times (\boldsymbol{\omega}_1 \times \mathbf{t}_3^1), \tag{5.67}$$

$$\dot{\mathbf{v}}_{11} = \dot{\mathbf{v}}_1 + (\ell_1 - z_1)\dot{\boldsymbol{\omega}}_1 \times \mathbf{t}_3^1 + (\ell_1 - z_1)\boldsymbol{\omega}_1 \times (\boldsymbol{\omega}_1 \times \mathbf{t}_3^1), \tag{5.68}$$

$$\dot{\mathbf{v}}_{1c} = \dot{\mathbf{v}}_{11} + R_1\dot{\boldsymbol{\omega}}_1 \times \mathbf{t}_3^1 + R_1\boldsymbol{\omega}_1 \times (\boldsymbol{\omega}_1 \times \mathbf{t}_3^1), \tag{5.69}$$

$$\dot{\mathbf{v}}_{12} = \dot{\mathbf{v}}_{1c} - R_1\dot{\boldsymbol{\omega}}_2 \times \mathbf{t}_3^2 - R_1\boldsymbol{\omega}_2 \times (\boldsymbol{\omega}_2 \times \mathbf{t}_3^2), \tag{5.70}$$

$$\dot{\mathbf{v}}_2 = \dot{\mathbf{v}}_{12} + z_2\dot{\boldsymbol{\omega}}_2 \times \mathbf{t}_3^2 + z_2\boldsymbol{\omega}_2 \times (\boldsymbol{\omega}_2 \times \mathbf{t}_3^2), \tag{5.71}$$

$$\dot{\mathbf{v}}_{22} = \dot{\mathbf{v}}_2 + (\ell_2 - z_2)\dot{\boldsymbol{\omega}}_2 \times \mathbf{t}_3^2 + (\ell_2 - z_2)\boldsymbol{\omega}_2 \times (\boldsymbol{\omega}_2 \times \mathbf{t}_3^2), \tag{5.72}$$

$$\dot{\mathbf{v}}_{2c} = \dot{\mathbf{v}}_{22} + R_2\dot{\boldsymbol{\omega}}_2 \times \mathbf{t}_3^2 + R_2\boldsymbol{\omega}_2 \times (\boldsymbol{\omega}_2 \times \mathbf{t}_3^2), \tag{5.73}$$

$$\dot{\mathbf{v}}_{23} = \dot{\mathbf{v}}_{2c} - R_2\dot{\boldsymbol{\omega}}_3 \times \mathbf{t}_3^3 - R_2\boldsymbol{\omega}_3 \times (\boldsymbol{\omega}_3 \times \mathbf{t}_3^3), \tag{5.74}$$

$$\dot{\mathbf{v}}_3 = \dot{\mathbf{v}}_{23} + z_3\dot{\boldsymbol{\omega}}_3 \times \mathbf{t}_3^3 + z_3\boldsymbol{\omega}_3 \times (\boldsymbol{\omega}_3 \times \mathbf{t}_3^3), \tag{5.75}$$

$$\dot{\mathbf{v}}_{33} = \dot{\mathbf{v}}_3 + (\ell_3 - z_3)\dot{\boldsymbol{\omega}}_3 \times \mathbf{t}_3^3 + (\ell_3 - z_3)\boldsymbol{\omega}_3 \times (\boldsymbol{\omega}_3 \times \mathbf{t}_3^3), \tag{5.76}$$

$$\dot{\mathbf{v}}_{3c} = \dot{\mathbf{v}}_{33} - R_3\dot{\boldsymbol{\omega}}_3 \times \mathbf{t}_3^3 - R_3\boldsymbol{\omega}_3 \times (\boldsymbol{\omega}_3 \times \mathbf{t}_3^3), \tag{5.77}$$

$$\dot{\mathbf{v}}_{34} = \dot{\mathbf{v}}_{3c} + R_3\dot{\boldsymbol{\omega}}_4 \times \mathbf{t}_3^4 + R_3\boldsymbol{\omega}_4 \times (\boldsymbol{\omega}_4 \times \mathbf{t}_3^4), \tag{5.78}$$

$$\dot{\mathbf{v}}_4 = \dot{\mathbf{v}}_{34} + (\ell_4 - z_4)\dot{\boldsymbol{\omega}}_4 \times \mathbf{t}_3^4 + (\ell_4 - z_4)\boldsymbol{\omega}_4 \times (\boldsymbol{\omega}_4 \times \mathbf{t}_3^4), \tag{5.79}$$

$$\dot{\mathbf{v}}_{44} = \dot{\mathbf{v}}_4 + z_4\dot{\boldsymbol{\omega}}_4 \times \mathbf{t}_3^4 + z_4\boldsymbol{\omega}_4 \times (\boldsymbol{\omega}_4 \times \mathbf{t}_3^4), \tag{5.80}$$

$$\dot{\mathbf{v}}_{4c} = \dot{\mathbf{v}}_{44} - R_4\dot{\boldsymbol{\omega}}_4 \times \mathbf{t}_3^4 - R_4\boldsymbol{\omega}_4 \times (\boldsymbol{\omega}_4 \times \mathbf{t}_3^4), \tag{5.81}$$

$$\dot{\mathbf{v}}_{45} = \dot{\mathbf{v}}_{4c} + R_4\dot{\boldsymbol{\omega}}_5 \times \mathbf{t}_3^5 + R_4\boldsymbol{\omega}_5 \times (\boldsymbol{\omega}_5 \times \mathbf{t}_3^5), \tag{5.82}$$

$$\dot{\mathbf{v}}_5 = \dot{\mathbf{v}}_{45} + (\ell_5 - z_5)\dot{\boldsymbol{\omega}}_5 \times \mathbf{t}_3^5 + (\ell_5 - z_5)\boldsymbol{\omega}_5 \times (\boldsymbol{\omega}_5 \times \mathbf{t}_3^5), \tag{5.83}$$

$$\dot{\mathbf{v}}_{55} = \dot{\mathbf{v}}_5 + z_5\dot{\boldsymbol{\omega}}_5 \times \mathbf{t}_3^5 + z_5\boldsymbol{\omega}_5 \times (\boldsymbol{\omega}_5 \times \mathbf{t}_3^5), \tag{5.84}$$

where Eqs. (5.66)-(5.84) are the acceleration vectors of the corresponding position vectors in Eqs. (5.7)-(5.25). The following vectors are all of the required vectors to properly describe the kinematics of the TFP.

Normal Forces

In order to look at the full kinetics of the TFP, all of the forces acting, both internally and externally, on the TFP need to be fully described. The first set of forces that act on the TFP are the internal normal forces. From a moment balance, the normal forces will not necessarily be acting at the center point of the contact between bearings [53], which requires another set of 1-2 Euler angles to define the location of each internal normal force. These Euler angles and their associated basis vectors shall be denoted with a superscribed $\tilde{}$, such as $\tilde{\psi}_1$ and $\tilde{\mathbf{t}}_1^1$. The basis vectors for each normal force position is given as

$$\tilde{\mathbf{t}}_i^1 = \tilde{\mathbf{R}}_1\mathbf{t}_i^1, \quad \tilde{\mathbf{t}}_i^2 = \tilde{\mathbf{R}}_2\mathbf{t}_i^2, \quad \tilde{\mathbf{t}}_i^3 = \tilde{\mathbf{R}}_3\mathbf{t}_i^3, \quad \tilde{\mathbf{t}}_i^4 = \tilde{\mathbf{R}}_4\mathbf{t}_i^4, \tag{5.85}$$

where

$$\tilde{\mathbf{R}}_1 = \mathbf{R}(\tilde{\psi}_1, \tilde{\theta}_1; \mathbf{t}_i^1), \quad \tilde{\mathbf{R}}_2 = \mathbf{R}(\tilde{\psi}_2, \tilde{\theta}_2; \mathbf{t}_i^2),$$
$$\tilde{\mathbf{R}}_3 = \mathbf{R}(\tilde{\psi}_3, \tilde{\theta}_3; \mathbf{t}_i^3), \quad \tilde{\mathbf{R}}_4 = \mathbf{R}(\tilde{\psi}_4, \tilde{\theta}_4; \mathbf{t}_i^4), \tag{5.86}$$

where $\mathbf{R}$ has the same definition as in Eq. (5.3). The position of each normal force is defined as:

$$\tilde{\mathbf{r}}_1 = \mathbf{r}_{1c} - R_1 \tilde{\mathbf{t}}_3^1, \tag{5.87}$$

which is the position of the normal force on the sliding surface with radius R_1,

$$\tilde{\mathbf{r}}_2 = \mathbf{r}_{2c} - R_2 \tilde{\mathbf{t}}_3^2, \tag{5.88}$$

which is the position of the normal force on the sliding surface with radius R_2,

$$\tilde{\mathbf{r}}_3 = \mathbf{r}_{3c} + R_3 \tilde{\mathbf{t}}_3^3, \tag{5.89}$$

which is the position of the normal force on the sliding surface with radius R_3,

$$\tilde{\mathbf{r}}_4 = \mathbf{r}_{4c} + R_4 \tilde{\mathbf{t}}_3^4, \tag{5.90}$$

which is the position of the normal force on the sliding surface with radius R_4. Finally, the normal forces are defined as

$$\mathbf{N}_1 = N_1 \tilde{\mathbf{t}}_3^1, \quad \mathbf{N}_2 = N_2 \tilde{\mathbf{t}}_3^2, \quad \mathbf{N}_3 = N_3 \tilde{\mathbf{t}}_3^3, \quad \mathbf{N}_4 = N_4 \tilde{\mathbf{t}}_3^4, \tag{5.91}$$

where N_α are the magnitudes of the normal forces. This is all of the required information to define the internal normal forces.

Friction Forces

The next set of forces acting on the TFP are the friction forces that act between bearings at each of the sliding surfaces. The friction forces act at the same locations as the normal forces, thus they will use the same set of basis vectors and Euler angles previously defined. The dynamic friction forces act in the plane normal to the normal forces and are defined as

$$\mathbf{F}_{f1} = -\mu_1 N_1 \tilde{\mathbf{f}}_1, \quad \mathbf{F}_{f2} = -\mu_2 N_2 \tilde{\mathbf{f}}_2, \quad \mathbf{F}_{f3} = -\mu_3 N_3 \tilde{\mathbf{f}}_3, \quad \mathbf{F}_{f4} = -\mu_4 N_4 \tilde{\mathbf{f}}_4, \tag{5.92}$$

where μ_α are the coefficient of frictions for each pair of sliding surfaces and the $\tilde{\mathbf{f}}_\alpha$ vectors define the direction in which the friction forces act and are given by,

$$\tilde{\mathbf{f}}_1 = Y_1 \tilde{\mathbf{t}}_1^1 + Z_1 \tilde{\mathbf{t}}_2^1, \quad \tilde{\mathbf{f}}_2 = Y_2 \tilde{\mathbf{t}}_1^2 + Z_2 \tilde{\mathbf{t}}_2^2, \tag{5.93}$$
$$\tilde{\mathbf{f}}_3 = Y_3 \tilde{\mathbf{t}}_1^3 + Z_3 \tilde{\mathbf{t}}_2^3, \quad \tilde{\mathbf{f}}_4 = Y_4 \tilde{\mathbf{t}}_1^4 + Z_4 \tilde{\mathbf{t}}_2^4,$$

where the Y_α and Z_α are used to define the direction of the friction forces in the plane normal to the normal forces. These values are determined using a modified Bouc-Wen model for biaxial hysteresis [49, 34], given as follows:

$$\dot{Y}_1 = \frac{R_1}{R_0} \left((1 - a_1 Y_1^2)\tilde{u}_1 - b_1 Y_1 Z_1 \tilde{v}_1 \right) \quad a_1 = \begin{cases} 1, & Y_1 \tilde{u}_1 > 0 \\ 0, & Y_1 \tilde{u}_1 \le 0 \end{cases} \tag{5.94}$$

$$\dot{Z}_1 = \frac{R_1}{R_0} \left((1 - b_1 Z_1^2)\tilde{v}_1 - a_1 Y_1 Z_1 \tilde{u}_1 \right) \quad b_1 = \begin{cases} 1, & Z_1 \tilde{v}_1 > 0 \\ 0, & Z_1 \tilde{v}_1 \le 0 \end{cases}$$

$$\dot{Y}_2 = \frac{R_2}{R_0}\left((1-a_2Y_2^2)\tilde{u}_2 - b_2Y_2Z_2\tilde{v}_2\right) \quad a_2 = \begin{cases} 1, & Y_2\tilde{u}_2 > 0 \\ 0, & Y_2\tilde{u}_2 \leq 0 \end{cases} \tag{5.95}$$

$$\dot{Z}_2 = \frac{R_2}{R_0}\left((1-b_2Z_2^2)\tilde{v}_2 - a_2Y_2Z_2\tilde{u}_2\right) \quad b_2 = \begin{cases} 1, & Z_2\tilde{v}_2 > 0 \\ 0, & Z_2\tilde{v}_2 \leq 0 \end{cases}$$

$$\dot{Y}_3 = \frac{R_3}{R_0}\left((1-a_3Y_3^2)\tilde{u}_3 - b_3Y_3Z_3\tilde{v}_3\right) \quad a_3 = \begin{cases} 1, & Y_3\tilde{u}_3 > 0 \\ 0, & Y_3\tilde{u}_3 \leq 0 \end{cases} \tag{5.96}$$

$$\dot{Z}_3 = \frac{R_3}{R_0}\left((1-b_3Z_3^2)\tilde{v}_3 - a_3Y_3Z_3\tilde{u}_3\right) \quad b_3 = \begin{cases} 1, & Z_3\tilde{v}_3 > 0 \\ 0, & Z_3\tilde{v}_3 \leq 0 \end{cases}$$

$$\dot{Y}_4 = \frac{R_4}{R_0}\left((1-a_4Y_4^2)\tilde{u}_4 - b_4Y_4Z_4\tilde{v}_4\right) \quad a_4 = \begin{cases} 1, & Y_4\tilde{u}_4 > 0 \\ 0, & Y_4\tilde{u}_4 \leq 0 \end{cases} \tag{5.97}$$

$$\dot{Z}_4 = \frac{R_4}{R_0}\left((1-b_4Z_4^2)\tilde{v}_4 - a_4Y_4Z_4\tilde{u}_4\right) \quad b_4 = \begin{cases} 1, & Z_4\tilde{v}_4 > 0 \\ 0, & Z_4\tilde{v}_4 \leq 0 \end{cases}$$

where R_0 is the yield radius and $\tilde{u}_\alpha$ and $\tilde{v}_\alpha$ are the orthogonal in-plane components of the relative velocity at the point where the friction forces act and are given by

$$\tilde{u}_1 = \tilde{\mathbf{v}}_1 \cdot \tilde{\mathbf{t}}_1^1, \quad \tilde{v}_1 = \tilde{\mathbf{v}}_1 \cdot \tilde{\mathbf{t}}_2^1, \quad \tilde{u}_2 = \tilde{\mathbf{v}}_2 \cdot \tilde{\mathbf{t}}_1^2, \quad \tilde{v}_2 = \tilde{\mathbf{v}}_2 \cdot \tilde{\mathbf{t}}_2^2 \tag{5.98}$$
$$\tilde{u}_3 = \tilde{\mathbf{v}}_3 \cdot \tilde{\mathbf{t}}_1^3, \quad \tilde{v}_3 = \tilde{\mathbf{v}}_3 \cdot \tilde{\mathbf{t}}_2^3, \quad \tilde{u}_4 = \tilde{\mathbf{v}}_4 \cdot \tilde{\mathbf{t}}_1^4, \quad \tilde{v}_4 = \tilde{\mathbf{v}}_4 \cdot \tilde{\mathbf{t}}_2^4,$$

where $\tilde{\mathbf{v}}_\alpha$ are the relative velocity vectors at the points where the friction forces act and are given by

$$\tilde{\mathbf{v}}_1 = -R_1(\boldsymbol{\omega}_2^t - \boldsymbol{\omega}_1^t) \times \tilde{\mathbf{t}}_3^1, \quad \tilde{\mathbf{v}}_2 = -R_2(\boldsymbol{\omega}_3^t - \boldsymbol{\omega}_2^t) \times \tilde{\mathbf{t}}_3^2, \tag{5.99}$$
$$\tilde{\mathbf{v}}_3 = R_3(\boldsymbol{\omega}_4^t - \boldsymbol{\omega}_3^t) \times \tilde{\mathbf{t}}_3^3, \quad \tilde{\mathbf{v}}_4 = R_4(\boldsymbol{\omega}_5^t - \boldsymbol{\omega}_4^t) \times \tilde{\mathbf{t}}_3^4.$$

This gives all of the necessary information to fully define the friction forces.

Contact Forces

The last set of forces acting on the TFP are the forces that occur when two bearings contact one another when the maximum sliding displacement has been reached for a given sliding surface. To model this force, a spring-damper system will be imposed at the contact point. First, the amount of relative sliding between bearings for each sliding surface is given as

$$s_1 = R_1 \cos^{-1}\left(\mathbf{t}_3^1 \cdot \mathbf{t}_3^2\right), \quad s_2 = R_2 \cos^{-1}\left(\mathbf{t}_3^2 \cdot \mathbf{t}_3^3\right), \tag{5.100}$$
$$s_3 = R_3 \cos^{-1}\left(\mathbf{t}_3^3 \cdot \mathbf{t}_3^4\right), \quad s_4 = R_4 \cos^{-1}\left(\mathbf{t}_3^4 \cdot \mathbf{t}_3^5\right).$$

The gap functions are then defined as

$$g_1 = s_{c1} - s_1, \quad g_2 = s_{c2} - s_2, \quad g_3 = s_{c3} - s_3, \quad g_4 = s_{c4} - s_4, \tag{5.101}$$

where $s_{c\alpha}$ is the maximum sliding displacement before contact. Thus, if g_α is positive, there is no contact, and if g_α is negative, there is contact. The velocity of the gap is defined as

$$\gamma_1 = \dot{g}_1, \quad \gamma_2 = \dot{g}_2, \quad \gamma_3 = \dot{g}_3, \quad \gamma_4 = \dot{g}_4. \tag{5.102}$$

The magnitude of the contact forces become

$$F_{c1} = \begin{cases} 0 & , g_1 > 0 \\ k_{c1}g_1 + c_{c1}\gamma_1 & , g_1 \leq 0 \end{cases} \tag{5.103}$$

$$F_{c2} = \begin{cases} 0 & , g_2 > 0 \\ k_{c2}g_2 + c_{c2}\gamma_2 & , g_2 \leq 0 \end{cases} \tag{5.104}$$

$$F_{c3} = \begin{cases} 0 & , g_3 > 0 \\ k_{c3}g_3 + c_{c3}\gamma_3 & , g_3 \leq 0 \end{cases} \tag{5.105}$$

$$F_{c4} = \begin{cases} 0 & , g_4 > 0 \\ k_{c4}g_4 + c_{c4}\gamma_4 & , g_4 \leq 0 \end{cases} \tag{5.106}$$

where $k_{c\alpha}$ and $c_{c\alpha}$ are, respectively, the stiffness and damping constants for the contact forces. And the contact forces become

$$\mathbf{F}_{c1} = F_{c1}\bar{\mathbf{f}}_1, \quad \mathbf{F}_{c2} = F_{c2}\bar{\mathbf{f}}_2, \quad \mathbf{F}_{c3} = F_{c3}\bar{\mathbf{f}}_3, \quad \mathbf{F}_{c4} = F_{c4}\bar{\mathbf{f}}_4, \tag{5.107}$$

where the direction of the normal forces are given by

$$\bar{\mathbf{f}}_1 = \frac{(\mathbf{t}_3^1 \cdot \mathbf{t}_1^2)\mathbf{t}_1^2 + (\mathbf{t}_3^1 \cdot \mathbf{t}_2^2)\mathbf{t}_2^2}{\sqrt{(\mathbf{t}_3^1 \cdot \mathbf{t}_1^2)^2 + (\mathbf{t}_3^1 \cdot \mathbf{t}_2^2)^2}}, \quad \bar{\mathbf{f}}_2 = \frac{(\mathbf{t}_3^2 \cdot \mathbf{t}_1^3)\mathbf{t}_1^3 + (\mathbf{t}_3^2 \cdot \mathbf{t}_2^3)\mathbf{t}_2^3}{\sqrt{(\mathbf{t}_3^2 \cdot \mathbf{t}_1^3)^2 + (\mathbf{t}_3^2 \cdot \mathbf{t}_2^3)^2}},$$

$$\bar{\mathbf{f}}_3 = \frac{(\mathbf{t}_3^4 \cdot \mathbf{t}_1^3)\mathbf{t}_1^3 + (\mathbf{t}_3^4 \cdot \mathbf{t}_2^3)\mathbf{t}_2^3}{\sqrt{(\mathbf{t}_3^4 \cdot \mathbf{t}_1^3)^2 + (\mathbf{t}_3^4 \cdot \mathbf{t}_2^3)^2}}, \quad \bar{\mathbf{f}}_4 = \frac{(\mathbf{t}_3^5 \cdot \mathbf{t}_1^4)\mathbf{t}_1^4 + (\mathbf{t}_3^5 \cdot \mathbf{t}_2^4)\mathbf{t}_2^4}{\sqrt{(\mathbf{t}_3^5 \cdot \mathbf{t}_1^4)^2 + (\mathbf{t}_3^5 \cdot \mathbf{t}_2^4)^2}}. \tag{5.108}$$

The contact forces will act at the following positions:

$$\bar{\mathbf{r}}_1 = r_2\bar{\mathbf{f}}_1 + p_2\mathbf{t}_3^2 + \mathbf{r}_{12}, \quad \bar{\mathbf{r}}_2 = r_3\bar{\mathbf{f}}_2 + p_3\mathbf{t}_3^3 + \mathbf{r}_{23}, \tag{5.109}$$

$$\bar{\mathbf{r}}_3 = r_3\bar{\mathbf{f}}_3 - p_3\mathbf{t}_3^3 + \mathbf{r}_{33}, \quad \bar{\mathbf{r}}_4 = r_4\bar{\mathbf{f}}_4 - p_4\mathbf{t}_3^4 + \mathbf{r}_{44}.$$

All of the required information needed to define the contact forces between the bearings has now been defined.

Equations of Motion

Now that all of the required kinematics and forces have been defined, the equations of motion for the TFP can be established. In this model, it is assumed that the motion of the base bearing is fully prescribed, meaning u_{g1}, u_{g2}, u_{g3}, ψ_1, θ_1, and ϕ_1, and all required time derivatives, are provided. It is also assumed that the force and moment on the top bearing – $\mathbf{F}_{top}$ and $\mathbf{M}_{top}$ – are also provided. From a balance of linear momentum applied to each of the bearings, the following equations are defined:

$$m_2\dot{\mathbf{v}}_2 = \mathbf{N}_1 + \mathbf{F}_{f1} + \mathbf{F}_{c1} - \mathbf{N}_2 - \mathbf{F}_{f2} - \mathbf{F}_{c2} - m_2 g\mathbf{E}_3, \tag{5.110}$$

$$m_3\dot{\mathbf{v}}_3 = \mathbf{N}_2 + \mathbf{F}_{f2} + \mathbf{F}_{c2} - \mathbf{N}_3 - \mathbf{F}_{f3} - \mathbf{F}_{c3} - m_3 g\mathbf{E}_3, \tag{5.111}$$

$$m_4\dot{\mathbf{v}}_4 = \mathbf{N}_3 + \mathbf{F}_{f3} + \mathbf{F}_{c3} - \mathbf{N}_4 - \mathbf{F}_{f4} - \mathbf{F}_{c4} - m_4 g\mathbf{E}_3, \tag{5.112}$$

$$m_5\dot{\mathbf{v}}_5 = \mathbf{N}_4 + \mathbf{F}_{f4} + \mathbf{F}_{c4} + \mathbf{F}_{top} - m_5 g\mathbf{E}_3, \tag{5.113}$$

where g is the gravitational acceleration and m_α is the mass of the bearing. After applying a balance of angular momentum to each bearing, the following equations are defined:

$$\mathbf{J}_2\dot{\boldsymbol{\omega}}_2^t + \boldsymbol{\omega}_2^t \times \mathbf{J}_2\boldsymbol{\omega}_2^t = (\tilde{\mathbf{r}}_1 - \mathbf{r}_2) \times (\mathbf{N}_1 + \mathbf{F}_{f1}) - (\tilde{\mathbf{r}}_2 - \mathbf{r}_2) \times (\mathbf{N}_2 + \mathbf{F}_{f2}) \tag{5.114}$$
$$+ (\bar{\mathbf{r}}_1 - \mathbf{r}_2) \times \mathbf{F}_{c1} - (\bar{\mathbf{r}}_2 - \mathbf{r}_2) \times \mathbf{F}_{c2},$$

$$\mathbf{J}_3\dot{\boldsymbol{\omega}}_3^t + \boldsymbol{\omega}_3^t \times \mathbf{J}_3\boldsymbol{\omega}_3^t = (\tilde{\mathbf{r}}_2 - \mathbf{r}_3) \times (\mathbf{N}_2 + \mathbf{F}_{f2}) - (\tilde{\mathbf{r}}_3 - \mathbf{r}_3) \times (\mathbf{N}_3 + \mathbf{F}_{f3}) \tag{5.115}$$
$$+ (\bar{\mathbf{r}}_2 - \mathbf{r}_3) \times \mathbf{F}_{c2} - (\bar{\mathbf{r}}_3 - \mathbf{r}_3) \times \mathbf{F}_{c3},$$

$$\mathbf{J}_4\dot{\boldsymbol{\omega}}_4^t + \boldsymbol{\omega}_4^t \times \mathbf{J}_4\boldsymbol{\omega}_4^t = (\tilde{\mathbf{r}}_3 - \mathbf{r}_4) \times (\mathbf{N}_3 + \mathbf{F}_{f3}) - (\tilde{\mathbf{r}}_4 - \mathbf{r}_4) \times (\mathbf{N}_4 + \mathbf{F}_{f4}) \tag{5.116}$$
$$+ (\bar{\mathbf{r}}_3 - \mathbf{r}_4) \times \mathbf{F}_{c3} - (\bar{\mathbf{r}}_4 - \mathbf{r}_4) \times \mathbf{F}_{c4},$$

$$\mathbf{J}_5\dot{\boldsymbol{\omega}}_5^t + \boldsymbol{\omega}_5^t \times \mathbf{J}_5\boldsymbol{\omega}_5^t = (\tilde{\mathbf{r}}_4 - \mathbf{r}_5) \times (\mathbf{N}_4 + \mathbf{F}_{f4}) + (\bar{\mathbf{r}}_4 - \mathbf{r}_5) \times \mathbf{F}_{c4} \tag{5.117}$$
$$+ (\mathbf{r}_{55} - \mathbf{r}_5) \times \mathbf{F}_{top} + \mathbf{M}_{top},$$

where $\mathbf{J}_\alpha$ is the mass moment of inertia tensor for each of the bearings, and is defined as

$$\mathbf{J}_\alpha = \sum_{i=1}^{3} \lambda_i^\alpha \mathbf{t}_i^\alpha \otimes \mathbf{t}_i^\alpha, \tag{5.118}$$

where λ_i^α are the principal moments of inertia of each bearing.

Eqs. (5.110)-(5.117) provide 24 independent equations for the 24 unknowns, which are

$$\begin{bmatrix} \ddot{\psi}_2 & \ddot{\theta}_2 & \ddot{\phi}_2 & \ddot{\psi}_3 & \ddot{\theta}_3 & \ddot{\phi}_3 & \ddot{\psi}_4 & \ddot{\theta}_4 & \ddot{\phi}_4 & \ddot{\psi}_5 & \ddot{\theta}_5 & \ddot{\phi}_5 \\ \tilde{\psi}_1 & \tilde{\theta}_1 & \tilde{\psi}_2 & \tilde{\theta}_2 & \tilde{\psi}_3 & \tilde{\theta}_3 & \tilde{\psi}_4 & \tilde{\theta}_4 & N_1 & N_2 & N_3 & N_4 \end{bmatrix} \tag{5.119}$$

Note that the equations are non-linear in the unknowns and must be solved using an iterative solver, such as Newton's method. After which, a time integrator, such as the Runge-Kutta methods, can be used to solve for the time-history of the TFP.

5.3 Expanding to MSFPs

In the previous section, the equations of motion for the TFP are defined, but now those equations will be expanded to MSFPs with any number of bearings. Assume that there is a MSFP with n bearings, which means there are $n-1$ sliding surfaces, and of those $n-1$ sliding surfaces, m are concave up and $p = n-1-m$ are concave down. Let α be a counting parameter that runs from 1 to m, let β be another counting parameter that runs from $m+1$ to $n-1$, and let γ be a third counting parameter that runs from 1 to $n-1$. Note that for the TFP of the previous section $n = 5$, $m = 2$, and $p = 2$, thus $\alpha = 1,2$, $\beta = 3,4$, and $\gamma = 1,2,3,4$. Using the previous definitions, all of the necessary equations to describe the motion of an MSFP can be compactly written, where the position vectors become

$$\mathbf{r}_{01} = u_{g1}\mathbf{E}_1 + u_{g2}\mathbf{E}_2 + u_{g3}\mathbf{E}_3, \tag{5.120}$$

$$\mathbf{r}_1 = \mathbf{r}_{01} + z_1\mathbf{t}_3^1, \tag{5.121}$$

$$\mathbf{r}_{11} = \mathbf{r}_1 + (\ell_1 - z_1)\mathbf{t}_3^1, \tag{5.122}$$

$$\mathbf{r}_{\alpha c} = \mathbf{r}_{\alpha,\alpha} + R_\alpha\mathbf{t}_3^\alpha, \tag{5.123}$$

$$\mathbf{r}_{\alpha,\alpha+1} = \mathbf{r}_{\alpha c} - R_\alpha\mathbf{t}_3^{\alpha+1}, \tag{5.124}$$

$$\mathbf{r}_{\alpha+1} = \mathbf{r}_{\alpha,\alpha+1} + z_{\alpha+1}\mathbf{t}_3^{\alpha+1}, \tag{5.125}$$

$$\mathbf{r}_{\alpha+1,\alpha+1} = \mathbf{r}_{\alpha+1} + (\ell_{\alpha+1} - z_{\alpha+1})\mathbf{t}_3^{\alpha+1}, \tag{5.126}$$

$$\mathbf{r}_{\beta c} = \mathbf{r}_{\beta,\beta} - R_\beta\mathbf{t}_3^\beta, \tag{5.127}$$

$$\mathbf{r}_{\beta,\beta+1} = \mathbf{r}_{\beta c} + R_\beta\mathbf{t}_3^{\beta+1}, \tag{5.128}$$

$$\mathbf{r}_{\beta+1} = \mathbf{r}_{\beta,\beta+1} + (\ell_{\beta+1} - z_{\beta+1})\mathbf{t}_3^{\beta+1}, \tag{5.129}$$

$$\mathbf{r}_{\beta+1,\beta+1} = \mathbf{r}_{\beta+1} + z_{\beta+1}\mathbf{t}_3^{\beta+1}, \tag{5.130}$$

where all position vectors here have similar physical representations as those from Eqs (5.7)-(5.25). Similar representations exist for the velocity and acceleration vectors. The angular velocity vectors become

$$\boldsymbol{\omega}_1 = \dot{\theta}_1\mathbf{t}_2^1 + \dot{\psi}_1\mathbf{E}_1, \quad \boldsymbol{\omega}_1^t = \dot{\phi}_1\mathbf{t}_3^1 + \boldsymbol{\omega}_1, \tag{5.131}$$

$$\boldsymbol{\omega}_{\gamma+1} = \dot{\theta}_{\gamma+1}\mathbf{t}_2^{\gamma+1} + \dot{\psi}_{\gamma+1}\mathbf{t}_1^\gamma + \boldsymbol{\omega}_\gamma, \quad \boldsymbol{\omega}_{\gamma+1}^t = \dot{\phi}_{\gamma+1}\mathbf{t}_3^{\gamma+1} + \boldsymbol{\omega}_{\gamma+1},$$

where the angular velocity vectors have similar physical meaning as the corresponding vectors from Eqs. (5.26)-(5.35). Similar representations exist for the angular acceleration vectors. The normal force basis becomes

$$\tilde{\mathbf{t}}_i^\gamma = \tilde{\mathbf{R}}_\gamma\mathbf{t}_i^\gamma \tag{5.132}$$

with the normal forces acting at the following positions:

$$\tilde{\mathbf{r}}_\alpha = \mathbf{r}_{\alpha c} - R_\alpha\tilde{\mathbf{t}}_3^\alpha, \quad \tilde{\mathbf{r}}_\beta = \mathbf{r}_{\beta c} + R_\beta\tilde{\mathbf{t}}_3^\beta. \tag{5.133}$$

The normal forces are then given as

$$\mathbf{N}_\gamma = N_\gamma \tilde{\mathbf{t}}_3^\gamma. \tag{5.134}$$

Next, the friction forces become

$$\mathbf{F}_{f\gamma} = -\mu_\gamma N_\gamma \tilde{\mathbf{f}}_\gamma \tag{5.135}$$

where the direction of the friction forces come from

$$\tilde{\mathbf{f}}_\gamma = Y_\gamma \tilde{\mathbf{t}}_1^\gamma + Z_\gamma \tilde{\mathbf{t}}_2^\gamma, \tag{5.136}$$

and

$$\dot{Y}_\gamma = \frac{R_\gamma}{R_0}\left((1 - a_\gamma Y_\gamma^2)\tilde{u}_\gamma - b_\gamma Y_\gamma Z_\gamma \tilde{v}_\gamma\right) \quad a_\gamma = \begin{cases} 1, & Y_\gamma \tilde{u}_\gamma > 0 \\ 0, & Y_\gamma \tilde{u}_\gamma \le 0 \end{cases} \tag{5.137}$$

$$\dot{Z}_\gamma = \frac{R_\gamma}{R_0}\left((1 - b_\gamma Z_\gamma^2)\tilde{v}_\gamma - a_\gamma Y_\gamma Z_\gamma \tilde{u}_\gamma\right) \quad b_\gamma = \begin{cases} 1, & Z_\gamma \tilde{v}_\gamma > 0 \\ 0, & Z_\gamma \tilde{v}_\gamma \le 0 \end{cases}.$$

The relative velocity at the point that the friction forces act is then defined as

$$\tilde{\mathbf{v}}_\alpha = -R_\alpha(\boldsymbol{\omega}_{\alpha+1}^t - \boldsymbol{\omega}_\alpha^t) \times \tilde{\mathbf{t}}_3^\alpha, \quad \tilde{\mathbf{v}}_\beta = R_\beta(\boldsymbol{\omega}_{\beta+1}^t - \boldsymbol{\omega}_\beta^t) \times \tilde{\mathbf{t}}_3^\beta. \tag{5.138}$$

The sliding displacements and gap functions for each sliding surface become

$$s_\gamma = R_\gamma \cos^{-1}\left(\mathbf{t}_3^\gamma \cdot \mathbf{t}_3^{\gamma+1}\right), \tag{5.139}$$

and

$$g_\gamma = s_{c\gamma} - s_\gamma, \tag{5.140}$$

which makes the contact forces

$$\mathbf{F}_{c\gamma} = F_{c\gamma}\bar{\mathbf{f}}_\gamma, \tag{5.141}$$

where the magnitude of the contact forces are given by

$$F_{c\gamma} = \begin{cases} 0 & , g_\gamma > 0 \\ k_{c\gamma} g_\gamma + c_{c\gamma} \gamma_\gamma & , g_\gamma \le 0 \end{cases}, \tag{5.142}$$

and the direction of the contact forces are given by

$$\bar{\mathbf{f}}_\alpha = \frac{(\mathbf{t}_3^\alpha \cdot \mathbf{t}_1^{\alpha+1})\mathbf{t}_1^{\alpha+1} + (\mathbf{t}_3^\alpha \cdot \mathbf{t}_2^{\alpha+1})\mathbf{t}_2^{\alpha+1}}{\sqrt{(\mathbf{t}_3^\alpha \cdot \mathbf{t}_1^{\alpha+1})^2 + (\mathbf{t}_3^\alpha \cdot \mathbf{t}_2^{\alpha+1})^2}}, \tag{5.143}$$

$$\bar{\mathbf{f}}_\beta = \frac{(\mathbf{t}_3^{\beta+1} \cdot \mathbf{t}_1^\beta)\mathbf{t}_1^\beta + (\mathbf{t}_3^{\beta+1} \cdot \mathbf{t}_2^\beta)\mathbf{t}_2^\beta}{\sqrt{(\mathbf{t}_3^{\beta+1} \cdot \mathbf{t}_1^\beta)^2 + (\mathbf{t}_3^{\beta+1} \cdot \mathbf{t}_2^\beta)^2}}.$$

The contact forces will act at the following positions:

$$\bar{\mathbf{r}}_\alpha = r_{\alpha+1}\bar{\mathbf{f}}_\alpha + p_{\alpha+1}\mathbf{t}_3^{\alpha+1} + \mathbf{r}_{\alpha,\alpha+1}, \quad \bar{\mathbf{r}}_\beta = r_\beta\bar{\mathbf{f}}_\beta - p_\beta\mathbf{t}_3^\beta + \mathbf{r}_{\beta,\beta}. \tag{5.144}$$

Finally, the equations of motion become

$$m_{\gamma+1}\dot{\mathbf{v}}_{\gamma+1} = \mathbf{N}_\gamma + \mathbf{F}_{f\gamma} + \mathbf{F}_{c\gamma} - \mathbf{N}_{\gamma+1} - \mathbf{F}_{f\gamma+1} - \mathbf{F}_{c\gamma+1} - m_{\gamma+1}g\mathbf{E}_3, \tag{5.145}$$

and

$$\begin{aligned}
\mathbf{J}_{\gamma+1}\dot{\boldsymbol{\omega}}_{\gamma+1}^t + \boldsymbol{\omega}_{\gamma+1}^t \times \mathbf{J}_{\gamma+1}\boldsymbol{\omega}_{\gamma+1}^t =& (\tilde{\mathbf{r}}_\gamma - \mathbf{r}_{\gamma+1}) \times (\mathbf{N}_\gamma + \mathbf{F}_{f\gamma}) \\
&- (\tilde{\mathbf{r}}_{\gamma+1} - \mathbf{r}_{\gamma+1}) \times (\mathbf{N}_{\gamma+1} + \mathbf{F}_{f\gamma+1}) \\
&+ (\bar{\mathbf{r}}_\gamma - \mathbf{r}_{\gamma+1}) \times \mathbf{F}_{c\gamma} - (\bar{\mathbf{r}}_{\gamma+1} - \mathbf{r}_{\gamma+1}) \times \mathbf{F}_{c\gamma+1},
\end{aligned} \tag{5.146}$$

except that the top bearing has a modified set of equations to account for the applied force and moment – $\mathbf{F}_{top}$ and $\mathbf{M}_{top}$ – on the top bearing, given as

$$m_n\dot{\mathbf{v}}_n = \mathbf{N}_{n-1} + \mathbf{F}_{fn-1} + \mathbf{F}_{cn-1} + \mathbf{F}_{top} - m_n g\mathbf{E}_3, \tag{5.147}$$

and

$$\begin{aligned}
\mathbf{J}_n\dot{\boldsymbol{\omega}}_n^t + \boldsymbol{\omega}_n^t \times \mathbf{J}_n\boldsymbol{\omega}_n^t =& (\tilde{\mathbf{r}}_{n-1} - \mathbf{r}_n) \times (\mathbf{N}_{n-1} + \mathbf{F}_{fn-1}) + (\bar{\mathbf{r}}_{n-1} - \mathbf{r}_n) \times \mathbf{F}_{cn-1} \\
&+ (\mathbf{r}_{n,n} - \mathbf{r}_n) \times \mathbf{F}_{top} + \mathbf{M}_{top}.
\end{aligned} \tag{5.148}$$

Using the above listed definitions, one can readily establish the equations of motion for any basic type of MSFP.

5.4 Analysis of the Triple Friction Pendulum Model

In order to test the effectiveness of this model for MSFPs, the analysis will focus on the TFP as there are many experimental and theoretical results for that system [7, 25, 26, 53]. Due to the non-linearity of the equations of motion for the TFP – Eqs. (5.110)-(5.117) – an iterative solver must be utilized to solve for the unknowns shown in Eq. (5.119). In this chapter, Newton's method is used to solve for the unknowns. Once the system unknowns have been determined, a system of ODEs has to be solved to get the time-history of the TFP. The time integrator used for all of the analysis will be that of the Dormand-Prince method, which is a type of Runge-Kutta ODE solver [15]. All of the physical quantities used for the following analysis can be found in Appendix E. For all the following simulations, a ground motion will be prescribed for the bottom bearing and a normal force, a restoring force and a restoring moment will be applied to the top bearing unless otherwise stated.

Uni-directional Ground Motions

For the uni-directional ground motions, a model based on the one used by Fenz and Constantinou [25] will be used and all of the physical data can be found in Appendix E.1. For the standard models of TFPs – $R_1 = R_4 > R_2 = R_3$, $\mu_2 = \mu_3 < \mu_1 < \mu_4$ – it has been well established that there are five stages to the motion [7, 25, 26, 53] when there is a ground motion in only one direction:

Stage I: There is motion only on surfaces 2 and 3.

Stage II: Motion on surface 2 stops and begins on surface 1, thus all motion is on surfaces 1 and 3.

Stage III: Motion on surface 3 stops and begins on surface 4, thus all motion is on surfaces 1 and 4.

Stage IV: The sliding capacity of surface 1 is reached and sliding begins on surface 2, thus all motion is on surfaces 2 and 4.

Stage V: The sliding capacity of surface 4 is reached and sliding begins on surface 3, thus all motion is on surfaces 3 and 4. This stage ends when the sliding capacities of both surfaces 2 and 3 are reached.

By running the kinetic model with a uni-directional motion – $u_{g1} = 0.05t^2$ m and all other prescribed motions set to zero – and imposing a restoring force and moment on the top bearing, this five stage behavior is recreated, as seen in Fig. 5.5, where $\frac{F_{top}}{N}$ is the restoring force on the top bearing, F_{top}, normalized to the applied normal force, N. Note that the relative angle between bearings is defined as $\delta_\gamma = \cos^{-1}\left(\cos(\psi_{\gamma+1})\cos(\theta_{\gamma+1})\right)$.

In order to test the hysteresis in this model, a uni-directional periodic ground motion – $u_{g1} = A\cos(2\pi ft)$ m – is applied to the system. The same tests as those used in [25] for the standard TFP will be used in this section, which will allow for a direct comparison of results. Table 5.1 shows the list of tests. The force-displacement curves are shown in

Test #	N, (kN)	f, (Hz)	A, (mm)
1	112	0.10	1.2
2	112	0.04	25
3	112	0.013	75
4	112	0.0088	115
5	112	0.0072	140

Table 5.1 Tests used for uni-directional ground motions.
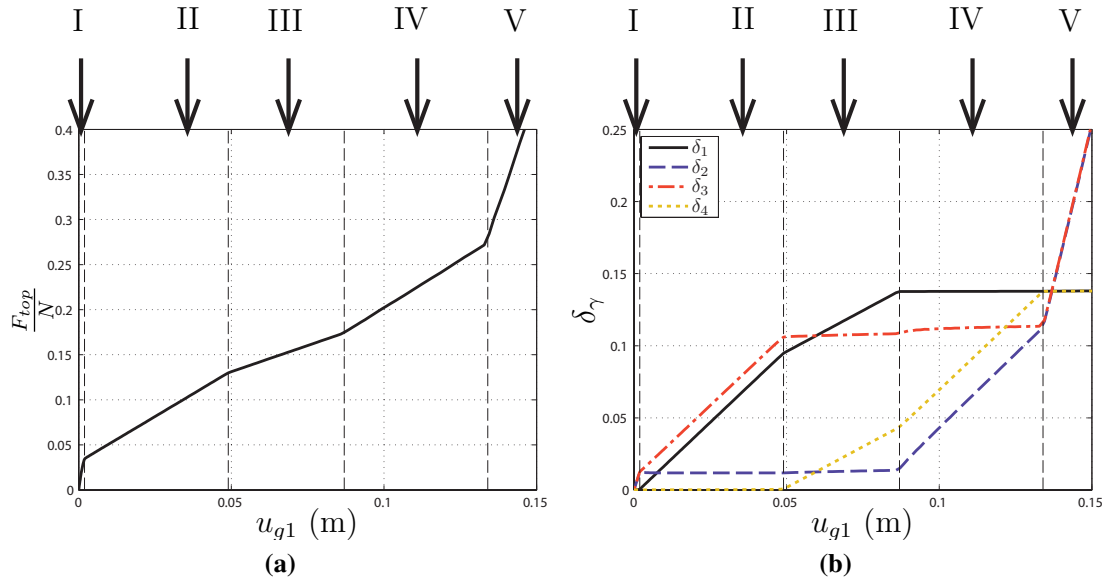
Fig. 5.5 (a) Force/displacement curve for the TFP for a uni-directional motion.
(b) Relative angle of each bearing for a uni-directional motion.

Fig. 5.6, and by comparing them to similar figures in [25, 26], it can be seen that the kinetic model has the appropriate hysteresis behavior. For the analytical models developed in [25],
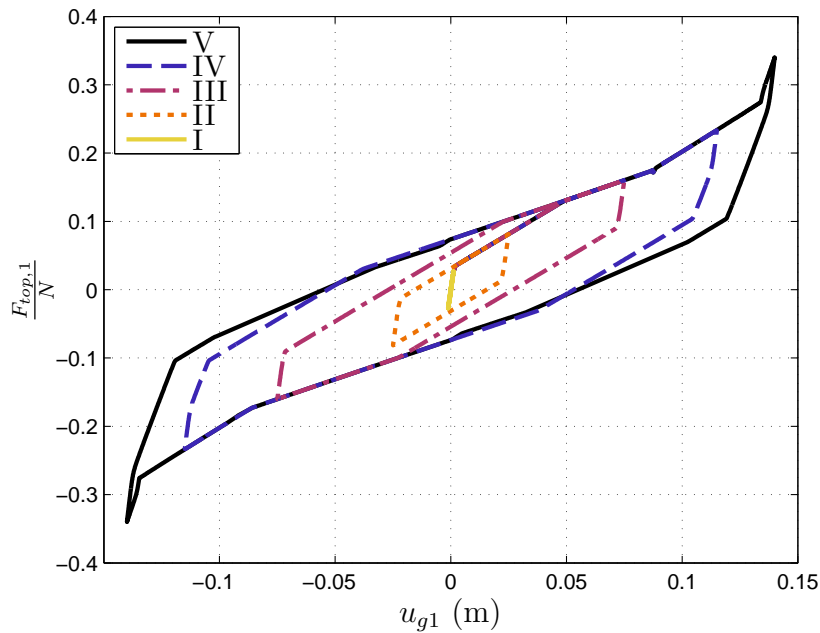
Fig. 5.6 Hysteresis loop for uni-directional motions for ground motions in the five stages of motion.

they note that their forces on the top bearing when the first and fourth sliding surfaces reach their limits – F_{dr1} and F_{dr4} – underestimate the force recorded from the experiment. The values for u^*, u^{**}, u_{dr1}, u_{dr4}, F_{dr1} and F_{dr4} are shown in Table 5.2, where u^* is the displacement at which the TFP transitions from Stage I to Stage II, u^{**} is the displacement at which the TFP transitions from Stage II to Stage III, u_{dr1} is the displacement at which the TFP transitions from Stage III to Stage IV, u_{dr4} is the displacement at which the TFP transitions from Stage IV to Stage V, F_{dr1} is the force at which the TFP transitions from Stage III to Stage IV, and F_{dr4} is the force at which the TFP transitions from Stage IV to Stage V [26]. From Table 5.2 it can be seen that the kinetic model matches all of these values fairly well, and the kinetic model actually slightly overestimates F_{dr1} and F_{dr4}, yet are still much closer to the experimental values than the analytical values. The

	Analytical[†]	Experimental[†]	Kinetic Model
u^* (mm)	0.1	2	1.9
u^{**} (mm)	38.4	42	49
u_{dr1} (mm)	92.1	90	87
u_{dr4} (mm)	130.4	130	134
$\frac{F_{dr1}}{N}$	0.161	0.173	0.175
$\frac{F_{dr4}}{N}$	0.240	0.272	0.275

[†] Analytical and Experimental values come from the Regime V Data from [25].

Table 5.2 Comparison of Analytical Model, Experimental, and Kinetic Model values.

overestimation of F_{dr4} is most likely due to using a constant set of μ_γ values as opposed to changing the friction coefficients with different stages. Thus, it is shown that for larger displacements the kinetic model can more accurately predict the response of an actual TFP, which is due to the fact that there is no linearization approximation, which becomes less accurate as the amplitude of motion increases.

For all of the previous tests, a normal force of $N = 112$ kN was used. However, it is useful to see how changing N affects the dynamic response of the TFP, as this will give a sense of the inertial effects of the model. To do this, the variance between two tests will be measured with an L^2-norm [36], given by

$$V(\eta) = \frac{\sqrt{\int_0^{u_{max}} \|\mathbf{d} - \mathbf{d}_{ref}\|^2}}{\sqrt{\int_0^{u_{max}} \|\mathbf{d}_{ref}\|^2}}, \tag{5.149}$$

where $V(\eta)$ is the variance as a function of η, η is the ratio of the applied normal force to the weight of the TFP, W, excluding the bottom bearing, u_{max} is the maximum applied

ground displacement, and **d** is given as

$$[\mathbf{d}] = \begin{bmatrix} \delta_1 & \delta_2 & \delta_3 & \delta_4 \end{bmatrix}^T, \tag{5.150}$$

and $\mathbf{d}_{ref}$ is the test with the largest normal force, N_{max}, to which all other tests will be compared. For this chapter, $N_{max} = 1$ MN and $W = 90.64$ N. Note that $\| \bullet \|$ is the standard 2-norm.
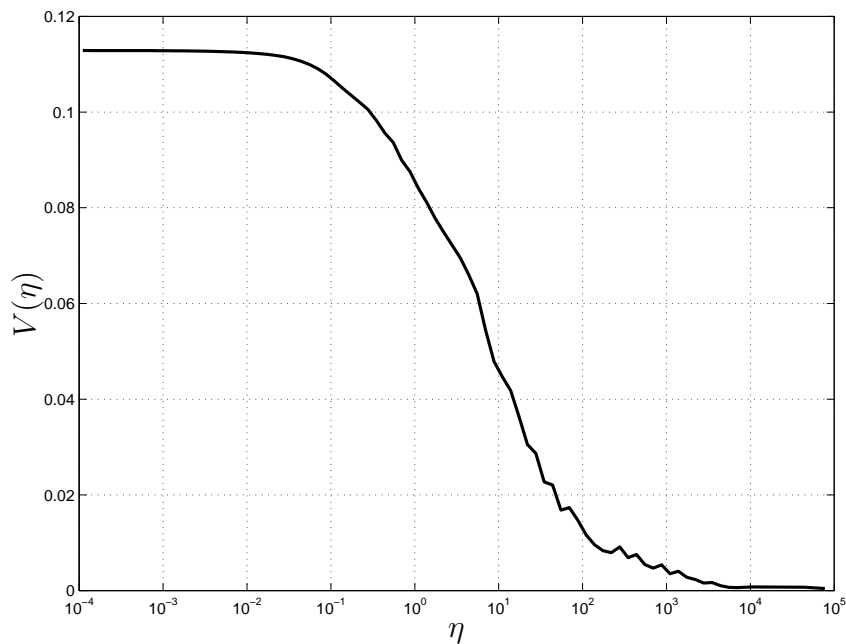
Fig. 5.7   The variance between two tests as a function of η on a semi-log scale.

The variance $V(\eta)$ is shown in Fig. 5.7, in which it can be seen that the variance is very small for large values of η, but as η decreases, the variance increases until it reaches a steady state around $\eta = 10^{-2}$. Typically values for η will be very large in practice, meaning that the inertial effects can be neglected. However, in the event of uplift [54], part of the TFP will be experiencing no normal force or $N = \eta = 0$, and from Fig. 5.7 it can be seen in that scenario the inertial effects play a major role.

Uni-directional Ground Motions for Unusual TFP Properties

Another utility of the model presented in this chapter is the lack of assumptions used to develop the model. This allows for a new and unique TFP to be analyzed by this model. For example, the unusual TFP described in [53] has $\mu_2 = \mu_3 > \mu_1 = \mu_4$. While a TFP with this property can not be analyzed properly by the models presented by Fenz and Constantinou [26] or that of Becker and Mahin [7], it can be analyzed by the nonlinear kinetic model. Using the same physical properties described in Appendix E.1, except that $\mu_1 = \mu_4 = 0.064$

and $\mu_2 = \mu_3 = 0.168$, the kinetic model can be tested against the results found by Sarlis and Constantinou [53] by applying a uni-directional ground motion of $u_{g1} = A\cos(2\pi ft)$, where $A = 0.14$ m and $f = 0.02$ Hz. Figure 5.8 shows the force/displacement curve for the unusual TFP. By comparing Fig. 5.8 to similar figures in [53], it can be seen that the kinetic model accurately models the behavior of the unusual TFP.
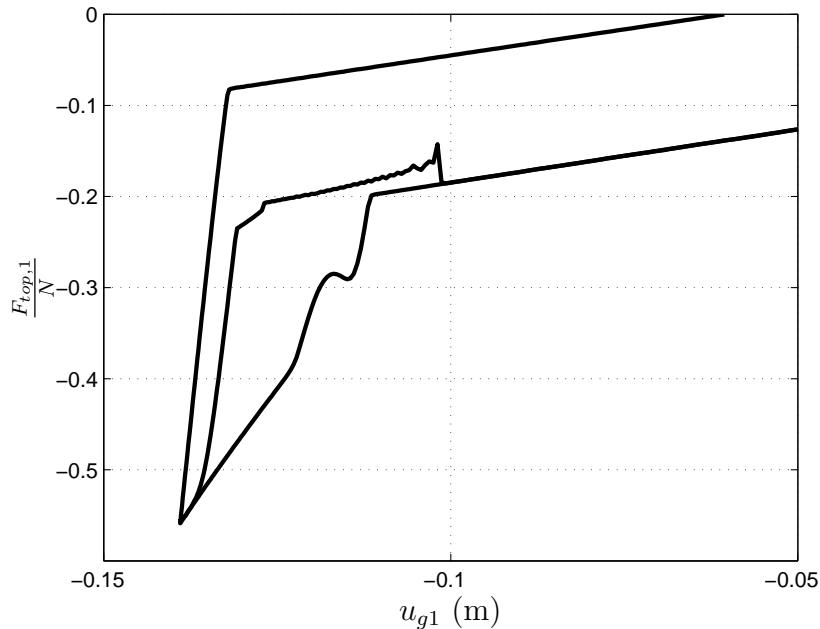
Fig. 5.8 Force/displacement curve for the unusual TFP.

Bi-Directional Ground Motions

Next, the kinetic model is tested with bi-directional ground motions. In the case of bi-directional ground motions, a model based on the one used by Becker and Mahin [7] is used and all of the necessary physical data can be found in Appendix E.2. The first test is a circular ground motion: $u_{g1} = A\cos(\Omega t)$ and $u_{g2} = A\sin(\Omega t)$ and all other prescribed motions set to zero. For the circular ground motion tests, $\Omega = 0.1$ rad/s is used, along with six values for A: $A = 0.12, 0.1, 0.07, 0.04, 0.01, 0.007$. This gives a basic ground motion to make sure that the kinetic model has the proper hysteresis loops as the bearings move in two directions. Figure 5.9 shows the hysteresis loops for both the $\mathbf{E}_1$ and $\mathbf{E}_2$ directions as well as the force curves on the top bearing when a circular ground motion is applied. By comparing these curves to similar ones by Becker and Mahin [7], it can be seen that the kinetic model is acting appropriately for a simple bi-directional ground motion. Next, a more complicated ground motion, that of a figure-eight, is applied: $u_{g1} = A\sin(\Omega t)$ and $u_{g2} = A\sin(2\Omega t)$ and all other prescribed motions set to zero. Again, $\Omega = 0.1$ is used, along with the same six values of A as for the circular motion: $A = 0.12, 0.1, 0.07, 0.04, 0.01, 0.007$. Figure 5.10
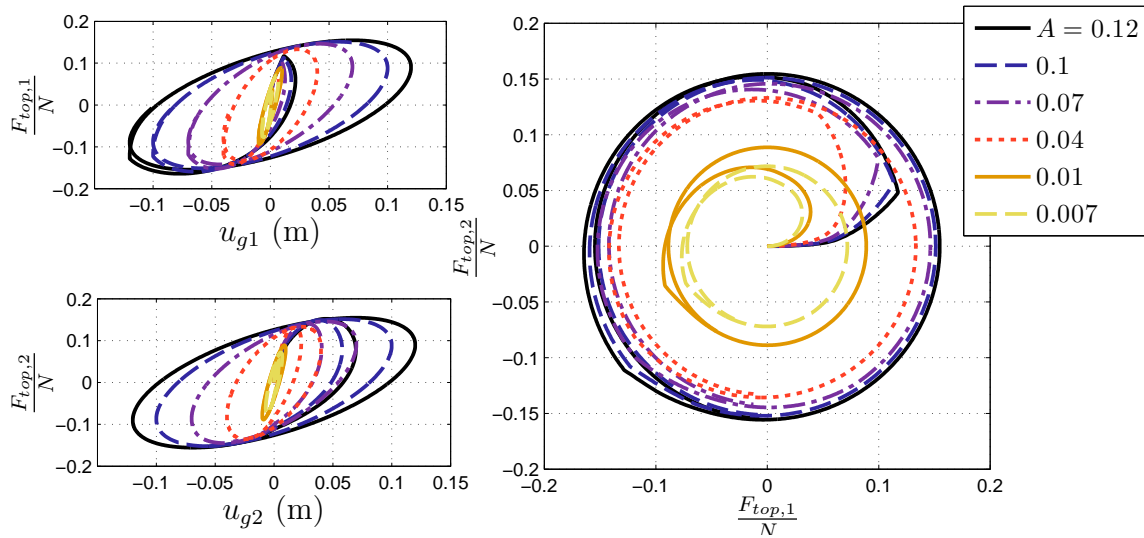
Fig. 5.9 Hysteresis loops and force curves for a circular ground motion.

shows the hysteresis loops for both the $\mathbf{E}_1$ and $\mathbf{E}_2$ directions as well as the force curves on the top bearing when a figure-eight ground motion is applied. By comparing the curves in Fig. 5.10 to similar curves by Becker and Mahin [7], it can be seen that the kinetic model is accurately predicting the behavior of the TFP for this complicated ground motion.
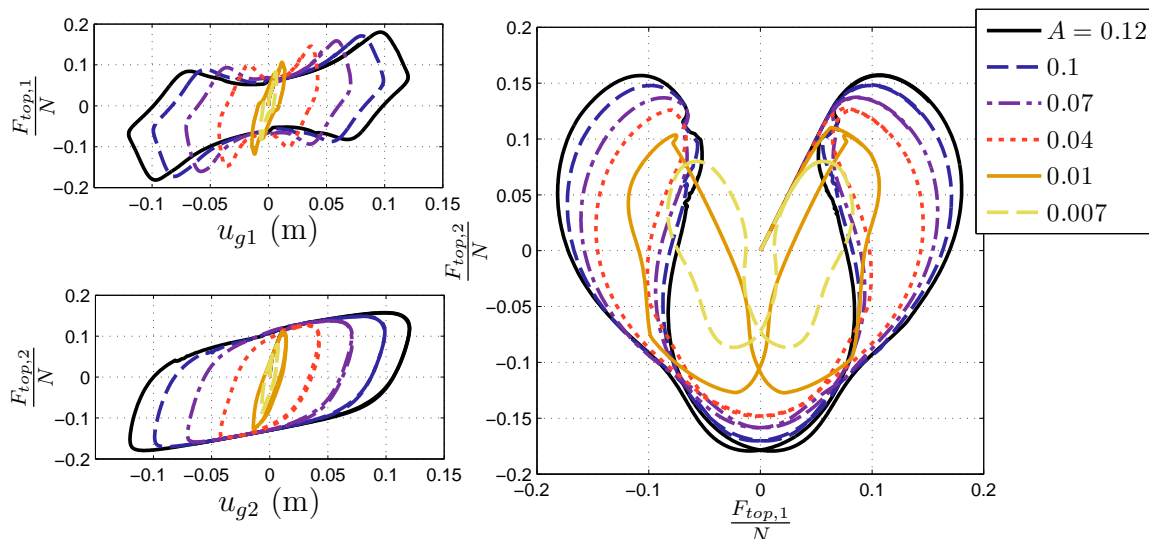
Fig. 5.10 Hysteresis loops and force curves for a figure-eight ground motion.

5.5 Conclusions and Future Work

While there have been other kinetic models [53], those kinetic models linearize the TFP which reduces the accuracy for larger displacements. They can also only handle uni-directional ground motions, which means they can not account for the more complicated bi-directional ground motions. Meanwhile, there are models that can handle bi-directional ground motion [7]. Again, they linearize the model and, as shown in [54], they lack the capability to handle non-standard TFP bearings. The model presented in this chapter, as shown in the previous section, can work for both uni-directional and bi-directional ground motions with no linearization assumption. For that reason, in the case of uni-directional ground motions, it was shown that the nonlinear model can more accurately predict the experimental values than previous analytical models. The only assumption that the nonlinear kinetic model makes is that the bearings are axisymmetric. Thus, this model can be used to analyze the simplest, as well as the more complicated ground motions that one would like to test. While not specifically analyzed in this chapter, the nonlinear kinetic model can handle initial rotations of the top and bottom bearings, similar to that described in [6].

The nonlinear kinetic model has the capability to be connected numerically to models of different superstructures, such as frames, trusses, or any type of finite element model. This allows one to model an entire system, including the TFP, in one complete simulation, while accounting for the non-linear and inertial nature of the TFP.

However, this model is far from complete. For instance, only constant values of the friction coefficients, μ_γ, were used while it has been shown that these values are dependent on multiple factors, such as speed, temperature, and pressure [37]. Implementing these more complicated friction coefficients is a straight forward process that can be added to this model. The nonlinear kinetic model does not account for uplift or tilting of bearings, yet that behavior has been shown to occur in TFP experiments [54]. However, this model can be equipped to handle uplift or tilting by adding the necessary degrees of freedom to Eq. (5.119). It was also shown that the inertial effects of the bearing will have a major role in the event of uplift, thus starting from a model that already incorporates inertia will make handling uplift less complicated.

Finally, all of the previous analyses can be conducted with any type of MSFP by the method presented earlier in this chapter, allowing for more complicated testing of different types of Friction Pendulum seismic isolators.

For all of the reasons previously stated, the model presented in this chapter is an all-in-one model that is the most capable and accurate model for MSFPs available and can be easily updated to handle different types of friction models as well as extra forces that may be applied to the internal bearings.

Chapter 6

Concluding Remarks

6.1 Summary of Results

The field of structural mechanics progresses every day, but it needs to progress equally in all facets: experiments, modeling and theoretical analysis. However, in the fields of hybrid simulation and multi-slider friction bearings, the modeling and theoretical analysis has lagged behind the advances made by experimentation, thus leading to the need for the work presented in this dissertation.

This dissertation developed novel approaches to the theoretical analysis of hybrid simulation. Specifically, it was shown that there are limitations and constraints that occur naturally from applying a hybrid split to a mechanical system including large errors around the natural frequencies of the reference system and how better controllers may not necessarily produce better results. These limitations and constraints are present in all of the test cases presented in this dissertation, from the simple linear model, all the way to the nonlinear multi-degree of freedom system. The fact that similar results show up for these vastly different systems, even when the system exhibits chaotic behavior, shows that there is a fundamental effect that a hybrid split has a dynamical system. The L^2 norm was utilized in all three test cases to understand the error present in hybrid simulation, which allows for easy comparison between all of the results, excluding, of course, the case of chaotic behavior. Thus, understanding those effects plays a critical role in how one creates a hybrid simulation experiment in an attempt to reduce any errors, as well as how one analyses the results of a hybrid simulation experiment knowing that errors will be present. For instance, the likelihood of ever achieving a perfect dynamical response from a hybrid system is not very good, however, the fundamental aspects of the dynamics are preserved if appropriate care is taken when preforming a hybrid simulation experiment.

An advanced model for a MSFP was also presented in this dissertation. The model started from existing models and incorporated those features as well as new and unique features to create this advanced model. Namely, this model incorporates inertial effects, bi-directional ground motions, and nonlinear internal motions to create this all-in-one model. It was shown that, due to the lack of assumptions while constructing the model, it can

handle all of the current modeling needs out there, and can, in some cases, be even more accurate than current models, thus demonstrating its utility.

6.2 Future Work

While this dissertation provided new and interesting insights into the modeling and analysis of hybrid simulation and MSFPs, there exist more research aspects that can be considered. For instance, the models for hybrid simulation all utilized either constant errors or simply PI controllers for the error model. There are better control systems out there in the literature which may provide more insight into the effect of the control scheme on the dynamical response of a hybrid system. Also, even though a multi-degree of freedom model was used in this dissertation, it still only had twelve degrees of freedom, where many hybrid simulation experiments can have orders of magnitude more degrees of freedom. Similarly, the most hybrid splits any one system had in this dissertation was two, whereas one could foresee a need for many more hybrid splits. Understanding how the error is affected by more hybrid splits would also be invaluable. As for the MSFPs, the model shown here does not incorporate uplift conditions between bearings, which is a well documented phenomenon in experimental tests. Thus, it would be beneficial to incorporate uplift conditions, as well as tilting of the bearings, into the model. While the model presented in this dissertation utilized constant values for the friction coefficient, there are models with representations of the friction coefficient that depend on the speed, temperature, and pressure at the contact interfaces. Finally, implementation of the MSFP model in computational platforms, such as OpenSees, would also be a beneficial task.

References

[1]   M. Ahmadizadeh, G. Mosqueda, and A. M. Reinhorn. "Compensation of actuator delay and dynamics for real time hybrid structural simulation". In: *Earthquake Engineering and Structural Dynamics* 37.1 (2008), pp. 21–42.

[2]   G. L. Baker and J. A. Blackburn. *The Pendulum: A Case Study in Physics*. New York: Oxford University Press, 2005.

[3]   G. L. Baker and J. P. Gollub. *Chaotic Dynamics: An Introduction*. New York: Cambridge University Press, 1996.

[4]   A. A. Bakhaty, S. Govindjee, and K. M. Mosalam. "Theoretical evaluation of hybrid simulation applied to continuous plate structures)". In: *Journal of Engineering Mechanics* 142.12 (2016), p. 04016093.

[5]   T. C. Becker and S. A. Mahin. "Correct treatment of rotation of sliding surfaces in a kinematic model of the triple friction pendulum bearing". In: *Earthquake Engineering & Structural Dynamics* 42.2 (2013), pp. 311–317.

[6]   T. C. Becker and S. A. Mahin. "Effect of support rotation on triple friction pendulum bearing behavior". In: *Earthquake Engineering & Structural Dynamics* 42.12 (2013), pp. 1731–1748.

[7]   T. C. Becker and S. A. Mahin. "Experimental and analytical study of the bi-directional behavior of the triple friction pendulum isolator". In: *Earthquake Engineering & Structural Dynamics* 41.3 (2012), pp. 355–373.

[8]   O. S. Bursi, C. Jia, L. Vulcan, S. A. Neild, and D. J. Wagg. "Rosenbrock-based algorithms and subcycling strategies for real-time nonlinear substructure testing". In: *Earthquake Engineering and Structural Dynamics* 40.1 (2011), pp. 1–19.

[9]   C. Chen and J. M. Ricles. "Tracking error-based servohydraulic actuator adaptive compensation for real-time hybrid simulation". In: *Journal of Structural Engineering* 136.4 (2010), pp. 432–440.

[10]   A. K. Chopra. *Dynamics of Structures: Theory and Applications to Earthquake Engineering*. Upper Saddle River, NJ: Prentice Hall., 2004.

[11] M. C. Constantinou, A. S. Whittaker, Y. Kalpakidis, D. M. Fenz, and G. P. Warn. *Performance of Seismic Isolation Hardware under Service and Seismic Loading*. Tech. rep. MCEER-07-0012. Buffalo, NY: Multidisciplinary Center for Earthquake Engineering Research, 2007.

[12] A. P. Darby, A. Blakeborough, and M. S. Williams. "Improved control algorithm for real-time substructure testing". In: *Earthquake Engineering and Structural Dynamics* 30.3 (2001), pp. 431–448.

[13] L. Dieci, M. S. Jolly, and E. S. Van Vleck. "Numerical techniques for approximating lyapunov exponents and their implementation". In: *Journal of Computational and Nonlinear Dynamics* 6.1 (2010), pp. 011003–011003–7.

[14] L. Dieci and E. S. Van Vleck. *Software: LESLIS/LESLIL and LESNLS/LESNLL*. http://www.math.gatech.edu/~dieci/software-les.html.

[15] J. R. Dormand and P. J. Prince. "A family of embedded Runge-Kutta formulae". In: *Journal of Computational and Applied Mathematics* 6.1 (1980), pp. 19 –26.

[16] N. E. Dowling. *Mechanical Behavior of Materials*. Upper Saddle River, NJ: Prentice Hall; 3rd Edition, 2007.

[17] P. L. Drazin. "Hybrid Simulation Theory Featuring Bars and Beams". M.S. report. Berkeley, CA: University of California, 2013.

[18] P. L. Drazin and S. Govindjee. "Hybrid simulation theory for a classical nonlinear dynamical system". In: *Journal of Sound and Vibration* 392 (2017), pp. 240 –259.

[19] P. L. Drazin and S. Govindjee. *Hybrid simulation theory for a crane structure*. Tech. rep. SEMM-2017/01. Berkeley, CA: Structural Engineering Mechanics and Materials, 2017.

[20] P. L. Drazin, S. Govindjee, and K. M. Mosalam. "Hybrid simulation theory for continuous beams". In: *ASCE Journal of Engineering Mechanics* 141.7 (2015), p. 04015005.

[21] *E-Defense*. www.bosai.go.jp/hyogo/ehyogo/profile/introduction/Introduction.html. [Online; accessed 08-June-2016].

[22] T. Elkhoraibi and K. M. Mosalam. "Towards error-free hybrid simulation using mixed variables". In: *Earthquake Engineering and Structural Dynamics* 36.11 (2007), pp. 1497–1522.

[23] F. Fadi and M. C. Constantinou. "Evaluation of simplified methods of analysis for structures with triple friction pendulum isolators". In: *Earthquake Engineering & Structural Dynamics* 39.1 (2010), pp. 5–22.

[24] D. M. Fenz and M. C. Constantinou. "Modeling triple friction pendulum bearings for response-history analysis". In: *Earthquake Spectra* 24.4 (2008), pp. 1011–1028.

[25] D. M. Fenz and M. C. Constantinou. "Spherical sliding isolation bearings with adaptive behavior: Experimental verification". In: *Earthquake Engineering & Structural Dynamics* 37.2 (2008), pp. 185–205.

[26] D. M. Fenz and M. C. Constantinou. "Spherical sliding isolation bearings with adaptive behavior: Theory". In: *Earthquake Engineering & Structural Dynamics* 37.2 (2008), pp. 163–183.

[27] J. Ferry. *Viscoelastic Properties of Polymers*. New York: John Wiley & Sons, 1970.

[28] P. Frederickson, J. L. Kaplan, E. D. Yorke, and J. A. Yorke. "The Liapunov dimension of strange attractors". In: *Journal of Differential Equations* 49.2 (1983), pp. 185 –207.

[29] R. Gilmore and M. Lefranc. *The Topology of Chaos*. Weinheim, Germany: Wiley-VCH, 2011.

[30] P. Grassberger and I. Procaccia. "Characterization of strange attractors". In: *Physical Review Letters* 50.5 (1983), pp. 346–349.

[31] P. Grassberger and I. Procaccia. "Measuring the strangeness of strange attractors". In: *Physica D: Nonlinear Phenomena* 9.1 (1983), pp. 189 –208.

[32] J. Guckenheimer and P. Holmes. *Nonlinear Oscillations, Dynamical Systems, and Bifurcations of Vector Fields*. New York: Springer-Verlag, 1983.

[33] S. Günay and K. M. Mosalam. "Seismic performance evaluation of high voltage disconnect switches using real-time hybrid simulation: II. Parametric study". In: *Earthquake Engineering and Structural Dynamics* 43.8 (2014), pp. 1223–1237.

[34] P. S. Harvey and H. P. Gavin. "Truly isotropic biaxial hysteresis with arbitrary knee sharpness". In: *Earthquake Engineering & Structural Dynamics* 43.13 (2014), pp. 2051–2057.

[35] B. Jerman, P. Podraj, and J. Kramar. "An investigation of slewing-crane dynamics during slewing motiondevelopment and verification of a mathematical model". In: *International Journal of Mechanical Sciences* 46.5 (2004), pp. 729 –750.

[36] C. Johnson. *Numerical Solution of Partial Differential Equations by the Finite Element Method*. Mineola, NY: Dover Publications, 2009.

[37] M. Kumar, A. S. Whittaker, and M. C. Constantinou. "Characterizing friction in sliding isolation bearings". In: *Earthquake Engineering & Structural Dynamics* 44.9 (2015), pp. 1409–1425.

[38] W. S. M. Lau and K. H. Low. "Motion analysis of a suspended mass attached to a crane". In: *Computers & Structures* 52.1 (1994), pp. 169 –178.

[39] S. A. Mahin and M. E. William. "Computer controlled seismic performance testing". In: *Dynamic Respone of Structures: Experimentation, Observation, Prediction and Control* American Society of Civil Engineers (1980).

[40] D. P. McCrum and M. S. Williams. "An overview of seismic hybrid testing of engineering structures". In: *Engineering Structures* 118 (2016), pp. 240 –261.

[41] A. S. Mokha, A. Navinchandra, M. C. Constantinou, and V. Zayas. "Seismic isolation retrofit of large historic building". In: *Journal of Structural Engineering* 122.3 (1996), pp. 298–308.

[42] T. A. Morgan and S. A. Mahin. "Achieving reliable seismic performance enhancement using multi-stage friction pendulum isolators". In: *Earthquake Engineering & Structural Dynamics* 39.13 (2010), pp. 1443–1461.

[43] K. M. Mosalam and S. Günay. "Seismic performance evaluation of high voltage disconnect switches using real-time hybrid simulation: I. System development and validation". In: *Earthquake Engineering and Structural Dynamics* 43.8 (2014), pp. 1205–1222.

[44] K. M. Mosalam, R. N. White, and G. Ayala. "Response of infilled frames using pseudo-dynamic experimentation". In: *Earthquake Engineering and Structural Dynamics* 27 (1998), pp. 589–608.

[45] G. Mosqueda, A. S. Whittaker, and G. L. Fenves. "Characterization and modeling of friction pendulum bearings subjected to multiple components of excitation". In: *Journal of Structural Engineering* 130.3 (2004), pp. 433–442.

[46] A. H. Nayfeh and B. Balachandran. *Applied Nonlinear Dynamics*. New York: John Wiley & Sons, 1995.

[47] N. S. Nise. *Control Systems Engineering*. New York: John Wiley & Sons, 2008.

[48] O. M. O'Reilly. *Intermediate Dynamics for Engineers*. New York: Cambridge University Press, 2008.

[49] Y. J. Park, Y. K. Went, and A. H-S. Ang. "Random vibration of hysteretic systems under bi-directional ground motions". In: *Earthquake Engineering & Structural Dynamics* 14.4 (1986), pp. 543–557.

[50] T. S. Parker and L. O. Chua. *Practical Numerical Algorithms for Chaotic Systems*. New York: Springer-Verlag, 1989.

[51] B. Posiadaa. "Influence of crane support system on motion of the lifted load". In: *Mechanism and Machine Theory* 32.1 (1997), pp. 9 –20.

[52] S. S. Rao. *Mechanical Vibrations*. Upper Saddle River, NJ: Prentice Hall, 2004.

[53] A. A. Sarlis and M. C. Constantinou. "A model of triple friction pendulum bearing for general geometric and frictional parameters". In: *Earthquake Engineering & Structural Dynamics* 45.11 (2016), pp. 1837–1853. ISSN: 1096-9845.

[54] A. A. Sarlis and M. C. Constantinou. *Model of triple friction pendulum isolators for general geometric and frictional parameters and for uplift conditions*. Tech. rep. MCEER-13-0010. Buffalo, NY: Multidisciplinary Center for Earthquake Engineering Research, 2013.

[55] A. H. Schellenberg. "Advanced implementation of hybrid simulation". PhD thesis. Berkeley, CA: University of California, 2008. 348 pp.

[56] P. S. B. Shing and S. A. Mahin. "Elimination of spurious higher-mode response in pseudodynamic tests". In: *Earthquake Engineering and Structural Dynamics* 15.4 (1987), pp. 409–424.

[57] P. S. B. Shing and S. A. Mahin. *Pseudodynamic test method for seismic perfor-mance evaluation: theory and implementation.* Tech. rep. UCB-EERC-84-01. Berke-ley, CA: Earthquake Engineering Research Center, 1984.

[58] S. H. Strogatz. *Nonlinear Dynamics and Chaos*. Perseus Books, 1994.

[59] K. Takanashi and M. Nakashima. "Japanese activities on on-line testing". In: *Journal of Engineering Mechanics* 113.7 (1987), pp. 1014–1032.

[60] K. Takanashi, K. Udagawa, M. Seki, T. Oakada, and H. Tanaka. "Nonlinear earth-quake response analysis of structures by a com-puter-actuator on-line system". In: *Bulletin of Earthquake Resistant Structure Research Center* 8 (1975).

[61] N. Terkovics, S. A. Neild, M. Lowenberg, R. Szalai, and B. Krauskopf. "Substruc-turability: the effect of interface location on a real-time dynamic substructuring test". In: *Proceedings of the Royal Society of London A: Mathematical, Physical and En-gineering Sciences* 472.2192 (2016).

[62] B. H. Tongue. *Principles of Vibration*. New York: Oxford University Press, 2002.

[63] C. S. Tsai, Y. C. Lin, and H. C. Su. "Characterization and modeling of multiple fric-tion pendulum isolation system with numerous sliding interfaces". In: *Earthquake Engineering & Structural Dynamics* 39.13 (2010), pp. 1463–1491.

[64] N. W. Tschoegl. *The Phenomenological Theory of Linear Viscoelastic Behavior*. Berlin: Springer-Verlag, 1989.

[65] M. Verma and J. Rajasankar. "Improved model for real-time substructuring testing system". In: *Engineering Structures* 41 (2012), pp. 258 –269.

[66] S. N. Voormeeren, D. de Klerk, and D. J. Rixen. "Uncertainty quantification in exper-imental frequency based substructuring". In: *Mechanical Systems and Signal Pro-cessing* 24.1 (2010), pp. 106–118.

[67] D. Wagg, S. Neild, and P. Gawthrop. "Real-time testing with dynamic substructur-ing". In: *Modern Testing Techniques for Structural Systems: Dynamics and Control*. Ed. by O. S. Bursi and D. Wagg. Vienna: Springer Vienna, 2008, pp. 293–342.

[68] G. P. Warn and K. L. Ryan. "A review of seismic isolation for buildings: Historical development and research needs". In: *Buildings* 2.4 (2012), 300325. ISSN: 2075-5309.

[69] M. S. Williams and A. Blakeborough. "Laboratory testing of structures under dy-namic loads: an introductory review". In: *Philosophical Transactions of the Royal Society of London A: Mathematical, Physical and Engineering Sciences* 359.1786 (2001), pp. 1651–1669.

[70] M. Zapateiro, H. R. Karimi, N. Luo, and B. F. Spencer. "Real-time hybrid testing of semiactive control strategies for vibration reduction in a structure with MR damper". In: *Structural Control and Health Monitoring* 17.4 (2010), pp. 427–451.

[71] V. Zayas, S. Low, and S. Mahin. *The FPS earthquake protection system: Experimental report*. Tech. rep. UCB/EERC-1987/01. Berkeley, CA: Earthquake Engineering Research Center, 1987.

[72] V. A. Zayas and S. S. Low. "Seismic isolation of bridges using friction pendulum bearings". In: *Structural Engineering in the 21st Century: Proc., 1999 Structures Congress*. (1999).

Appendix A

Beam Material Constants and Physical Parameters

For analysis of the pinned-pinned beam in Chapter 2, the beam is assumed to be a square steel beam with material constants and dimensions listed in Table A.1 [16].

E	E_0	E_∞	A	I	l	ρ	$\bar{M}$
$2 \times 10^{11} \ \frac{\text{N}}{\text{m}^2}$	$2 \times 10^{11} \ \frac{\text{N}}{\text{m}^2}$	$10^{11} \ \frac{\text{N}}{\text{m}^2}$	$0.04 \ \text{m}^2$	$\frac{A^2}{12} \ \text{m}^4$	$10 \ \text{m}$	$7800 \times A \ \frac{\text{kg}}{\text{m}}$	$10^4 \ \frac{\text{N}}{\text{m}^2}$

Table A.1 Material constants and dimensions used for fixed-free bar systems.

Appendix B

θ_p and $\dfrac{d\theta_p}{d\tau}$ Plots

In Chapter 3, the dynamical response of the $\mathcal{C}$ part of the hybrid system is consistently compared to the reference system. In this appendix, comparison plots using the dynamical response of the $\mathcal{P}$ part are provided. This is provided for completeness. All conclusions made from the plots in Chapter 3 remain true.
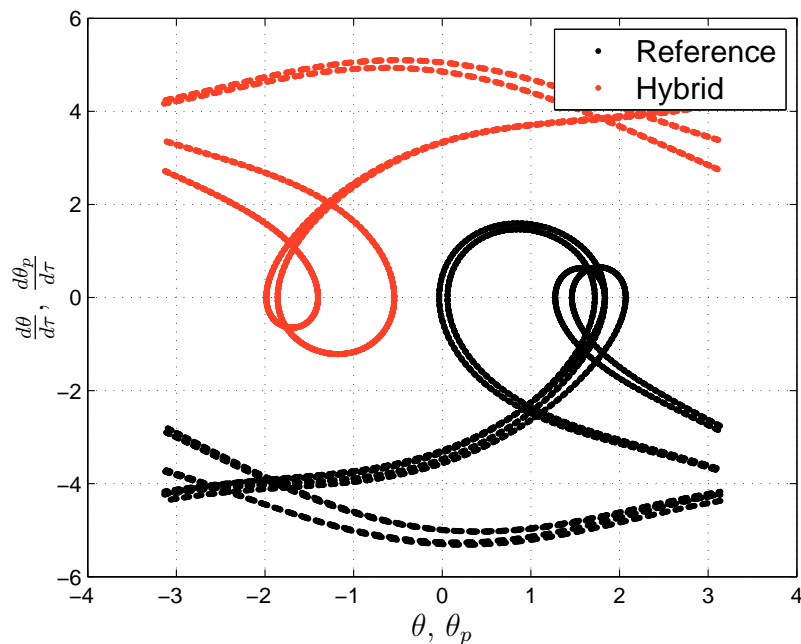
Fig. B.1 The state space trajectories for the reference and hybrid systems with $\bar{\mu} = 1.114$. Compare to Fig. 3.5.

Fig. B.2 The angular velocity time series of the reference and hybrid systems for $\bar{\mu} = 1.2$. Compare to Fig. 3.6.

Fig. B.3 A zoomed-in plot of the angular velocity time series of the reference and hybrid systems for $\bar{\mu} = 1.2$. Compare to Fig. 3.7.

Fig. B.4 The Poincaré sections of the reference and hybrid systems for $\bar{\mu} = 1.2$. Compare to Fig. 3.8.

Fig. B.5 The angular velocity time series of the reference and hybrid systems for $\bar{\mu} = 2.2$. Compare to Fig. 3.9.

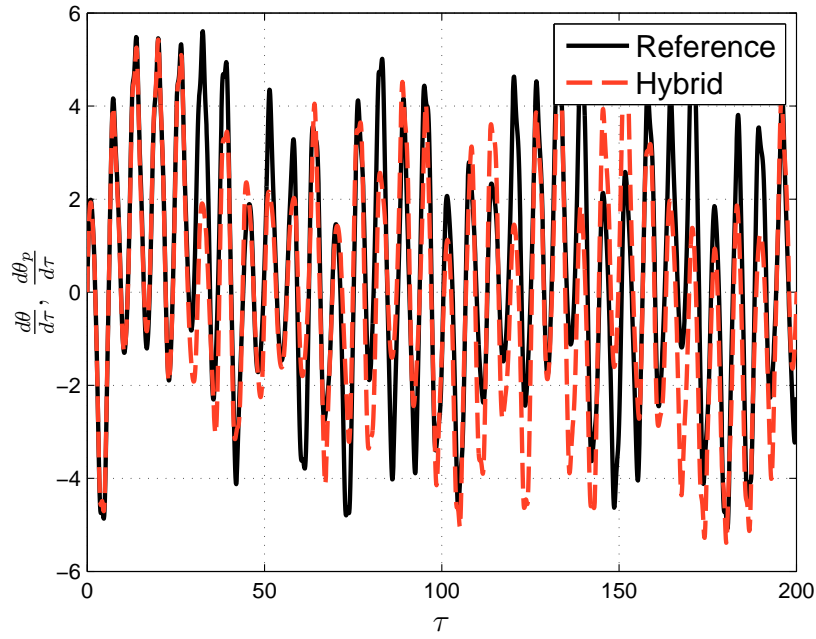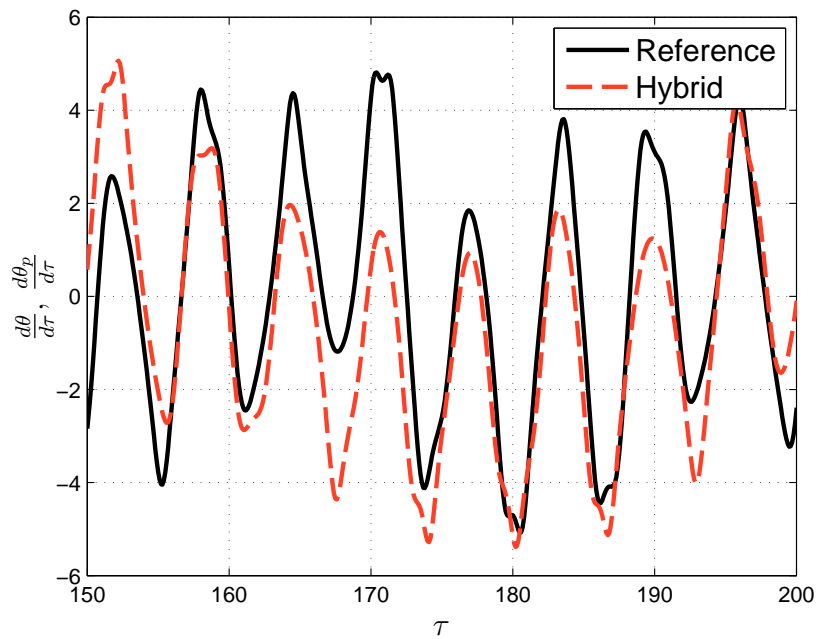**Fig. B.6** A zoomed-in plot of the angular velocity time series of the reference and hybrid systems for $\bar{\mu} = 2.2$. Compare to Fig. 3.10.
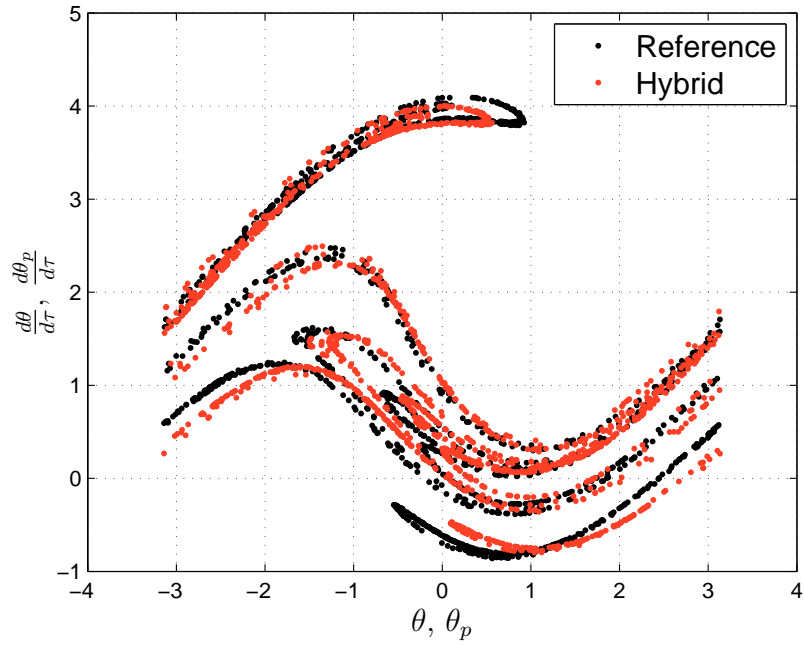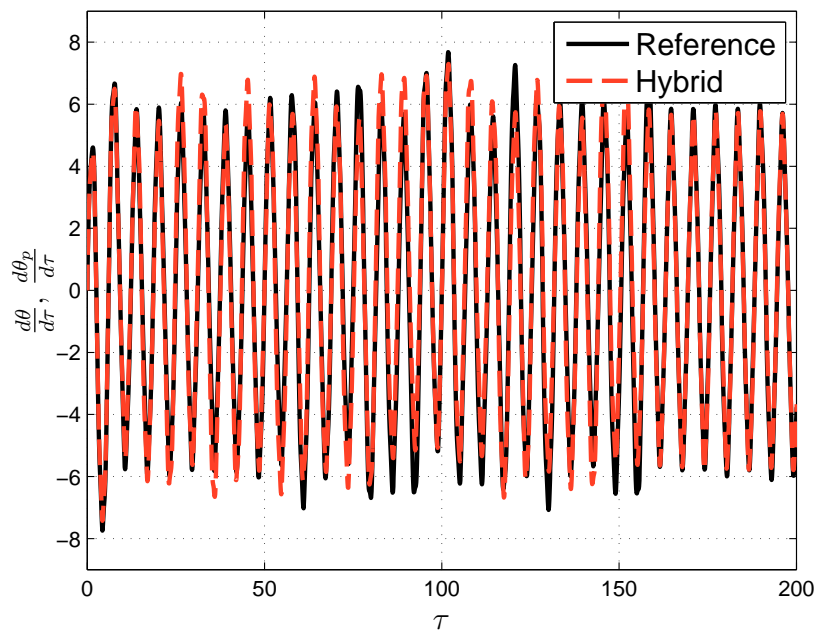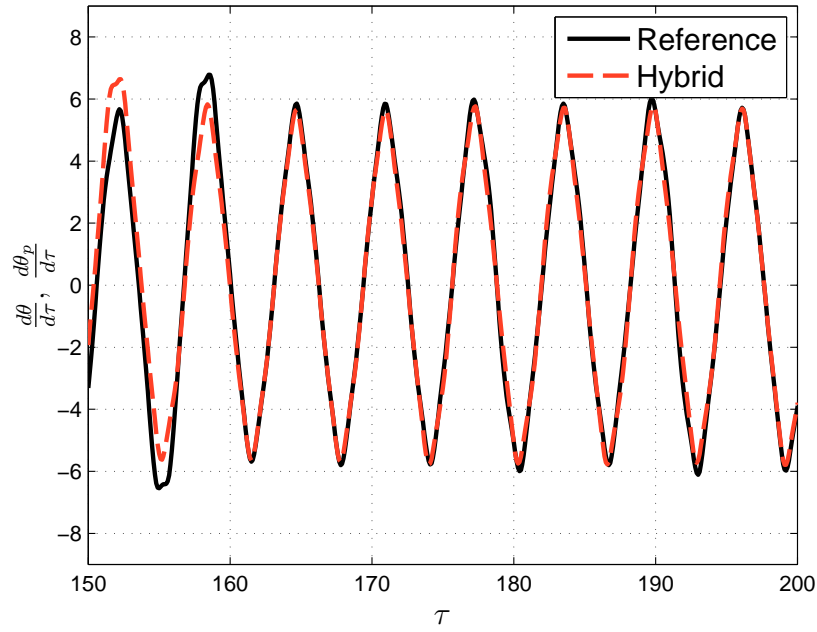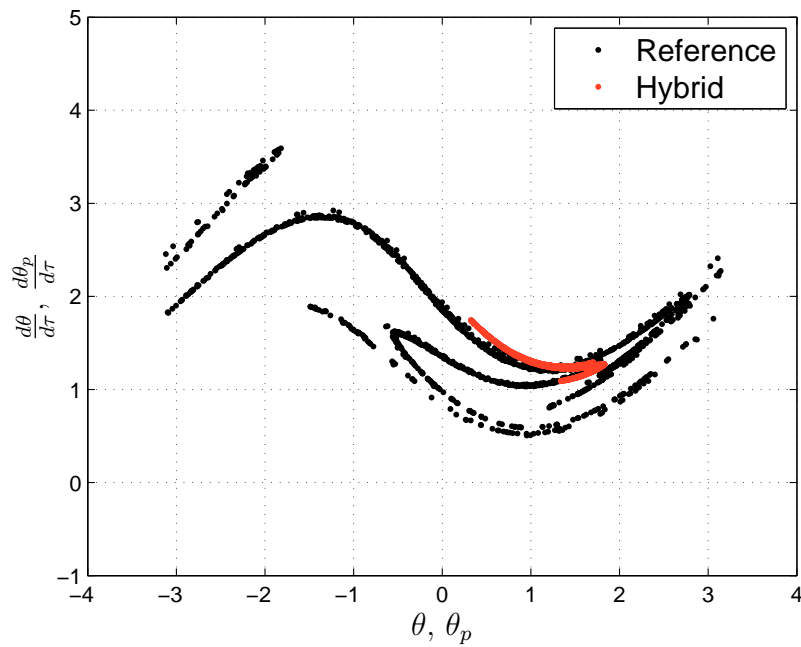

Fig. B.7 The Poincaré sections of the reference and hybrid systems for $\bar{\mu} = 2.2$. Compare to Fig. 3.11.
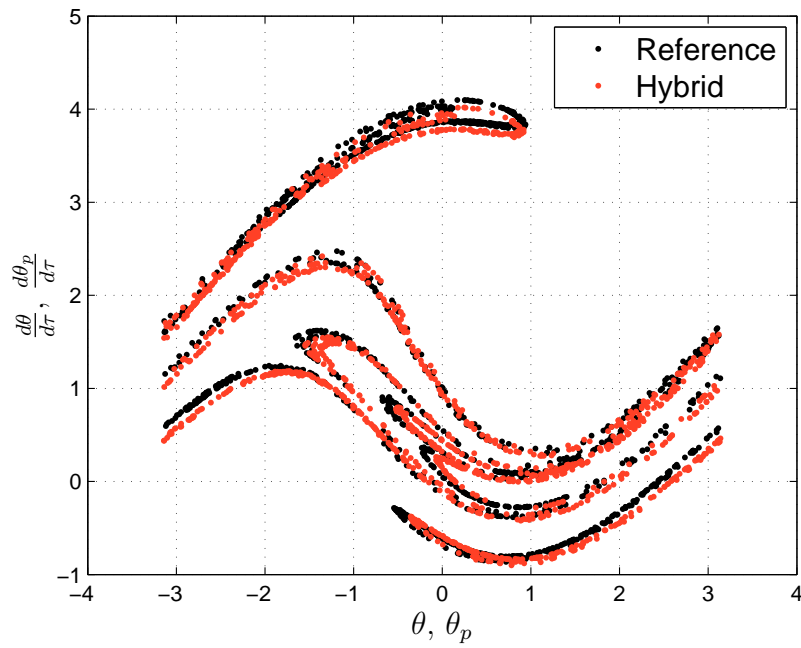
Fig. B.8 The Poincaré sections of the reference and hybrid systems for $\bar{\mu} = 1.2$ and $K_i = 10$. Compare to Fig. 3.18.

Physical Data for the Crane Structures

The following tables provide all of the numerical values used for the crane structures in Chapter 4, along with $g = 9.8$. All values were chosen in an attempt to approximate a scaled down crane structure and are considered dimensionless. Note, for the initial conditions used for time integration, all non-zero values are shown in Table C.5, with the exception of u_{g2}, whose definition is provided within Chapter 4.

ℓ_x	ℓ_y	ℓ_s	ℓ_r	ℓ_{ax}	ℓ_{az}	ℓ_b	ℓ_t	R_0
0.25	0.25	3	0.75	0.05	0.05	1	1	3

Table C.1   All lengths used for the crane systems.

$\mathbf{M}_j$	m_r	m_b	m_m	$\mathbf{J}_r$	$\mathbf{J}_b$
$\begin{bmatrix} 9.36 & 0 \\ 0 & 18.72 \end{bmatrix}_{\mathbf{E}_i \otimes \mathbf{E}_j}$	19.5	3.9	0.78	$\begin{bmatrix} 4.0625 & 0 & 0 \\ 0 & 4.0625 & 0 \\ 0 & 0 & 0.8125 \end{bmatrix}_{\mathbf{r}_i \otimes \mathbf{r}_j}$	$\begin{bmatrix} 0.0016 & 0 & 0 \\ 0 & 1.308 & 0 \\ 0 & 0 & 1.308 \end{bmatrix}_{\mathbf{b}_i \otimes \mathbf{b}_j}$

Table C.2   All masses and inertias used for the crane systems.

$\mathbf{K}_j$	k_b	k_m	$\mathbf{C}_j$	c_b	c_m
$\begin{bmatrix} 2023.3 & -2201.5 \\ -2201.5 & 4562.5 \end{bmatrix}_{\mathbf{E}_i \otimes \mathbf{E}_j}$	2.6×10^6	4.19×10^7	$\begin{bmatrix} 39.96 & -0.02 \\ -0.02 & 79.93 \end{bmatrix}_{\mathbf{E}_i \otimes \mathbf{E}_j}$	191.21	342.96

Table C.3   All stiffnesses and damping constants used for the crane systems.

m_a	c_a	k_a	k_p	k_i
1	156.5	245.25	10	55

Table C.4   All constants used for hybrid control.

R	ϕ	θ	α	β	u_{gx}
3	1.47	1.47	0.25	0.5	1

Table C.5   All non-zero initial conditions.

Appendix D

Error State Vectors

In order to define the error state vectors used in Chapter 4, let $\mathbf{a}_d$ be the vector of displacements, then

$$[\mathbf{a}_d] = \begin{bmatrix} R & \phi & \theta & \gamma & u_1 & u_2 & u_3 & u_4 & u_5 & u_6 & u_7 & u_8 \end{bmatrix}^T, \tag{D.1}$$

and equivalently for $\hat{\mathbf{a}}_d$, where all the quantities in Eq. (D.1) have the same meaning as in Section 4.2. And let $\mathbf{a}_v = \dot{\mathbf{a}}_d$, where the superposed dot ($\dot{\bullet}$)indicates a time derivative of the given quantity. Then,

$$[\mathbf{a}_s] = \begin{bmatrix} \mathbf{a}_d & \mathbf{a}_v \end{bmatrix}^T, \tag{D.2}$$

Similarly for $\hat{\mathbf{a}}_s$. Then, the total energy vectors are given as

$$[\mathbf{a}_E] = \begin{bmatrix} E \end{bmatrix}, \tag{D.3}$$

where $E = T + U$. See Section 4.2 for definitions of T and U. And equivalently for $\hat{\mathbf{a}}_E$. Finally, the vectors for δ, x, and y, are given by

$$[\mathbf{a}_\delta] = \begin{bmatrix} \delta & \dot{\delta} \end{bmatrix}^T, \; [\hat{\mathbf{a}}_{c\delta}] = \begin{bmatrix} \delta_c & \dot{\delta}_c \end{bmatrix}^T, \; [\hat{\mathbf{a}}_{p\delta}] = \begin{bmatrix} \delta_p & \dot{\delta}_p \end{bmatrix}^T, \tag{D.4}$$

$$[\mathbf{a}_x] = \begin{bmatrix} x_s & \dot{x}_s \end{bmatrix}^T, \; [\hat{\mathbf{a}}_{cx}] = \begin{bmatrix} x_{sc} & \dot{x}_{sc} \end{bmatrix}^T, \; [\hat{\mathbf{a}}_{px}] = \begin{bmatrix} x_{sp} & \dot{x}_{sp} \end{bmatrix}^T, \tag{D.5}$$

$$[\mathbf{a}_y] = \begin{bmatrix} y_s & \dot{y}_s \end{bmatrix}^T, \; [\hat{\mathbf{a}}_{cy}] = \begin{bmatrix} y_{sc} & \dot{y}_{sc} \end{bmatrix}^T, \; [\hat{\mathbf{a}}_{py}] = \begin{bmatrix} y_{sp} & \dot{y}_{sp} \end{bmatrix}^T, \tag{D.6}$$

where x_s, y_s, and δ are the $\mathbf{E}_1$ position, the $\mathbf{E}_2$ position, and rotation angle of the crane cabin for the reference system, x_{sc}, y_{sc}, and δ_c are the $\mathbf{E}_1$ position, the $\mathbf{E}_2$ position, and rotation angle of the crane cabin for the hybrid systems from the computational side, and x_{sp}, y_{sp}, and δ_p are the $\mathbf{E}_1$ position, the $\mathbf{E}_2$ position, and rotation angle of the crane cabin for the hybrid systems from the physical side.

Appendix E

Physical Data for the Triple Friction Pendulums

The following tables provide all of the numerical values used throughout Chapter 5, along with $g = 9.8$ m/s^2 .

E.1 Uni-directional Ground Motions

All values chosen for uni-directional ground motions were based on the data provided by Fenz and Constantinou [25] in order to allow for direct comparison of results.

R_1	R_2	R_3	R_4	R_0	r_2	r_3	r_4
0.473 m	0.076 m	0.076 m	0.473 m	5×10^{-5} m	0.051 m	0.0255 m	0.051 m
ℓ_1	ℓ_2	ℓ_3	ℓ_4	ℓ_5	p_2	p_3	p_4
0.013 m	0.015 m	0.046 m	0.015 m	0.013 m	0.0028 m	0.0044 m	0.0028 m
z_2	z_3	z_4	z_5	s_{c1}	s_{c2}	s_{c3}	s_{c4}
0.0075 m	0.023 m	0.0075 m	0.0065 m	0.065 m	0.0215 m	0.0215 m	0.065 m

Table E.1   All lengths used for uni-directional ground motions.

116

m_2	m_3	m_4	m_5
0.45 kg	0.34 kg	0.45 kg	8.0 kg

Table E.2   All masses used for uni-directional ground motions.

$\mathbf{J}_2$	$\mathbf{J}_3$
$\begin{bmatrix} 3.01 & 0 & 0 \\ 0 & 3.01 & 0 \\ 0 & 0 & 5.85 \end{bmatrix}_{\mathbf{t}_i^2 \otimes \mathbf{t}_j^2} \times 10^{-4} \ \mathrm{kg \cdot m^2}$	$\begin{bmatrix} 1.15 & 0 & 0 \\ 0 & 1.15 & 0 \\ 0 & 0 & 1.11 \end{bmatrix}_{\mathbf{t}_i^3 \otimes \mathbf{t}_j^3} \times 10^{-4} \ \mathrm{kg \cdot m^2}$
$\mathbf{J}_4$	$\mathbf{J}_5$
$\begin{bmatrix} 3.01 & 0 & 0 \\ 0 & 3.01 & 0 \\ 0 & 0 & 5.85 \end{bmatrix}_{\mathbf{t}_i^4 \otimes \mathbf{t}_j^4} \times 10^{-4} \ \mathrm{kg \cdot m^2}$	$\begin{bmatrix} 3.14 & 0 & 0 \\ 0 & 3.14 & 0 \\ 0 & 0 & 6.25 \end{bmatrix}_{\mathbf{t}_i^5 \otimes \mathbf{t}_j^5} \times 10^{-2} \ \mathrm{kg \cdot m^2}$

Table E.3   All inertias used for uni-directional ground motions.

$k_{c\gamma}$	k_{top}	$c_{c\gamma}$	c_{top}	μ_1	μ_2	μ_3	μ_4
10^7 N/m	10^6 N/m	5 N·s/m	5 N·s/m	0.03	0.017	0.017	0.107

Table E.4   All stiffnesses and damping constants used for uni-directional ground motions.

E.2 Bi-Directional Ground Motions

All values chosen for bi-directional ground motions were based on the data provided by Becker and Mahin [7] in order to allow for direct comparison of results.

R_1	R_2	R_3	R_4	R_0	r_2	r_3	r_4
0.9906 m	0.0762 m	0.0762 m	0.9906 m	5×10^{-5} m	0.0381 m	0.0191 m	0.0381 m
ℓ_1	ℓ_2	ℓ_3	ℓ_4	ℓ_5	p_2	p_3	p_4
0.011 m	0.0127 m	0.0254 m	0.0127 m	0.011 m	0.00073 m	0.0024 m	0.00073 m
z_2	z_3	z_4	z_5	s_{c1}	s_{c2}	s_{c3}	s_{c4}
0.0063 m	0.0127 m	0.0063 m	0.0055 m	0.0918 m	0.0135 m	0.0135 m	0.0918 m

Table E.5 All lengths used for bi-directional ground motions.

m_2	m_3	m_4	m_5
0.45 kg	0.34 kg	0.45 kg	8.0 kg

Table E.6 All masses used for bi-directional ground motions.

$\mathbf{J}_2$	$\mathbf{J}_3$
$\begin{bmatrix} 1.69 & 0 & 0 \\ 0 & 1.69 & 0 \\ 0 & 0 & 3.27 \end{bmatrix}_{\mathbf{t}_i^2 \otimes \mathbf{t}_j^2} \times 10^{-4}\ \mathrm{kg \cdot m^2}$	$\begin{bmatrix} 4.91 & 0 & 0 \\ 0 & 4.91 & 0 \\ 0 & 0 & 6.17 \end{bmatrix}_{\mathbf{t}_i^3 \otimes \mathbf{t}_j^3} \times 10^{-5}\ \mathrm{kg \cdot m^2}$
$\mathbf{J}_4$	$\mathbf{J}_5$
$\begin{bmatrix} 1.69 & 0 & 0 \\ 0 & 1.69 & 0 \\ 0 & 0 & 3.27 \end{bmatrix}_{\mathbf{t}_i^4 \otimes \mathbf{t}_j^4} \times 10^{-4}\ \mathrm{kg \cdot m^2}$	$\begin{bmatrix} 3.93 & 0 & 0 \\ 0 & 3.93 & 0 \\ 0 & 0 & 7.84 \end{bmatrix}_{\mathbf{t}_i^5 \otimes \mathbf{t}_j^5} \times 10^{-2}\ \mathrm{kg \cdot m^2}$

Table E.7   All inertias used for bi-directional ground motions.

$k_{c\gamma}$	k_{top}	$c_{c\gamma}$	c_{top}	μ_1	μ_2	μ_3	μ_4
10^7 N/m	10^6 N/m	5 N·s/m	5 N·s/m	0.118	0.036	0.036	0.137

Table E.8   All stiffnesses and damping constants used for bi-directional ground motions.